THE UNIVERSITY OF CHICAGO

PLANETESIMAL COLLISIONS IN THE EARLY SOLAR SYSTEM AND A FRAMEWORK FOR INTERPRETING IRON METEORITE COOLING RATES

A DISSERTATION SUBMITTED TO
THE FACULTY OF THE DIVISION OF THE PHYSICAL SCIENCES
IN CANDIDACY FOR THE DEGREE OF
DOCTOR OF PHILOSOPHY

DEPARTMENT OF THE GEOPHYSICAL SCIENCES

BY
RICHARD J. LYONS III

CHICAGO, ILLINOIS
JUNE 2020

I dedicate this dissertation to my family: my parents Richard and Kathleen, my sister Elizabeth, my wonderful and clever partner Sophia S. Carryl, and my grandmothers June "Nanas" Dray and Maggie Lyons. And a special gratitude to my late grandfather, Robert "Papas" Dray, whose inquisitive nature and infectious laughter brought joy to all around him. Papas, you are missed every single day.

I would also like to dedicate this dissertation to all those with learning disabilities. Hard work and persistence are key, but support and love from those around you are paramount.

"It's beginning to look as if it's true, that planets are a dime a dozen." – Carl Sagan (1977)

TABLE OF CONTENTS

LIST OF FIGURES

LIST OF TABLES

ACKNOWLEDGMENTS

Foremost, I would like to express an immense gratitude to my advisor, Professor Fred Ciesla, for his continuous support of my Ph.D. study and research, for his patience, motivation, enthusiasm, and immense knowledge. His guidance helped me in all aspects of my research and the writing of this thesis. I could not have imagined having a better advisor and mentor.

In addition, I would like to thank the rest of my thesis committee: Professor Andrew Campbell, Professor Andrew Davis, and Professor Nicolas Dauphas for their encouragement, insightful comments, and probing questions over the years.

My sincere thanks also goes to my collaborators: Dr. Thomas Davison, Professor Gareth Collins, Dr. Timothy Bowling, Dr. Sebastiaan Krijt, and Clara Maurel with whom I have had many insightful discussions and worked through many difficult problems.

I thank my fellow DoGS for their laughter, hangouts, and camaraderie throughout this Ph.D. journey: Gabriel Vargas, Dr. Reto Trappitsch, Dr. Nicolas Greber, Dr. Grant Macdonald, Dr. Predrag Popovic, Sam Holo, Nigel Brauser, Dr. Gerard Olack, Dr. Stewart Edie, Dr. Bethany Chidester, and Dr. Larry Grossman.

Lastly, I would like to thank my family: my parents, Richard and Kathleen, for giving every opportunity and supporting me every step of the way. My sister, Elizabeth, who has been encouraging and proud of my work. My partner, Sophia S. Carryl, without her support, love, and never-ending inspiration this thesis would not have been possible. And all of the Carryl, Dray, Lyons, and Roberts that have been cheering me on throughout my life.

ABSTRACT

Understanding how planets form is similar to a detective working a crime scene. The end results are all around us, but we need to look at the finer details and piece together the clues to find out how it all happened. When deciphering planet formation, difficulties lie in the fact that the planets we see today are the product of 4.5 billion years of dynamic and geologic evolution. Fortunately, the Asteroid Belt holds useful clues as it is populated with planetary building blocks (i.e. planetesimals) leftover from the epoch of planet formation. Meteorites, which are samples of these bodies, can provide key insights into the earliest evolution of the Solar System. Through meteorites, the types of collisions between these planetesimals during planet formation can be inferred and illuminate the dynamics at the time. If we can find the traces of these impacts hidden in meteorites, we can start to align the evidence and crack the case.

Iron meteorites provide a direct look at the processes that occurred on differentiated planetesimals such as their heating, separation of metal and silicate, cooling, and impact history. These effects are often treated independently of one another; however, we know that they would have been simultaneous and their concurrent effects need to be understood. Here, the effects impacts had in the early Solar System on the cooling histories of planetesimals are quantitatively investigated. This work shows, through the combination of impact and thermal models, that collisions can rapidly increase the cooling as well as create cooling rate variation (spanning many orders of magnitude in some cases) throughout the metal of differentiated bodies. The effectiveness of these impacts in causing such changes is dependent on the thermal and rheologic state of the impacted planetesimals, and subsequently, the time of the impact. The accelerated cooling also leads to nonlinear cooling of the metal in a planetesimal. Such nonlinear cooling would affect the formation of the Widmanstätten pattern, leading to differences when compared to the constant cooling rates of unimpacted bodies. These differences can be significant and can provide a means to identify the signatures of impacts in meteoritic samples. The traces of these impacts can, therefore, be searched for

in the meteoritic record and could answer the many questions surrounding the formation of various meteorite groups (e.g. IAB, IIE, IVA, IVB). Determining what types of collisions are responsible for creating these tracers can also offer a means of probing the dynamics of the early Solar System. Thus, the framework developed here serves as another piece of the planet detective toolkit necessary to understand how planets formed.

CHAPTER 1

INTRODUCTION

Our galaxy is expected to have at least one planet around each star (Cassan et al., 2012). The ubiquity of planets, and differences between each including those around our own Sun, forces us to ask "how do planets form?"

Astronomers tackle this question by studying the gaseous disks around other stars with high-powered telescopes which provide insight into the first few million years of planet formation. These protoplanetary disks illuminate the great variety of conditions from which planetary systems form. However, direct observations of the planets forming in these disks are not possible in these environments. Exoplanet-finding missions, such as Kepler, provide information about planets themselves; however, these are the finished products billions of years after formation. After so much time, the planets have undergone significant dynamical and geophysical evolution, erasing much of the record of their formation.

Our own Solar System, similarly, represents the outcome of 4.5 billion years of planetary formation and dynamical evolution. However, within our Solar System there is the means of exploring planet formation that is not accessible via telescopic studies: meteorites. The study of meteorites provides clues into the initial materials from which planets grew. Studying meteorites and their parent bodies (asteroids) can provide a comprehensive look into the past and can inform us about the processes by which planetary systems form.

The traditional view of planet formation follows the collisional evolution of rocky material. Dust grains began to orbit the newly formed Sun within a gaseous disk. The grains then collide with each other; fracturing, bouncing, and sticking together. These dust aggregates continue to grow, eventually reaching planetesimal size (kilometers in radii) (Lissauer, 1993). Some of these planetesimals become even larger by incorporating the dust, gas, and planetesimals near them, growing to sizes of planetary embryos ($\sim$500 km in radius) and then protoplanets ($\sim$1000 km in radius) (Kokubo and Ida, 1998). Eventually a few of these bodies would reach the sizes and orbits of the planets that we see today. Planetesimals

that escape this growth path remain behind as free-floating objects, dynamically stirred by gravitational interactions with the planets. Many such bodies now reside in the Asteroid Belt, with fragments of them falling to the Earth as meteorites.

These meteorites can provide insight into the early Solar System. Many properties of meteorites have been used to infer characteristics of the planetesimals these meteorites originated from. Features such as mineralogy, texture, and isotopic abundance can inform about the size of the parent body, thermal structure and history, and accretion time. A record of what happened to these parent bodies is potentially obtainable, but requires our interpretation. For example, numerical models of the thermal evolution of a parent body are needed to interpret what physical processes may have taken place (radioactive decay, aqueous alteration, and regolith accretion) and what types of features would be exhibited in the meteorites in such cases (Haack et al., 1990; Ghosh and McSween, 1998; Ghosh et al., 2006; Harrison and Grimm, 2010). Such models study these parent bodies in isolation; however, impacts have often been invoked to describe features observed in meteoritic samples (Krot et al., 2014). Some features are clearly evidence of an impact as the high energy and pressures uniquely associated with impacts are necessary to create the characteristics. Shock metamorphism is a result of alterations to the mineralogy at high temperatures and pressures. Breccia describes a rock that is composed of angular debris broken during an impact and cemented together by fine-grain matrix. Mesosiderites, for example, are brecciated meteorites often thought to be the result of the disruption and reassembly of a differentiated planetesimal (Scott et al., 2001). Glasses are made of molten rock that cooled extremely quickly thought to be a result of exposure to space or other cold temperature environments.

There are also features observed in meteorites that are often indirectly attributed to impacts as they cannot be explained in any other context. For example, meteorites such as the IAB and IIE irons exhibit mixing of silicates and metals, often expected to be largely spatially separated into the core and mantle of differentiated planetesimals. These meteorites have been interpreted as the products of large-scale impacts which mixed hot core and mantle

material (Benedix et al., 2000; Ruzicka and Hutson, 2010; Ruzicka, 2014). The rate at which iron meteorites cooled has also been interpreted as an indirect signature of impacts. A single meteorite group is expected to have a single cooling rate (Haack et al., 1990). Using a feature known as the Widmanstätten pattern, the cooling rate of an iron meteorite sample can be inferred with the aid of numerical modelling (Wood, 1964; Goldstein and Ogilvie, 1965; Rasmussen, 1981; Haack et al., 1996; Yang and Goldstein, 2006). The inferred cooling rates for the IVA and IVB iron meteorites exhibit large ranges which are thought to be the result of an impact exposing the core of a differentiated planetesimal to space (Yang et al., 2011). The H chondrite parent is also thought to have experienced impacts due to inferred metallographic cooling rates ranging from 10 - 50 C/Myr which do not match what is expected for an unimpacted body (Taylor et al., 1987; Scott et al., 2014). Pallasites, long thought to be formed near the core-mantle boundary of a differentiated planetesimal, are thought in some cases be the product of an impact due not only to a range of cooling rates which are unexpected near the core but the presence of plagioclase that does not form in the deep mantle (Yang et al., 2010b; Gregory et al., 2016). Understanding the consequences of impact events can give further insight into the formation of these meteorites.

However, the meteoritic record is at times at odds with models of planet formation in the early Solar System. Haack et al. (1990) used the cooling rates of iron meteorites and thermal evolution models to infer the radii and structure of iron meteorite parent bodies. They inferred these bodies to have radii of 12 - 100 km. However, dynamical models aiming to reproduce the modern day size distribution of the Asteroid Belt determined that the initial population of planetesimals would need to be greater than 100 km in radius (Morbidelli et al., 2009). The iron meteorite parents bodies, which ought to represent this initial population, either are representing an undersized minority or currently have their sizes underestimated.

The traditional model for planet formation also struggles to reproduce particular features of the early Solar System. Traditional computer simulations find that Mars is up to ten times as massive as it should be and that Jupiter and Saturn form on circular orbits (instead of

eccentric as seen today) (Raymond et al., 2009). The failure of traditional models have led new scenarios to be proposed for the formation of the terrestrial planets such as the Grand Tack Model and pebble accretion.

The Grand Tack model proposes that Jupiter migrated inward to the inner Solar System due to gravitational interactions with the gaseous disk, before moving out again after falling into resonance with Saturn (Morbidelli and Crida, 2007; Walsh et al., 2011). During this migration, planetesimals would be dynamically excited, causing a great number of collisions as well as ejections from the Asteroid Belt. The disk of planetesimals and embryos from which the terrestrial planets formed would be truncated much closer to the Sun than it otherwise would have. Mars would then form at the outer edge of this swarm of planetesimals with its low, current-day mass due to the depletion of the available building blocks in its feeding zone.

Pebble accretion has emerged as a favored theory for explaining many features observed in the Solar System, including Mars' small mass. In this formation theory, planets could form quickly through the accretion of pebbles, dust aggregates measuring millimeters to meters in size. The dynamics of these pebbles is largely determined by their interactions with the gaseous disk, which causes the pebbles to drift inwards toward the Sun as a result of gas drag. This drift would allow for these pebbles to accumulate in regions of the gaseous disk to form planetesimals or efficiently incorporated into growing planets. This would quickly result in a body the size of Jupiter's core ($\sim$10M$_{Earth}$) (Lambrechts and Johansen, 2012; Levison et al., 2015). The rapid growth of planetesimals and planets would now be limited in the terrestrial planet region as formation of Jupiter would impede the drift and replenishment of pebbles. This would result in a low-mass planet inside of Jupiter (Mars), as well as a very low-mass region of leftover planetesimals (the Asteroid Belt).

There is little direct evidence of the early Solar System to inform which dynamical model or models may be correct. However, each dynamical model predicts a different impact history for the asteroid belt in the early Solar System, providing information such as probable number

of impacts and average impact velocity. Meteorites are the products of planet formation and may provide a record of the dynamics during which they formed. As impacts have been proposed to be responsible for a number of features observed in meteorites, investigating how impacts affect meteorite parent bodies and the subsequent samples will constrain what types of impacts were present in the early Solar System. What type of impacts could have formed these meteorites? How would alterations to the cooling of a body due to impacts change our interpretations of the parent bodies? What traces of these impacts are measurable in the meteoritic record? What does this tell us about the dynamical environment these impacts took place in?

These questions and problems will be addressed in the following chapters. This thesis has been designed to bridge the gap between meteoriticists' description of the early Solar System via interpretation of the meteoritic record and the dynamicists' models for planet formation. In Chapter 2 I review how impacts have been invoked to explain the various properties of iron meteorites. In Chapter 3 I will discuss how impacts affect the cooling of iron meteorite parent bodies. In Chapter 4 I review the methods by which the cooling rates of iron meteorites have been inferred and the features from which their thermal evolution is determined. Chapter 5 shows how such features are affected by changes in cooling rate brought on by various impacts in the early Solar System. Chapter 6 examines how the impacts discussed here can be related to the dynamics of the early Solar System.

CHAPTER 2

IMPACT FORMATION THEORIES FOR IRON METEORITE GROUPS

Many iron meteorites are thought to be samples of the cores of differentiated planetesimals. These planetesimals were heated, likely due to the decay of ^{26}Al, to a degree such that iron could melt and gravitationally accumulate at the center of the body, separated from the silicate mantle above it. These bodies would then cool and crystallize undisturbed for over hundreds of millions of years (in this work I adopt the abbreviation "Myr" to represent a duration of time in units of millions of years). Meteorites that originate from the same parent body are said to be in the same "group" and can be chemically and isotopically linked to one another (Goldberg et al., 1951; Clayton and Mayeda, 1996; Wasson, 2012; Krot et al., 2014). Later in time, these iron meteorite parent bodies were broken apart and the iron fragments made their way to Earth. The size, the cooling rate, and other characteristic of the parent body can be inferred within the framework of this traditional view of iron meteorite formation. For instance, how quickly these planetesimals cool will depend, first and foremost, on how big they are.

Haack et al. (1990), using 1D thermal models, explored the thermal evolution and calculated the metallographic cooling rates throughout the iron cores of various differentiated planetesimals. The metallographic cooling rate is assumed to be the instantaneous cooling rate when iron has reached its closure temperature. The closure temperature is the point at which diffusion of Ni in the formation of the Widmanstätten pattern has slowed to such a degree that it can be assumed to have ceased. This temperature is assumed to be about 450 C for iron. The mechanisms by which the cooling rate of iron meteorites is determined is outlined in greater detail in Chapter 4. Haack et al. (1990) found that due to the insulation of the silicate mantle and the high conductivity of iron, the cooling rate of the core was uniform and set by the size of the planetesimal. In other words, all factors being equal,

they found that a given cooling rate for the core corresponds to a unique parent body size. In this idealized framework for meteorite formation, iron meteorites groups not only should consist purely of metals but record uniform cooling rates. An example of such a meteorite group is the IIAB that have a narrow range of reported cooling rates (Table 2.1). With those cooling rates, the parent body can be inferred following the relation set forth in Haack et al. (1990); 85 - 120 km in radius. Haack et al. (1990) also explored how the cooling rates would be affected by the presence of regolith or megaregolith at the surface. Regolith is a porous assemblage of rock on the surface of a body as a result of impacts or additional accumulation of dust (with megaregolith being less porous). This layer of porous material greatly insulates a body from heat loss (Warren and Rasmussen, 1987). Introducing regolith, as Haack et al. (1990) found, would decrease the size of a meteorite parent body. This can be seen in Table 2.1 for the IIABs where its inferred parent body radii is nearly halved.

However, there are meteorite groups that are difficult to interpret within this framework. This might be due to models such as Haack et al. (1990) ignoring impacts onto planetesimals during their cooling. Such events have been hypothesized to play a significant role in the formation of several meteorite groups. In this section I will review some groups of iron meteorites that call into question this formation model and look at the impact origins proposed for each.

2.1 IVA & IVB Iron Meteorites

There are some meteorite groups for which a wide range of cooling rates have been inferred for the various members. That is, even though the estimated uncertainty in a cooling rate is a conservative factor of $\sim$2.5 (Wood, 1967; Taylor et al., 1987; Williams et al., 2000; Harrison and Grimm, 2010), different samples in a given group have inferred cooling rates that range over an order of magnitude which can be seen for the IVA and IVB meteorites in Table 2.1. Thus, within the framework of a cooling planetesimal core as described in Haack et al. (1990), multiple parent bodies would been needed within a single group, which would

require such bodies to evolve independently of one another and yet maintain the chemical and isotopic signatures that link them. Further, the cooling rates for many samples from the IVAs and IVBs are quite rapid (>100 K/Myr), implying very small parent bodies for nearly any assumed structure of the parent body, some with radii as low as 10 km. This is at odds with the idea that asteroids were "born big;" that is, that the original planetesimals that grew from dust in the solar nebula measured 100 - 1000 km in diameter (Morbidelli et al., 2009). Such large bodies would be necessary in the Asteroid Belt in order to match the current day size distribution after billions of years of collisional evolution.

Not only do these same meteorite groups have large ranges in cooling rates, but they also have a distinctive correlation between Ni concentration and cooling rate (Yang et al., 2007, 2008, 2010a; Goldstein et al., 2009a,b). For instance, the IVA iron meteorites exhibit faster cooling rates in samples with less bulk Ni concentration. On the other hand, the IVB group records slower cooling rates for samples with low bulk Ni concentrations. As iron melt first crystallizes it excludes some elements such as Ni. The remaining melt is now enriched in Ni compared to the initial melt and with subsequent crystallizations, the solids include large and larger concentrations of Ni. The center of the core is expected to cool more slowly than near the core-mantle boundary and as such, along with other factors such as core size, the direction of crystallization can be inferred. For the IVA group such a relation has been suggested to indicate an outward-in crystallization of the core (Yang et al., 2011). Conversely, the IVBs would indicate in-out crystallization. In order to explain these features various hypotheses for the structure of the parent bodies have been proposed such as a "raisin bread" distribution of iron (Goldstein and Short, 1967; Moren and Goldstein, 1979), several parent bodies (Rasmussen, 1982), or a large scale break-up due to an impact and reassembly (first the core and then other material).

In order to constrain parent body structure of the IVAs and IVBs any hypothesis would need to produce not only the Ni relations, but also the large range in cooling rates. Yang et al. (2008) most recently put forth the idea of a mantle stripping impact event that would

Group	**Cooling Rate (K Myr^{-1})**	**References**	**Conventional (Mantle and Core) (km)**	**With Added Regolith Layer (km)**	**Pre Mantle Stripping Event (km)**	**References**
IAB	1 - 650	Ruzicka (2014)	15 - 275	<10 - 150	-	-
IIAB	6 - 12	Saikumar and Goldstein (1988)	85 - 120	45 - 65	-	-
IIIAB	56 - 338	Yang et al. (1997), Rasmussen (1989)	15 - 40	10 - 25	>300	Yang and Goldstein (2006)
IIE	1 - 1000	Ruzicka (2014)	<10 - 275	<10 - 150	-	-
IVA	100 - 6600	Rasmussen et al. (1995)	<10 - 30	<10 - 20	>300	Yang et al. (2007)
IVB	475 - 5000	Rasmussen et al. (1984)	<10 - 15	<10 - 10	>140	Yang et al. (2010)a
Pallasites	2 - 18	Yang et al. (1997)	70 - 200	40 - 110	400	Yang et al. (2010)b
Mesosiderites	0.5	Yang et al. (1997)	375	200	-	-

Table 2.1: Summary of inferred parent-body radii for several iron and stony-iron meteorite groups. The "Conventional" is the case of a core only surrounded by a mantle. The "Regolith Layer" assumes a porous, insulating regolith on the surface of the body measuring 0.3% the radius of the planetesimal (Eq. 3.4). Both models are derived from Haack et al. (1996). The "Stripped Mantle" case assumes an iron sphere covered by a thin silicate layer, as in Yang et al. (2008). These results illustrate how the physical structure of the body affects the expected cooling rate-radius relationship. We note that the rapid cooling seen in some groups either requires very small bodies in both the Haack et al. (1996) cases or a mantle-stripping impact. The table is adapted from Benedix et al. (2014).

leave behind little to no insulating mantle around the core, leading to rapid cooling. Further, if the exposed core were large enough, gradients in the cooling rates would develop, as the surface would cool much faster than the center. Yang et al. (2008, 2010b) found that the order of magnitude range in cooling rates seen in the IVA and IVB iron meteorites as well as the Ni-cooling rate relation could be explained if they originated from exposed cores that were 150 and 70 km in radii, respectively.

In order to strip away the mantle to create these purely iron bodies, they invoked hit-and-run impacts. Hit-and-run impacts are low velocity, grazing collisions that result in the largest remnant of the target body having a mass comparable to its pre-impact mass (Asphaug et al., 2006; Leinhardt and Stewart, 2012). While the target may be largely unaffected, such events can lead to significant disruption of the impacting body, leaving behind a number of remnants. One such remnant could be composed of entirely hot iron from the core of the impactor. The sizes of the original, pre-hit-and-run bodies that would yield exposed cores of this scale is uncertain, as the collision remnants could represent core fragments much smaller than their progenitors. However, if the iron/silicate ratio was the same as assumed in Haack et al. (1990), then the bodies were at least 300 km in radius, assuming all the metal from the impactor goes into the the IVA or IVB parent body. These mantle stripping events will be explored further in Chapters 3 and 5.

2.2 IAB Iron Meteorites

The IAB iron meteorites are peculiar because they are iron meteorites with silicate inclusions, as shown in Figure 2.1a.

Impact melt pools near the surface of the IAB parent body have been the proposed formation site. An impact would not only heat and melt both the iron and silicate but the close vicinity of each would allow for the two to mix. The location of the melt pool would also allow for the formation of quenched mineralogy. However, this origin has largely been rejected as these small, surface level impact are not thought to produce enough melt

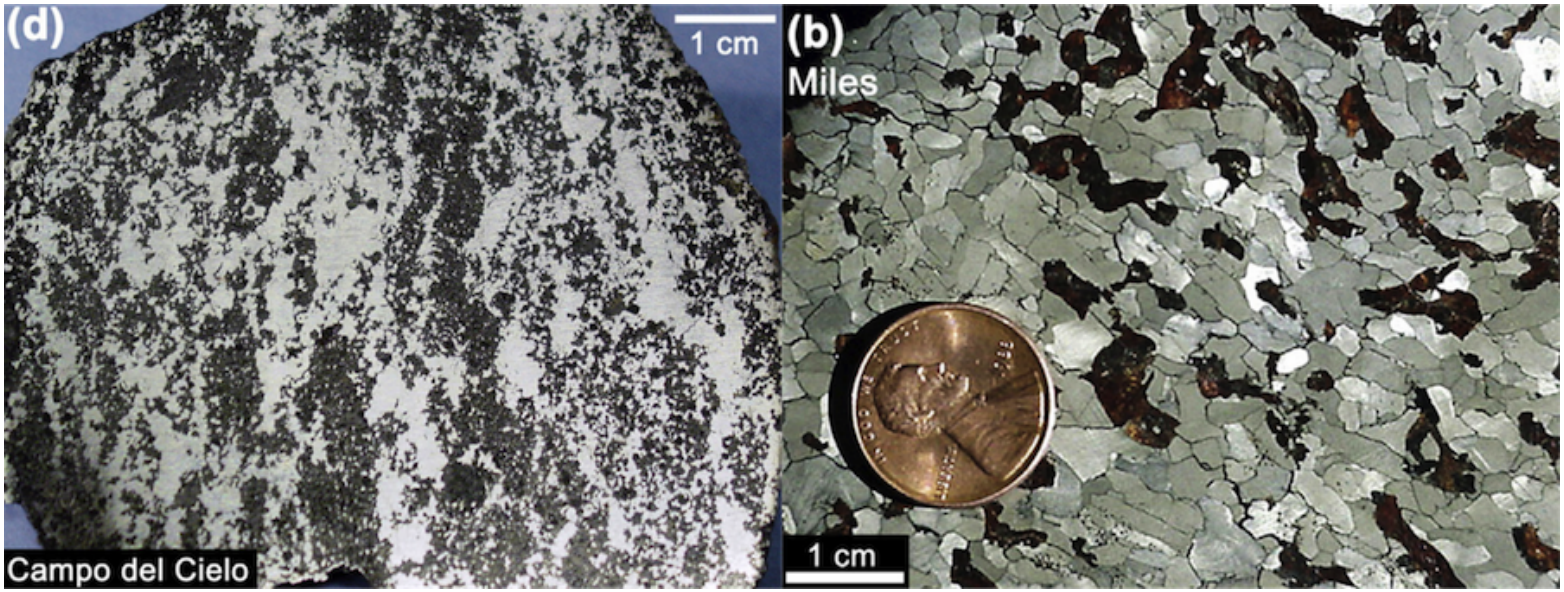

Figure 2.1: Examples of two iron meteorites with silicate inclusions. (Left) A sample from Campo del Cielo IAB iron meteorite. (Right) A sample of Miles IIE iron meteorite. Images from Ruzicka (2014)

to allow for mixing to occur (Wasson and Jianmin, 1986; Wasson and Kallemeyn, 2002). Benedix et al. (2000) studied the petrology and mineralogy of a suite of IAB samples and categorized the lithologies of the silicate inclusions (chondritic, partial-melt, residue) and the compositions of the metal (metal-rich, sulfide-rich) observed. The IAB meteorites exhibit various combinations of melt compositions and inclusions, indicating that mantle silicates as well as chondritic crust from a partially differentiated body were somehow brought into contact with the metal. Figure 2.2 is a mixing cartoon from Benedix et al. (2000) showcasing the proposed initial lithologies of the partially differentiated IAB parent body, the various components that need to be mixed, and the meteorites that exhibit such features.

These meteorites primarily are thought to be a result of a large scale, disruptive impact onto the parent body that mixed silicate from the mantle and crust with metals from the core as there appears to be some signs of fractional crystallization (Benedix et al., 2000; Ruzicka, 2014; Worsham et al., 2016). Figure 2.3 is a cartoon of the type of large impact and re-accumulation which many assume formed the IABs (Ruzicka, 2014). However, no quantitative work has be done to understand if such an impact can mix such spatially disparate material.

In addition to petrologic studies, radiometric ages have been determined for the IABs. Figure 2.4a provides a summary of the radiometric ages for various meteorites in the IAB group as collected in Ruzicka (2014) and references therein. The chronometers listed in the legends in Figure 2.4 are ordered by their respective closure temperatures from high to low. The Hf-W chronometer describes the time when silicate-metal separation began and the formation of the core (Kleine et al., 2008). Core formation in the IAB parent body is well constrained by Hf-W to be about 5 - 6 Myr after the formation of CAIs (Schulz et al., 2009; Hunt et al., 2018), as seen in Figure 2.4. The other chronometers probe the body at later times after core formation as the parent body cools due to those element's lower closure temperatures. For instance, Hf-W reaches its closure temperature at about 1100 K, Pb-Pb probes a temperature range around 725 K, and Ar-Ar is locked in at about 550 K (Schulz

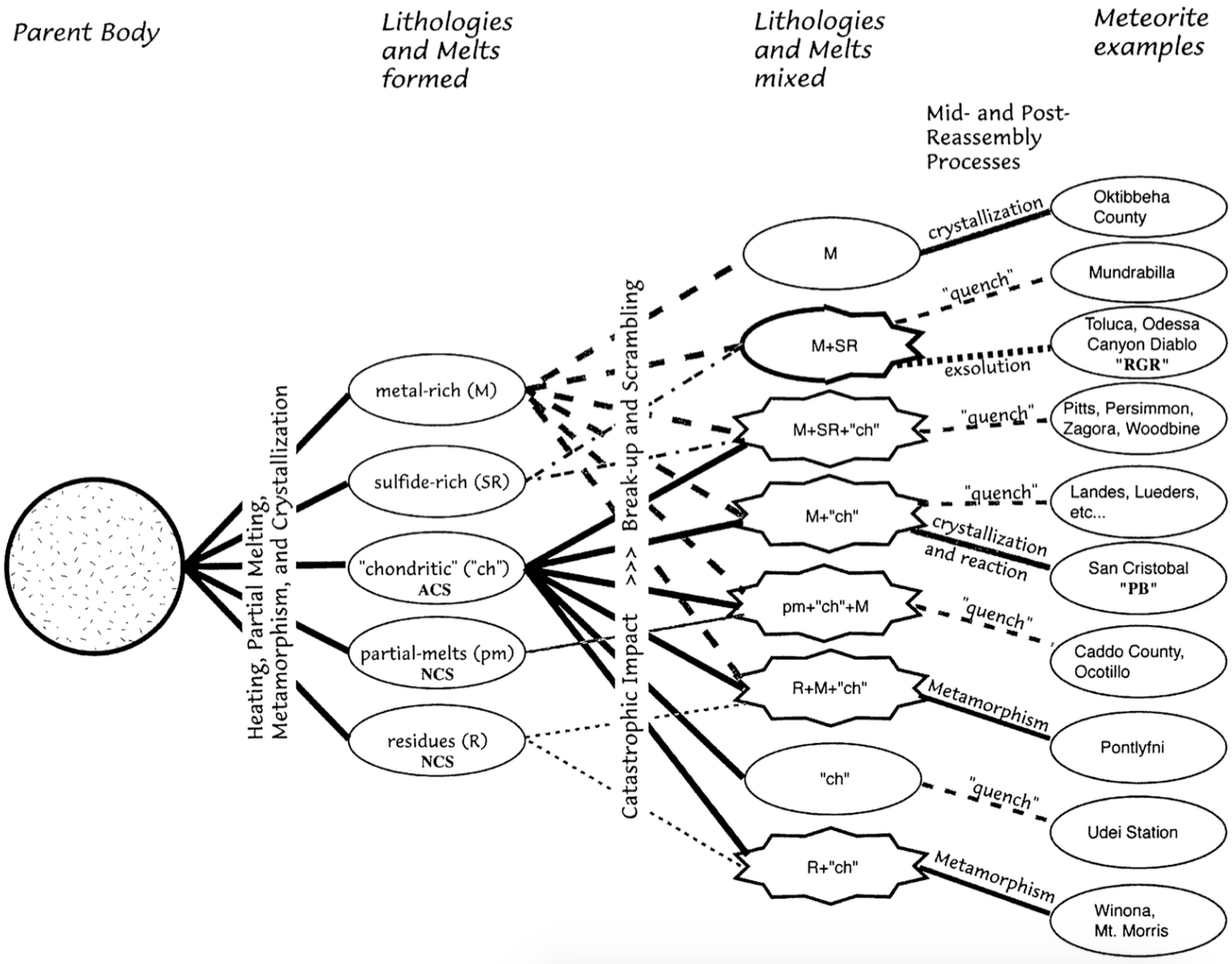

Figure 2.2: Schematic of the formation of the IAB iron meteorites as proposed by Benedix et al. (2000) The parent body begins with a chondritic composition. Differentiation forms the lithologies and melts listed (with abbreviations). The large impact mixes and forms the lithologies and melts observed in meteorite samples listed.

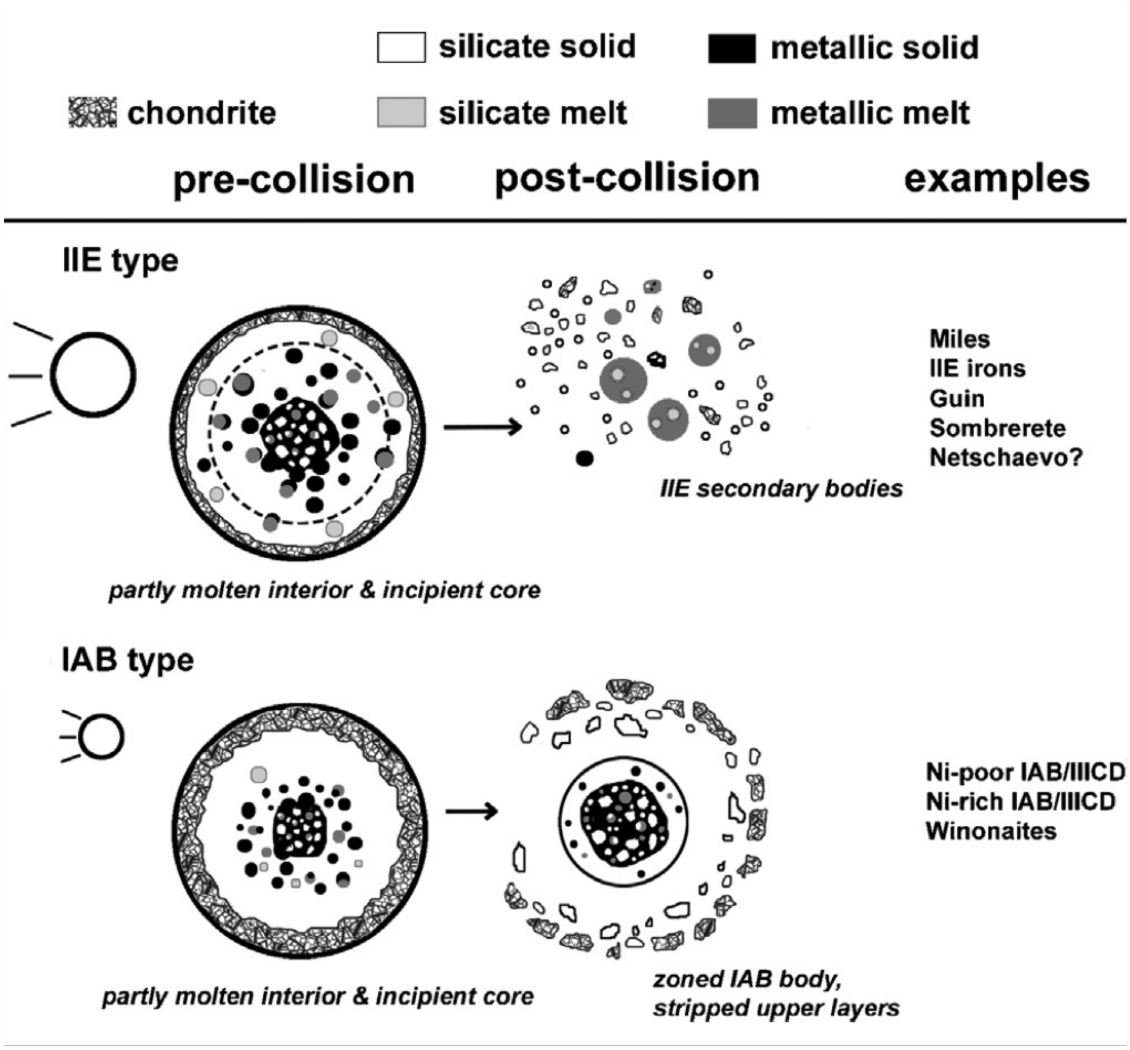

Figure 2.3: Cartoon of formation theories from Ruzicka (2014). The IIE parent body (Top) is impacted resulting in secondary bodies exhibiting fractionated and unfractionated silicates mixed with metal. The IAB parent body (Bottom) is impacted mixing silicates and metals with only the crustal layer stripped.

et al., 2010). Several of the chronometers exhibit ages for the IABs that are later than would be expected by just cooling of an onion shell model Haack et al. (1990). It is possible these dates do not represent the original cooling of the parent body, but instead the system was "reset" by a reheating event that allowed the various species of interest to be remobilized, recording the timing of this later event. Because the timing recorded by these systems are later than expected, an impact induced thermal event would be necessary to reset the ages (Vogel and Renne, 2008; Pravdivtseva et al., 2013; Theis et al., 2013). A potential impact is hypothesized to have occurred about 10 - 14 Myr after the onset of core formation on the IAB parent body (Schulz et al., 2010, 2012; Hunt et al., 2018).

Cooling rates have been determined for many individual meteorites in the IAB group ranging from 1 to 650 K/Myr (Table 2.1) As noted in Figure 2.2, different features of cooling are invoked in order to describe the mixtures of silicates and metals (crystallization, exsolution, metamorphism, quenching) in the IABs. These processes and the rates of cooling are often in disagreement with what one would expect from an unimpacted planetesimal. For example, metal melt would be expected to cool slowly at in the core of the planetesimal as illustrated in Haack et al. (1990), but (as in Landes) is seen to have dendritic features which indicate very rapid cooling (Benedix et al., 2000). This discrepancy in cooling rates between the unimpacted models and dendritic features has been interpreted as the melt being excavated by an impact and the cooling rapidly while exposed to space. Similar inferences can be made for other petrologic and cooling rate discrepancies. The cooling rates can be utilized to infer where in (or outside) the parent body a meteoritic samples cooled postimpact.

While generally accepted, there have been no quantitative models investigating these impact hypothesis and whether the inferred evolution could occur in such an event. To provide such an evaluation, a complete model which investigates the dynamics of disruptive collisions and re-accumulation of debris is needed, along with a thermal model which would explore the postimpact cooling rates recorded by metal. This would allow a better understanding of the types of impacts that would have led to the formation of the IAB parent body. Constraining

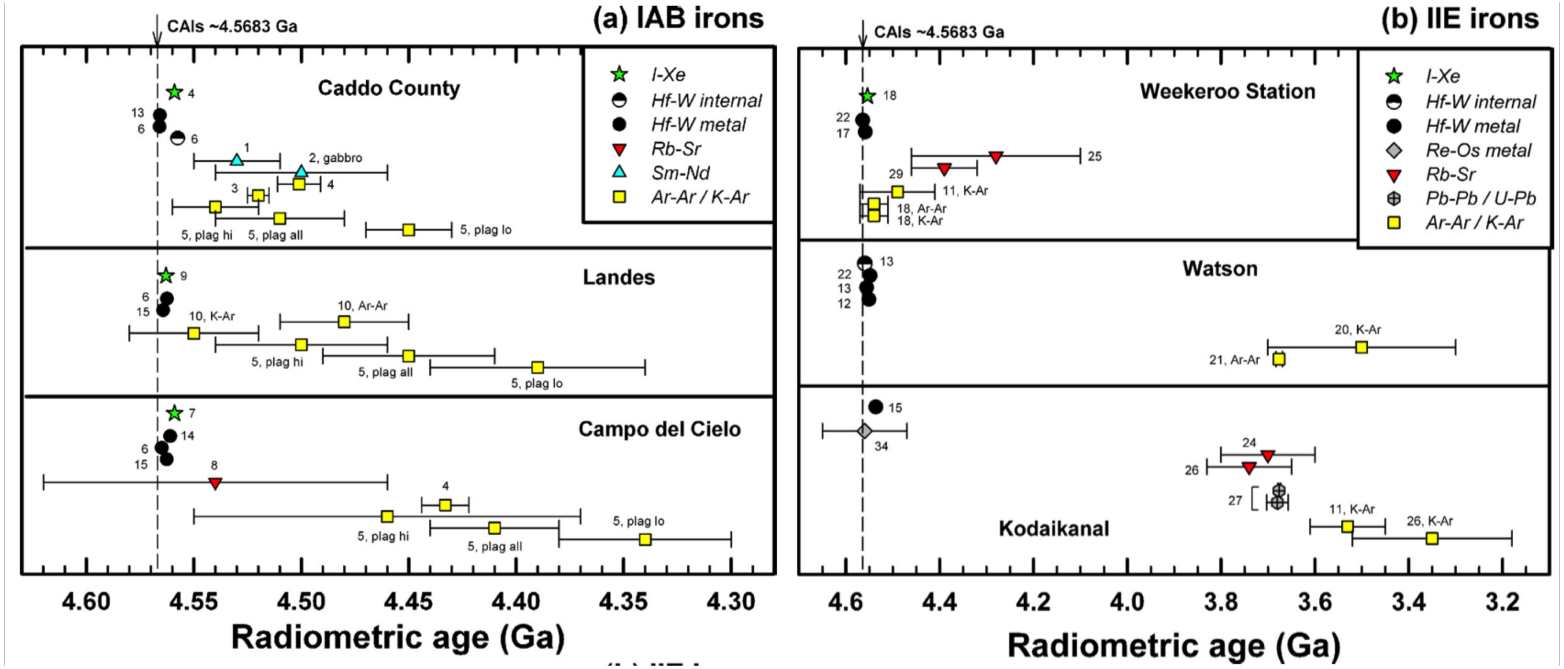

Figure 2.4: The radiometric ages for meteorites from the IAB irons group (Left) and the IIE irons group (Right) found with the isotopic chronometers listed, from Ruzicka (2014). The chronometers in the legends are ordered by the closure temperature from high to low. The radiometric ages exhibit resetting of several chornometers indicated by an age later than would be expected by the closure of a cooling body. These ages have been interpreted as impacts at 10 Myr after the onset of differentiation for the IABs and ∼100 Myr, 1 Gyr for the IIEs.

the range of impact parameters for the IABs (as well as other meteorite groups) will provide a framework for evaluating the dynamical environment in which the impacts occurred.

2.2.1 New Simulations of IAB Formation

Here I investigate how impacts could cause the mixing of iron and silicate to form meteorites like the IABs. I developed a modeling pipeline that simulates an impact onto a planetesimal, tracks the ejected material as it re-accumulates, and follows the subsequent thermal history of the largest remaining remnant (Lyons et al., 2016). The cooling rates in regions of the body where mixing of material has occurred are then compared to the inferred values for the IAB meteorites. I modeled the initial impact using the hydrodynamic shock code iSALE, which has been applied to a number of previous studies looking at impacts between planetesimals (Ciesla et al., 2013; Davison et al., 2012). The 2D version of iSALE can be run with self-gravity, where the gravity field is updated throughout the collision, allowing re-accumulation of the target and ejecta to be followed. However, the computational demands for doing this in the 3D version of iSALE are prohibitive. Thus, the collision is modeled in the 3D version until the shock wave had dissipated, with no further acceleration from the impact occurring (on the order of 100s of seconds). The density, velocity, and position of mass everywhere in the simulation is then fed into the N-body code, REBOUND, which maps the target and ejecta into a system of particles that interact gravitationally and collisionally, allowing the re-accumulation to be modeled.

A similar approach was used in Leinhardt and Stewart (2009) using the smooth-particle hydrodynamical (SPH) code CTH in place of iSALE, and pkdgrav in place of REBOUND. That work looked at collisions and subsequent re-accumulation between Kuiper Belt objects. While comparisons between CTH and iSALE have been done previously and shown the codes to be in good agreement with one another (Elbeshausen and Wünnemann, 2011), such tests were not performed with REBOUND and pkdgrav for planetary applications. Figure 2.5 shows the outcome of low velocity asteroid collisions with REBOUND (top row; this work)

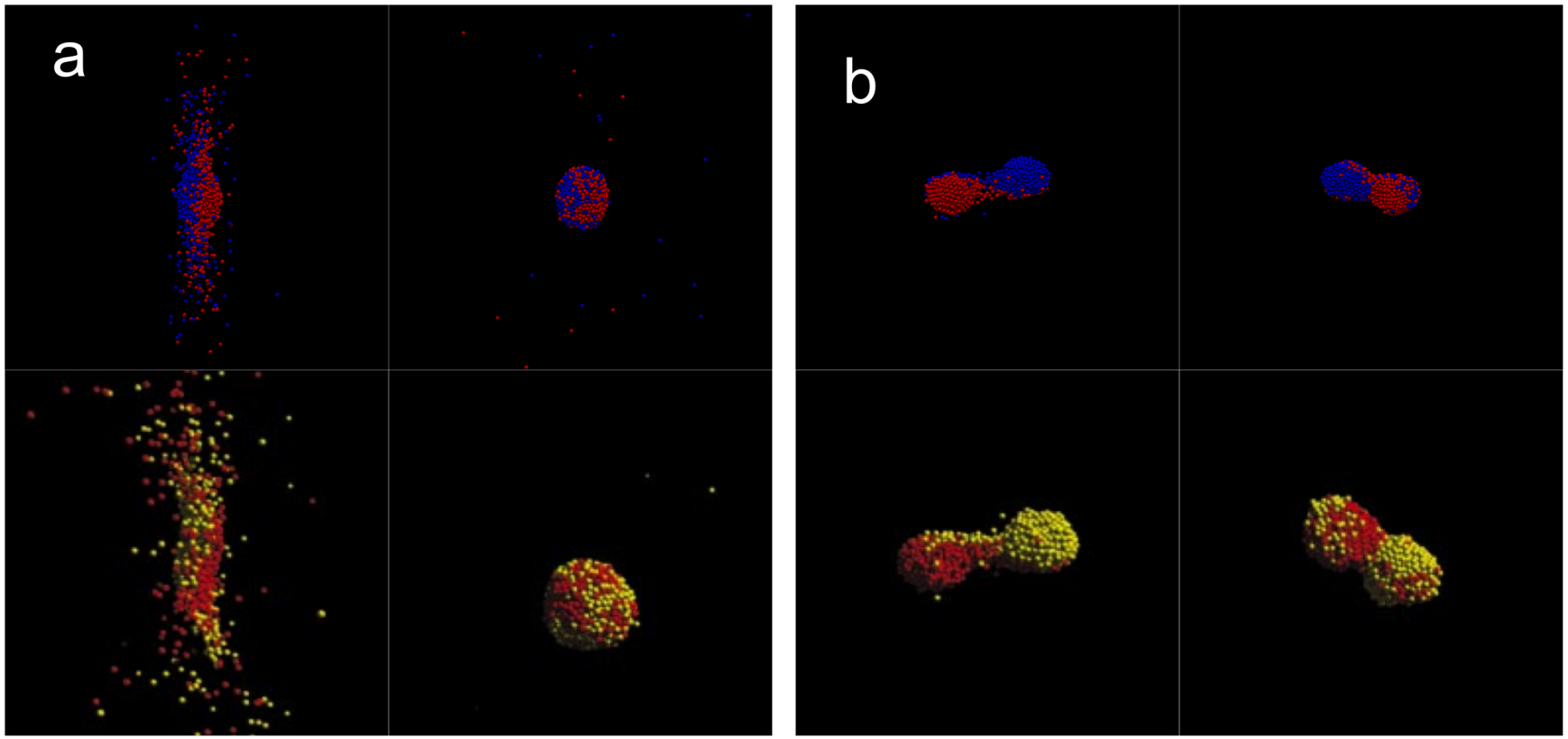

Figure 2.5: The left is a head-on impact of two rubble piles at the velocity necessary to disperse them as outlined in Leinhardt et al. (2000). The right is a grazing impact at 45 degrees at 0.52 the dispersal velocity. The top row for are my simulations using REBOUND while the bottom are images provided in Leinhardt et al. (2000) using pkdgrav. REBOUND agrees well to those performed in Leinhardt et al. (2000) with respect to the remaining mass fractions postimpact.

and pkdgrav (bottom row; Leinhardt et al. (2000)). Figure 2.5a shows a head-on impact of two rubble piles at the initial time of impact and the re-accumulated body. Similarly, Figure 2.5b is a grazing impact at 45 degrees. The two N-body codes are in good agreement with respect to the remaining mass fractions for both the head-on (.93) and the grazing (.99).

With REBOUND shown to be similar to other particle codes, the modeling pipeline can be confidently used to examine the re-accumulation of impacted bodies as described above. Once re-accumulation is complete (10 - 50 hours), the thermal structure of the largest remnant is passed to a 3D thermal model based on that in Ciesla et al. (2013) which tracked the conductive cooling over time. This allows the temperature of the remnant as a function of time to be determined. Of particular interest with the IABs in mind are cells identified by iSALE as containing both iron and rock. The cooling rates for the re-accumulated body can be calculated and compared to those inferred for the IABs (Table 2.1).

Figure 2.6 shows two examples of this pipeline. The left panels show a radiogenically heated, 100 km radius body of pure dunite that is below the assumed solidus of silicate at its center ($\sim$1300 K) impacted at 10 km s^{-1} at a 45 degree angle by a 20 km impactor also composed of dunite. The right panels show a 100 km body with a 20 km metal core within the same thermal structure as the dunite body but impacted head-on at 5 km s^{-1}. Dunite is used to model the impactor and the planetesimal because there are only a few materials for which a detailed equation of state has been determined and approximations to chondritic or mantle material need to be made. The material properties of each of the targets and impactors are outlined in Table 3.2. Each image represents a snapshot of the components of the outlined modeling pipeline (iSALE, REBOUND, thermal evolution input). The re-accumulated remnant for the pure dunite body was about 85 km and the iron core body was about 65 km in radii. The plots at the bottom show the cooling rate of each grid cell of the re-accumulated body, when it had reached a temperature of 500 C, as a function of its peak temperature.

For the model with an iron core, cells in the iSALE simulations that contained both sili-

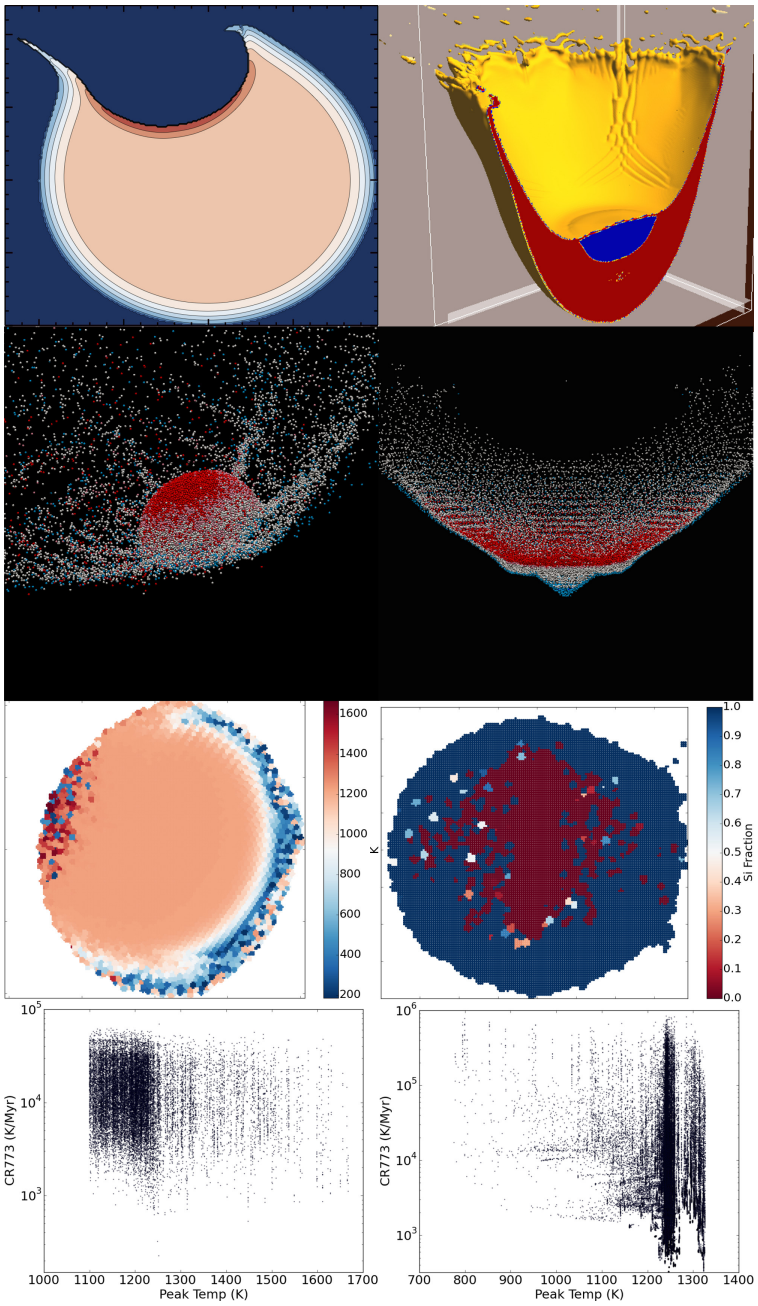

Figure 2.6: Two examples of the modeling pipeline for impacts onto a heated planetesimal. (Left) A 45 degree impact into a 100 km dunite body at 10 km s^{-1} with a 20 km dunite impactor. (Right) head-on impact into a 100 km dunite body with a 20 km iron core at 5 km s^{-1} with a 20 km dunite impactor. The pipeline, in order; 3D iSALE hydrodynamic code, REBOUND N-body code, thermal evolution model, and the recorded instantaneous cooling rates at 450 C with respect to peak temperature. We see mixtures of hot and cold material in the rocky body resulting in cooling rates of some regions near the upper bound of the recorded IAB cooling rates (650 K/Myr). We also see a great amount of mixing of silicate and iron in the model on the right involving the differentiated body. This results in a large portion of the re-accumulated remnant cooling near the upper bound as shown in 2.1.

cate and iron were observed and may represent locations where the characteristic mixing in the IAB samples can occur (on a much smaller scale than modeled here). This is illustrated with the silicate fraction plotted throughout the body in the third row of Figure 2.6. The cooling rates were recorded and found to be at the upper end of inferred values for IAB meteorites; 1 - 650 K/Myr (Table 2.1). However, if the IAB parent body had not differentiated at the time of impact, as modeled with the entirely dunite body with no core, the cooling rates of the mixed material are not slow enough to match the meteoritic data (Hunt et al., 2018). While further work is needed to understand how mixing of metal and silicates would occur on the scales seen in meteorites, these preliminary results shows that impacts could have had a profound affect on the thermal evolution of meteorite parent bodies, and should be accounted for in understanding the origins of particular samples.

2.3 IIE Iron Meteorites

The IIE iron meteorites are another example of iron meteorites with silicate inclusions, examples of which are shown in Figure 2.1b. As with the IABs, the IIE parent body is thought to be formed by a large scale impact that resulted in the formation of smaller secondary bodies (Ruzicka and Hutson, 2010). This is primarily due to the classification of the IIEs into two groups based on their silicate inclusions; fractionated and unfractionated. Fractional crystallization is the process by which the crystallized phase is removed from equilibrium with the remaining liquid. This process results in the last melt to be enriched in elements incompatible with the previously crystallized phases. The fractionated silicate inclusions in the IIEs imply an origin in the parent body that was warm enough to allow for (at least partial) melting, where as the unfractionated inclusions have nearly chondritic composition. Therefore, Ruzicka and Hutson (2010) theorized that an impact onto the IIE parent body formed secondary bodies that were composed of either entirely fractionated silicates from the upper mantle or unfractionated silicates from the unmelted crust. As with other meteorite groups, the inferred cooling rate range reported in Table 2.1 (1 - 1000

K/Myr), has been interpreted as an indication of burial depth of a given sample postimpact. Figure 2.3a is a cartoon illustrating the formation of the IIE meteorites as described in Ruzicka (2014) and, as seen with other meteorite groups, is the extent to which impacts have been invoked. The possible impact had not been quantitatively investigated.

Radiometric ages have been determined using isotopic measurements for a variety of IIE meteorites. Figure 2.4b provides a summary of the radiometric ages as collected in Ruzicka (2014) and references therein. Core formation for the IIE parent body is well constrained by Hf-W to be about 5 Myr after the formation of CAIs (Schulz et al., 2010). The other chronometers probe the body at later times as the material cools. Some IIE meteorite samples show that the IIE parent body experienced a resetting about 100 Myr after silicate metal separation (Weekeroo Station) and others do not show a resetting until $\sim$1 Gyr after differentiation (Ruzicka, 2014). These resetting events for the respective isotopic chronometers have been interpreted as impacts, the earliest being the large scale disruption described in Figure 2.3a.

Magnetization has also been measured in several IIE meteorites (Maurel et al., 2019). The presence of magnetization implies the existence of a dynamo in the core of the planetesimal. The strength of the magnetization also implies that there had to be a large enough core to produce a corresponding magnetic field with similar intensities. For the iron in the two IIE samples investigated (Colomera and Techado) to be magnetized to such a degree, a core 60 km in radius must be present and the would-be iron meteorite would need to be buried $\sim$30 - 60 km from the surface of a $\sim$170 km radius body. Such a parent body size as well as burial depth would not only match the magnetic field strength but the inferred cooling rates as well via 1D cooling models. The position in the mantle for these samples raises the question of how the iron ended up there? A localized iron melt pool in the mantle would likely not be the case given the extent of heating and differentiation needed to form the core and the subsequent dynamo. Could the placement of the iron be the result of the impact that reset the chronometers?

2.3.1 New Simulations of IIE Formation

In order to investigate the feasibility of an impact origin for Colomera and Techado, I performed impact simulations focusing on the two representative scenarios (excavation and implantation). These simulations are not meant to find the specific set of impact conditions that could have formed a IIE reservoir on a partially-differentiated parent body, but explore the feasibility of such an origin.

A suite of numerical simulations were conducted using the latest version of the iSALE2D shock hydrodynamics code, iSALE-Dellen, with a cylindrically symmetric computational mesh. Given the two-dimensional geometry of the simulations, only vertical impacts were simulated. The target planetesimal was 170 km in radius with a 60 km radius iron core and a 110 km thick silicate layer in order to match magnetization and cooling rate constraints. The initial thermal profiles of the target at 10, 30, and 60 Myr after CAI formation were obtained from a 1D thermal model. In all simulations, the core was molten (T > 1250 K, solidus of iron) and treated as a fluid with a constant viscosity of 100 Pa s (Johnson and Cook, 1983). For an impact at 10 Myr after CAI-formation, 53% of the silicate layer is still above its solidus ($\sim$1373 K) and therefore only partially molten. At 30 Myr, 27% of the silicate layer is still above its solidus, whereas at 60 Myr, nearly all of the silicate has solidified. In each case, the still molten silicate is nearest to the core-mantle boundary. We used the ANEOS package to determine the equation of state of each material using published rheologic properties of dunite for the silicate layer and iron for the core. The spatial resolution was between 14 and 16 cells per projectile radius (CPPR), which resulted in a grid spacing between 2 and 2.5 km. The simulations were stopped after internal flows within the body had ceased. A number of impact conditions were considered either with the projectile made of iron or rock (dunite). In either case, the impactor had a radius ranging from 10 to 40 km and impacted at a velocities from 1 - 9 km s^{-1}, totaling 29 simulations.

We found that a pure iron impactor, 30 km in radius, can be implanted permanently in the upper half of the silicate layer at low impact velocity (1 km s^{-1}). It follows that at

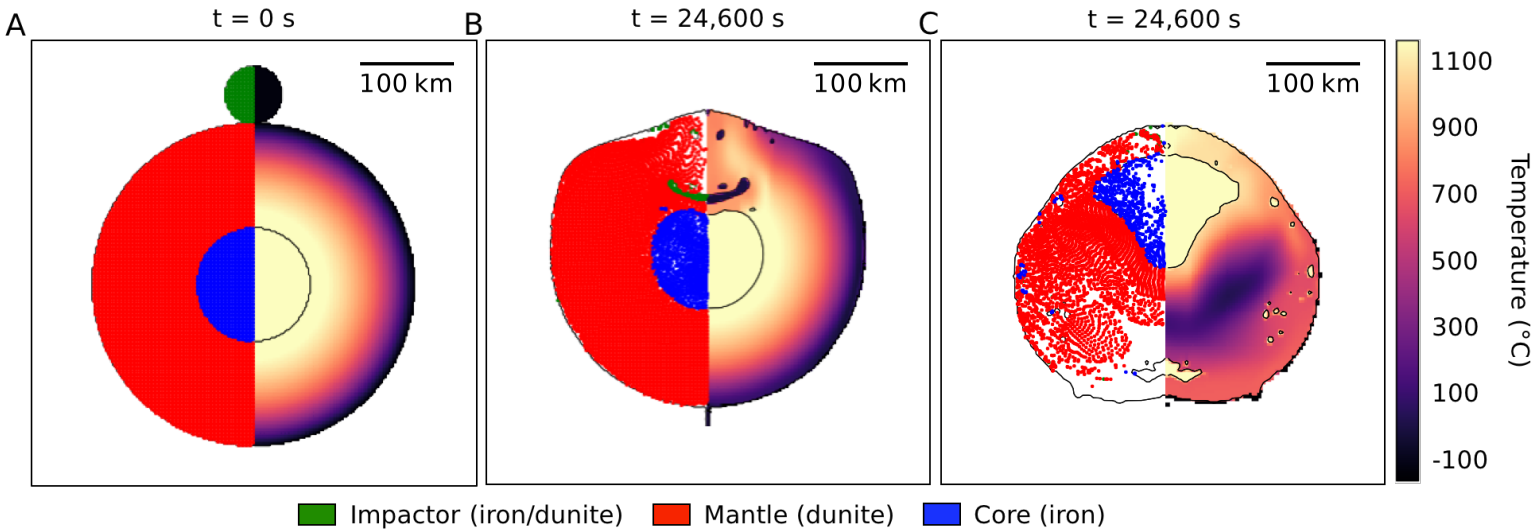

Figure 2.7: A) Initial state of a 170 km radius target with a 60 km radius iron core and a 110 km thick dunite layer prior to impact. The impactor is 30 km in radius, solid, and made of either iron or dunite. The left-hand side of the figure shows the materials and the right-hand side shows the temperature after 30 Myr of thermal evolution since CAIs. B) This is the resulting target after 24,600 s for a 30 km radius iron impactor impacting vertically at 1 km s^{-1}. White space within the body on the left-hand side denotes a lack of tracers, not material. This is a result of the tracers being closely grouped postimpact. The iron impactor is implanted in the mantle at various depths. C) End of the impact simulation after 24,600 s for a 40 km radius, dunite impactor impacting vertically at 5 km s^{-1}. Small amounts of core material are excavated into the upper half of the target's silicate layer while the impactor is distributed throughout the body. As published in Maurel et al. (2020).

higher velocities the iron impactor could penetrate through the silicate layer and merge with the core. Conversely, much slower impacts would not bury the iron impactor deep enough into the body to match the inferred cooling rates. This implantation of the iron into the warm silicate preserves the core and allows for a magnetic field to be recorded as iron melt pool cools and crystallizes. Considering a dunite impactor, impacts between 4 and 5 km s^{-1} with an impactor 40 km in radius can result in portions of the target's molten core being uplifted into the silicate layer. Figure 2.7 illustrates these two possible outcomes looking at a slice through the center of the iSALE simulations with the left-hand side of each following a finite number of tracers of the impactor (green), mantle (red), and core (blue). The right-hand side shows the temperature profile of the body with the given color-bar. Figure 2.7a is the initial state of the simulation before impact with a thermal structure determined by a thermal evolution model which has cooled for 30 Myr. Figure 2.7b is the product of the impact due to an iron body with a 30 km radius impactor at 1 km s^{-1} and Figure 2.7c is the result of the 40 km radius dunite impactor at 5 km s^{-1}. Both of the resulting profiles are 24,600 s postimpact. In each case, the iron reservoir is impeded from percolating back to the stirred-up core due to the cool, crystallized silicate surrounding it.

From the suite of simulations conducted with a 30 km radius metallic impactor, the impactor merges into the core at velocities $\geq$ 2 km s^{-1}. However, one of the simulations shows that a smaller, 10 km radius impactor could be implanted in the upper half of the mantle when impacting at $\geq$ 4 km s^{-1} (Figure 2.8a), although with only marginal heating ($<$ 100 K) and less overall iron material.

Conversely, collisions involving a chondritic impactor which excavate small amounts of core material into the mantle have a narrow range of allowable impact energies. For a 40 km radius impactor, impacts at $\leq$ 3 km s^{-1} do not disturb the core at all and only stir-up the mantle. Impacts with velocities $\geq$ 6 km s^{-1} were found to fully break up the core, lofting iron into the upper regions of the body, but leaving no central core for which a dynamo can be produced. Figure 2.8b is such an impact involving a 6 km s^{-1}, 40 km radius chondritic

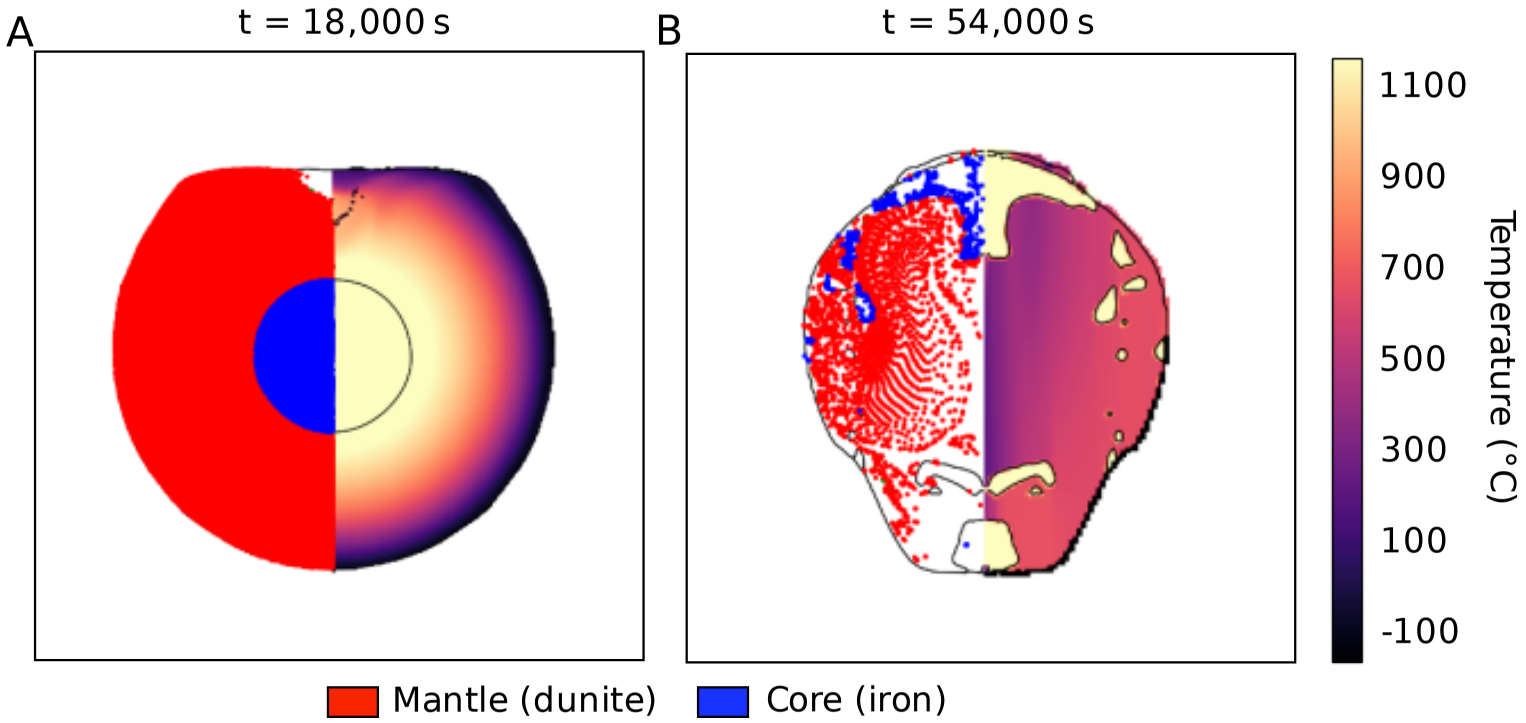

Figure 2.8: A) End of an impact simulation after 18,000 s for a 10 km radius, pure iron impactor impacting vertically at 4 km s^{-1}. The left half of the figure shows the materials, and the right half shows the temperature. Small amounts of projectile material (green) are implanted into the upper half of the target's mantle. White space within the body on the left-hand side denotes a lack of tracers, not material. B) End of an impact simulation after 54,000 s for a 40 km radius, pure dunite impactor impacting vertically at 6 km s^{-1}. The core is broken up and scattered in the upper portions of the target leaving no core for the dynamo to be produced. As published in Maurel et al. (2020).

impactor.

Head-on impacts are less likely than impacts at an angle with respect to the normal to the surface of the target, with 45^o being the most probable configuration (Shoemaker, 1962). Such oblique impacts were not explored here as they require computationally expensive three-dimensional simulations. Our work is meant to be a proof of concept that iron (be from the target body or the impactor) can be implanted in the silicate layer of a partially-differentiated planetesimal and the 2D models discussed here show just that. However, 3D iSALE simulations of nonvertical impacts onto nondifferentiated planetesimals have shown that impacting at an angle shallower than vertical yields less heating and less material excavation for the same impact velocity (Davison et al., 2014). Oblique impacts may therefore allow for faster impactors (given the same size) than those used here for a similar implantation of exogenous iron or excavation of endogenous iron into the mantle. Although, one limitation to highly oblique impacts would that the amount of material from the impactor effectively accreted during these collisions significantly decreases, similar to decreasing the impactor size (Figure 2.8a).

Each of the impacts showcased in Figure 2.7 provide a possible impact origin for the IIEs given constraints. Maurel et al. (2019) and Maurel et al. (2020) provides further discussion into the meteoritic analysis, dynamo modeling, and the probability of such impacts in the early Solar System.

The story revealed by the meteoritic samples discussed in this chapter indicates that impacts shaped many parent bodies early in the history of the Solar System. Impacts would be common during this time, and have been hypothesized to be the origin for particular features and thermal evolutions of many groups of meteorites. Thus it is critical to develop a rigorous understanding of how impacts would affect the properties of parent bodies and how these effects may be identified in the meteoritic record. In the remaining chapters, we focus on the cooling of iron within impacted differentiated bodies and how the thermal history is recorded by the subsequent chemical evolution.

CHAPTER 3

THE EFFECTS OF IMPACTS ON THE THERMAL HISTORY OF IRON METEORITES

3.1 Introduction

Mantle stripping impacts have been proposed as the formation mechanism for the IVA and IVB iron meteorite groups, brought on primarily by hit-and-run impacts (Yang et al., 2008, 2010a). However, hit-and-run impacts typically occur between two comparably sized bodies at low impact angles near their mutual escape velocity (Asphaug et al., 2006). In addition, the size of the pre-impact parent body would need to be nearly 300 km in radius to create a remnant 170 km in radius. In reality, this remnant would only represent a fraction of the core of the impactor, pointing to even larger bodies. This would suggest that the original parent bodies of these meteorite groups were very large planetesimals, if not planetary embryos, agreeing with the initial planetesimal sizes proposed by Morbidelli et al. (2009) but also making these events very rare. Such impacts would only be a subset of the possible collisions that meteorite parent bodies may have experienced in the early Solar System. For a 100 km radius body, which is comparable to the inferred size of many meteorite parent bodies (Harrison and Grimm, 2010; Benedix et al., 2014), Davison et al. (2013) showed that the typical relative velocities among 100 km bodies during the first 100 Myr of the Solar System were likely many kilometers per second, with collisions at >10 km s^{-1} being possible in the first 10 - 20 Myr. Given that inferred cooling rates and petrologies of many iron meteorites appear to imply a collisional history, it is necessary to understand the effects that these collisions between smaller bodies at higher energies had on the overall evolution of the parent bodies.

Here, we quantitatively investigate this issue. Work in this Chapter has been published as a paper as Lyons et al. (2019). In the next section we describe the methodology and computational models used in our study. We then present the results of our numerical

analysis and examine how they depend on the assumptions made in our models. We conclude by discussing the implications of our work for interpreting the variable inferred cooling rates of iron meteorites, the presence of a Ni-cooling rate relation, and the possible impact history of a meteorite group's parent body.

3.2 Methodology

We follow a similar procedure to that of Ciesla et al. (2013), who investigated the consequences of impacts on the thermal evolution of chondritic bodies in the early Solar System. In that study, the temperature structure of a purely chondritic body was calculated as a function of time as it was heated by decay of short-lived radionuclides (^{26}Al) and cooled by heat conduction to the surface and radiation from the surface to space. Impact simulations were then performed using the iSALE code in 2D at various times in the planetesimal's history. The postimpact body was then fed into a 2D thermal model and its subsequent cooling tracked over time. The major finding by Ciesla et al. (2013) was that while impacts had been suggested by some authors to be an important source of heating in chondritic bodies (e.g. Rubin, 1995, 2003, 2004), instead their main effect was to accelerate the cooling of these bodies by bringing hot material to the surface where it could cool at much faster rates.

3.2.1 1D Thermal Model

The major change in this work from Ciesla et al. (2013) is that rather than considering chondritic planetesimals, we focus on differentiated bodies. We follow the thermal evolution of a planetesimal as described in Haack et al. (1990) (similar to Yang et al. (2011)), where the body begins at a high temperature state (1900 K), having already differentiated to form a core surrounded by a silicate mantle. The body then cools conductively as described by the 1D heat equation:

$$\rho c_p \frac{\partial T}{\partial t} = \frac{1}{r^2}\frac{\partial}{\partial r}\left(kr^2\frac{\partial T}{\partial r}\right) \tag{3.1}$$

Material	**Density** ($\mathbf{kg\ m^{-3}}$)	**Heat Capacity** ($\mathbf{J\ (kg\ K)^{-1}}$)	**Thermal Conductivity** ($\mathbf{W\ (m\ K)^{-1}}$)
Silicate	3600	1200	2
Iron	7800	600	60

Table 3.1: Material properties used for our differentiated planetesimal as taken from Haack et al. (1990).

where r is the radial distance from the center of the body, and T, ρ, c_p, and k represent the temperature, density, heat capacity, and thermal conductivity of the materials at that location. This is solved using a finite volume approach with material properties and initial conditions described below.

We generally assume that the planetesimal cools from a high temperature where the core and mantle will be at least partially molten. As the system cools, latent heat of phase transitions for both materials is handled as outlined in Haack et al. (1990). The melt fraction of the mantle varies linearly over the temperature range 1373 to 2013 K (the assumed solidus and liquidus temperatures) and is given by:

$$f_m = \frac{T - 1373}{640} \tag{3.2}$$

The latent heat is taken to be $T - 1150$ (with units of J/g). For the core, the amount of melt is defined as:

$$f_c = \frac{S}{0.05454[1800 - T]} \tag{3.3}$$

where S is the sulfur concentration (in units of wt%), and the latent heat is taken to be a constant of 270 J/g. The liquidus temperature of the core depends on the sulfur content, and is found when f_c=1, while the solidus is assumed to be 1250 K. For the models reported here we assume 10 wt% S throughout the core, as in Haack et al. (1990). With a higher S content, the liquidus would be at a lower temperature (and vice versa).

To benchmark our model against that of Haack et al. (1990), we simulated the cooling of planetesimals with a range of radii and a core 44% the radius of the full body. The initial temperature throughout was set at 1900 K, and an ambient temperature at the surface was set to 170 K. Material properties of the mantle and core are given in Table 3.1. Our assumptions match those of the "conventional model" of Haack et al. (1990) with no megaregolith, no regolith, no additional heat production from radionuclides, and no porosity. An example of a thermal run is shown in Figure 3.1 shows the temperature evolution throughout the 100

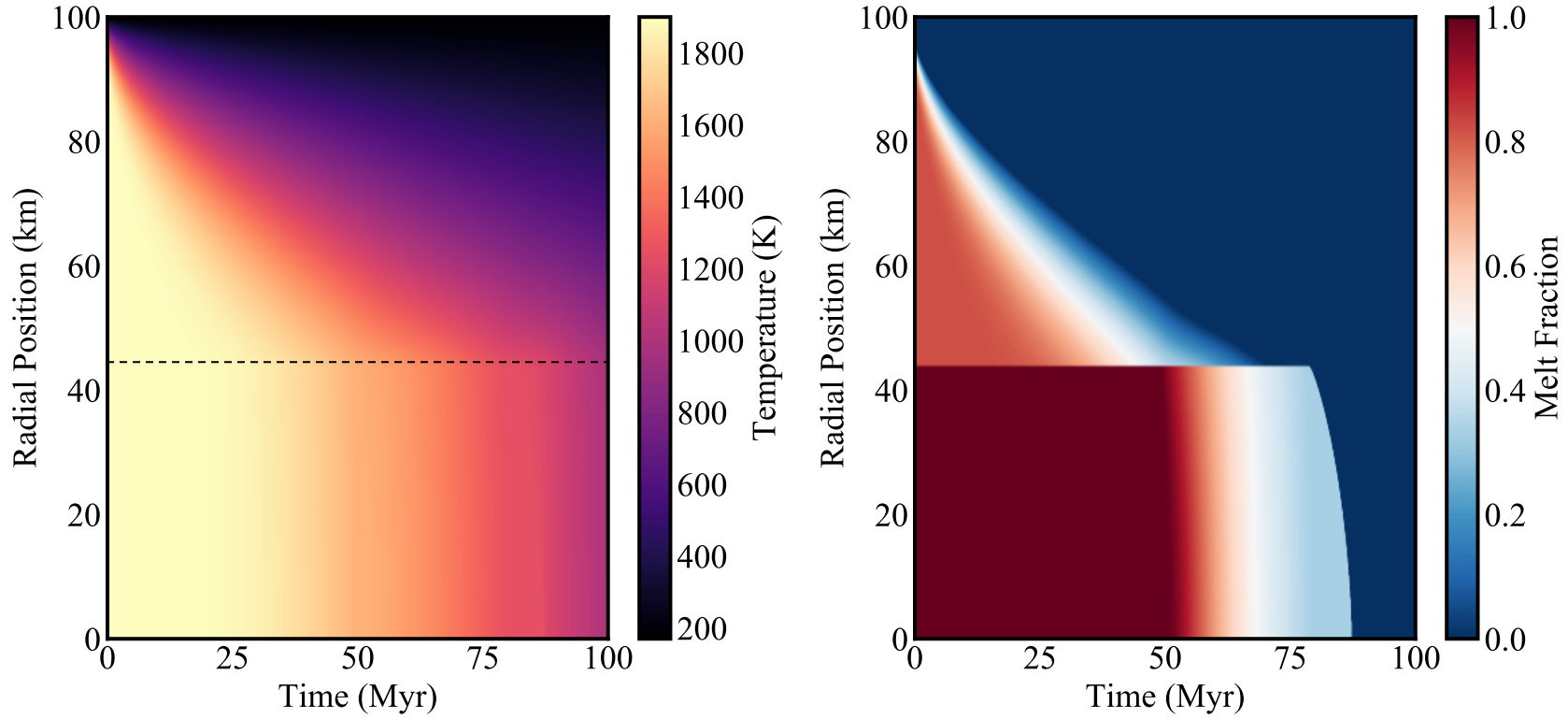

Figure 3.1: The temperature (left) and melt fraction (right) throughout a 100 km radius body over the first 100 Myr of the Solar System. The core-mantle boundary is denoted at 44 km. As published in Lyons et al. (2019).

km radius body as well as the melt fraction in both the core and mantle over 100 Myr of cooling. For all of our simulated bodies, we recorded the cooling rates at 773 K, which is taken as the metallographic closure temperature, as in Haack et al. (1990). Figure 3.2 shows cooling rate as a function of planetesimal size as determined by our model, which agrees within 10% of the "conventional model" of Haack et al. (1990).

For reference, we also plot the cooling rate-radius relation derived by Haack et al. (1990) for bodies with a thin regolith layer (0.3% the radius of the planetesimals) on their surfaces. Regolith is a loosely packed assortment of dust and pebbles near the surface, which forms as a product of small impacts and has a very low thermal conductivity compared to consolidated rock, thus, slowing the loss of heat from a planetesimal. As such, the regolith serves to slow the cooling of the body over time, allowing for smaller planetesimals to yield slower cooling rates within their cores. A best-fit curve to this regolith-included model is given by:

$$R = 149 \cdot CR^{-.465} \tag{3.4}$$

where CR is the cooling rate of the iron core in Kelvin per million years and R is the radius of the planetesimal in kilometers. Eq. 3.4 has been applied to estimate the sizes of the parent bodies for a number of iron meteorites (e.g. Benedix et al., 2014). Going forward, we follow the "conventional model" by assuming no regolith is present over the time of interest in order to evaluate the fastest cooling rates expected in unimpacted bodies. We return to the issue of whether regolith is expected in our bodies in Section 4.

3.2.2 Impact Simulations

We used the iSALE2D shock hydrodynamics code (Wünnemann et al., 2006), an extension of the SALE code (Amsden et al., 1980), to model the effect of impacts on differentiated planetesimals at various times in their thermal evolution. SALE was originally built to model shock processes in gaseous materials, and iSALE extends this work to include sophis-

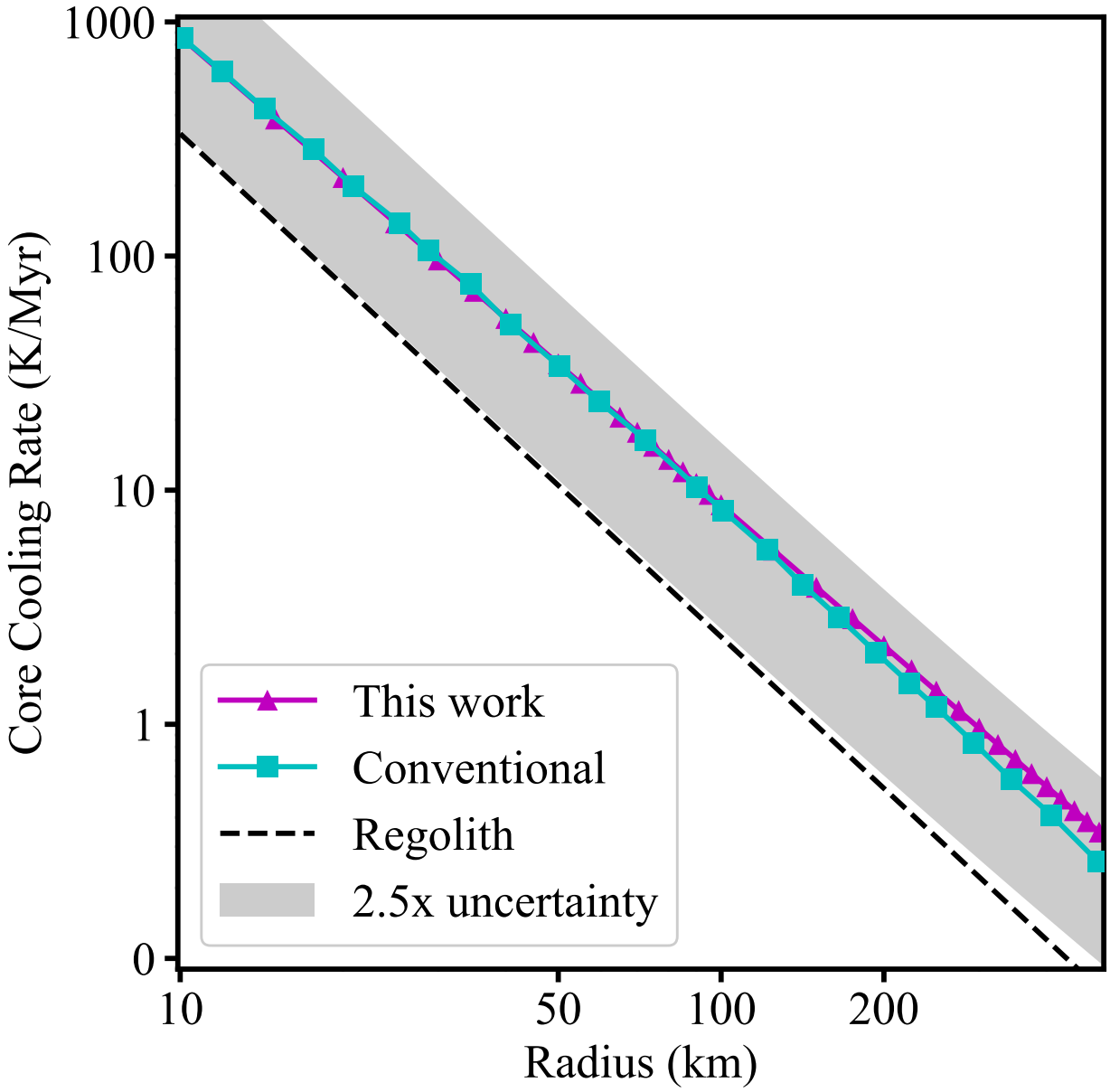

Figure 3.2: Cooling rates as a function of planetesimal radius for the 'conventional model,' of Haack et al. (1990) and this work. Also shown is the relationship for a regolith-covered planetesimal from Haack et al. (1990). The shaded region represents the x2.5 error of the cooling rate for the iron cores of planetesimals. As published in Lyons et al. (2019).

ticated constitutive models and equations of state, and is capable of realistically modeling shock processes in geologic materials (Melosh et al., 1992; Ivanov and Kostuchenko, 1997; Collins et al., 2004). We employed the latest version of the code, iSALE-Dellen. Impact simulations were run using a two-dimensional, self-gravitating, cylindrically symmetric computational mesh as in Ciesla et al. (2013). The two-dimensional assumption required us to only consider the effects of vertical, head-on impacts. This was necessary because the computational requirements for fully three dimensional simulations are much greater than for two dimensional simulations, particularly when self-gravity algorithms are employed. While 2D calculations required us to consider only head-on collisions, the fact that they are computationally less demanding allowed us to explore a greater range of impactor and target properties. pre-impact targets are assumed to be composed of a dunite mantle overlying an iron core, with each material's thermodynamic response described using equation of state (EOS) tables derived using the semi-analytical EOS package ANEOS (Benz et al., 1989; Thompson, 1990).

The rheology of the target mantle was addressed with a fully visco-elastic-plastic strength model (described in Johnson et al. (2016); Elbeshausen and Melosh (2018)) with flow law constants appropriate for the terrestrial mantle (Table 3.2; Kameyama et al. (1999)). The elastic component of mantle strength used the model of Collins et al. (2004) and Davison et al. (2010), and accounted for thermal weakening of the mantle (Ohnaka, 1995). In simulations where the core is below the solidus (1250 K), core rheology was described using the metal-appropriate model of Johnson and Cook (1983) which included an intrinsic thermal weakening term. In simulations where the core was assumed to be molten, the core was treated as a fluid with a constant viscosity. Simulations detailed here can be assumed to have a viscosity of 100 Pa s unless otherwise noted. In cases where the core was solid, we set the melting temperature of the iron in iSALE to 1450 K to ensure the code assigned strength to the iron and treated it as a solid throughout the simulation. In all simulations the impactor was assumed to be made entirely of dunite.

In these simulations, we used a resolution that yielded 15 cells per projectile radius (CPPR), which for a 20 km projectile results in a grid spacing of 1.33 km. The simulation continued until internal flows within the body ceased and a negligible amount of mass was left to be re-accreted (<1% of the target mass). Thus, models were run for $\sim$ 8 - 14 hours of simulation time.

We considered target radii of 50, 100, and 200 km with a single impact occurring at various times in the target's cooling history. For each impact, we took the thermal structure from our 1D models (e.g., Figure 3.1 for 100 km radius body). We considered impacts with impactor-to-target radius ratios of 20% and velocities of 3 and 6 km s^{-1}. These velocities are on the low end of those expected in some dynamical models for the early Solar System, where mean impact velocities can approach 8 to 12 km s^{-1} over the first 100 Myr (Davison et al., 2013).

3.2.3 Postimpact Thermal Evolution

Once the iSALE runs were complete, the physical and thermal structure of the postimpact body was read into a 2D thermal evolution model which tracked the subsequent cooling using the same finite volume assumptions as our pre-impact 1D model. The grid spacing of the thermal model is half that of the impact simulations. For impactors 20 km in radius, which are those we focus on here, this led to grid cell sizes of 0.66 km. We created this finer 2D grid through linear interpolation of the iSALE output. As the postimpact planetesimal cooled, we recorded the cooling rate of the iron at 773 K to compare to those rates recorded by the nonimpacted planetesimals considered above (Haack et al., 1990). In reality, the Widmanstätten pattern in iron meteorites reflects the integrated cooling history of the metal between when the taenite and kamacite nucleate and when Ni diffusion stops. If cooling rates change significantly while the Widmanstätten pattern develops, it is unclear what rate would be most reflected by a given sample and is investigated in Chapter 5.

In all cases, the planetesimal was assumed to maintain the postimpact shape over the

Parameter	**Mantle**	**Core**
EOS	ANEOS dunite	ANEOS iron
Melting Temperature	1436 K (Ivanov et al., 2010)	1450 K
Specific Heat Capacity	1000 J kg^{-1} K^{-1}	440 J kg^{-1} K^{-1}
Thermal Softening Parameter	2.0	1.2
Simon A Parameter	1400 MPa	6000 MPa
Simon B Parameter	5.0	3.00
Poisson Ratio ν	0.25	0.29
Coefficient of Internal Friction (damaged) μ	0.6	–
Coefficient of Internal Friction (undamaged) μ	1.4	–
Strength at Infinite Pressure Y_m	3.5 GPa	–
Cohesion (damaged)	10 kPa	–
Cohesion (undamaged)	50 MPa	–
Johnson-Cook Paramater A	–	100 MPa
Johnson-Cook Paramater B	–	219 MPa
Johnson-Cook Paramater C	–	0
Johnson-Cook Paramater N	–	0.32
Reference Grain Size	1 mm	–
Grain Size	0.1 mm	–
Activation Energy for Diffusion Creep	3×10^5 J mol^{-1} K^{-1}	–
Grain-size Dependence for Diffusion Creep	2.5	–
Reference Viscosity	3.88×10^{10} Pa s	100 Pa s
Activation Energy for Power Law Creep	5.4×10^5 J mol^{-1} K^{-1}	–
Stress Dependence for Power Law Creep	3.5	–
Critical Stress	91.25 Pa	–
Peierls Stress	8.5 GPa	–
Peierls Rate Constant	5.7×10^{11} s^{-1}	–
Activation Energy for Peierls Mechanism	5.4×10^5 J mol^{-1} K^{-1}	–
Stress Dependence for Peierls Mecahnism	2.0	–

Table 3.2: Summary of iSALE Material Parameters used in the simulations described.

entirety of its cooling; that is, we assumed no migration of metal and silicate during cooling. In most cases, this is likely a valid assumption, though more detailed investigations for the physical relaxation of the body should be considered in future work.

3.3 Results

3.3.1 Example Cases: 100 km Targets

Here we illustrate the range of outcomes predicted by our models. We begin by focusing on the 100 km radii planetesimal cases. Figure 3.3 shows an example of one of our case studies, in which a 100 km target is impacted by a 20 km impactor at 3 km s^{-1} 10 Myr after it began to cool. As shown in Figure 3.1, at the time of the impact the internal temperatures in the target have decreased only slightly from their initial values and the core and mantle are still nearly entirely fluid. As a result, while the impact does open a crater, the mantle and core are able to flow for long periods of time after the impact, allowing the target body to relax back to an approximately hydrostatic, spherical shape with a fully formed metallic core at the center. Thus, while the impact perturbs the planetesimal, mixing hotter and cooler mantle to a certain degree (as seen in the postimpact thermal structure), the overall shape and structure of the target is largely preserved in this scenario. After the impact, the core continues to be insulated by a silicate mantle that is comparable to what was present before the impact, resulting in very little change in the overall cooling rate of the core. This is shown in the histogram on the right-hand panel of Figure 3.3, which compares the fractional distribution of cooling rates for the 100 km parent body with and without an impact. As there is little difference between them, no sign of the impact would be recorded in the iron at this time.

Figure 3.4 shows the results of a different impact scenario with a higher impact velocity (6 km s^{-1}) occurring at a much later time, after the core has cooled below 773 K ($\sim$725 K at 112 Myr in this model). At this point, the core has crystallized and thus has significant

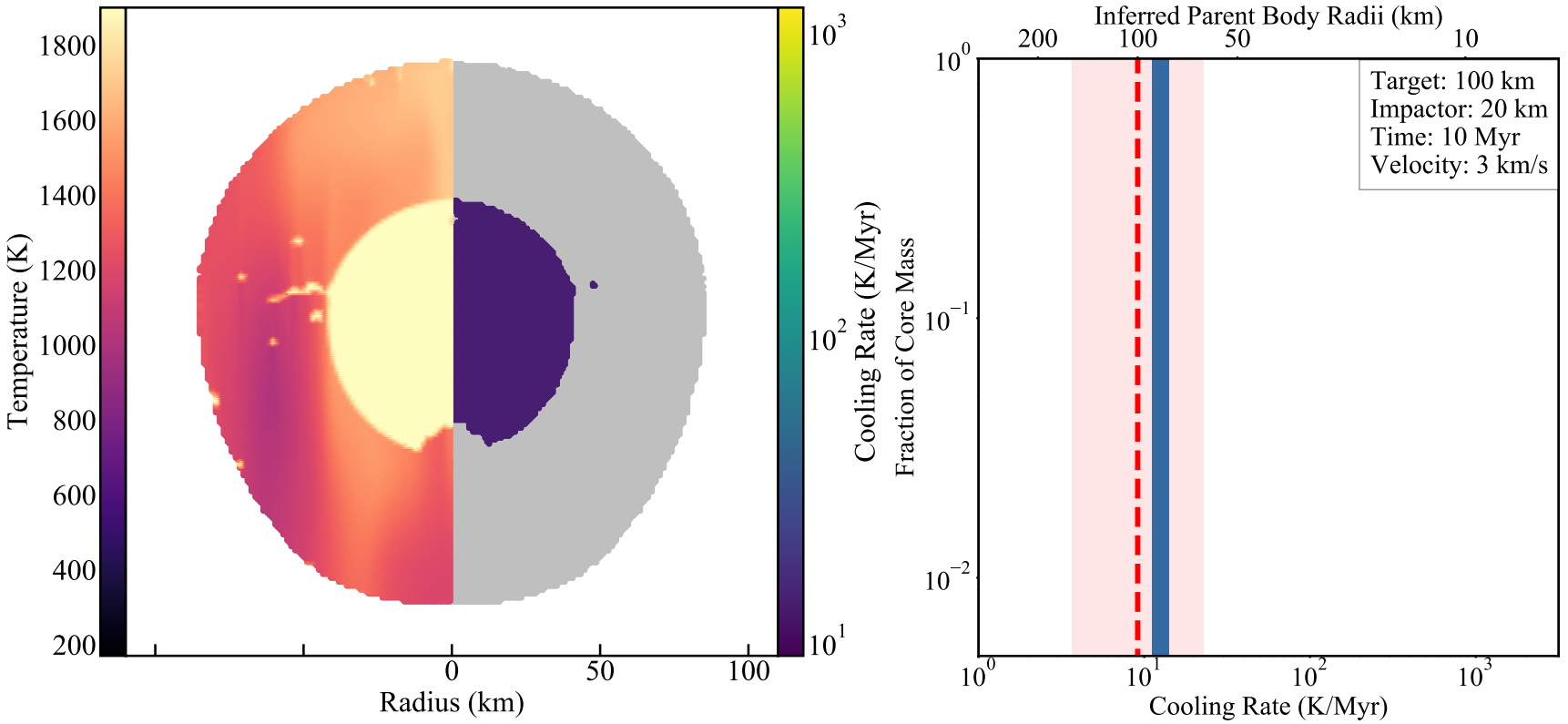

Figure 3.3: "Molten Regime:" an impact onto a 100 km radius body at 10 Myr by a 20 km radius impactor at 3 km s^{-1}. (Left) Thermal profile of the post impact body. The gray regions are silicate material and any iron with temperatures below 773 K after the impact. The length scale is identical for the the x and y-axis. (Right) A histogram of the cooling rates in the core as a fraction of the core mass. The red dashed line denotes the cooling rate of an unimpacted body with the shaded region being the estimated uncertainty of the cooling rate The top axis marks the parent body radii that would be inferred from a given cooling rate for the conventional model. As published in Lyons et al. (2019).

shear strength rather than flowing as a viscous fluid. This results in deformation of the core that is preserved throughout the simulation. Some heat is deposited in the impact, with portions of the core reaching temperatures as high as 830 K. As a result, the impact would do very little to directly change the cooling rate throughout much of the core. However, we find that material from the impactor can be buried, forming a hot plug that will cool over long timescales (Davison et al., 2012). Heat from this hot plug will diffuse into the core, warming it again, then causing it to cool through the metallographic cooling rate closure temperature of 773 K at a different rate than it had previously. This effect is seen in the histogram in Figure 3.4, which shows some secondary cooling rates. Again, whether this would have a significant effect on the Widmanstätten pattern is the focus of the work in Chapter 5.

While the two previous scenarios result in negligible or minor changes to core cooling rates, we find that significant changes occur when the planetesimal is impacted between these two time periods. During this time the mantle will cool and crystallize but the core can remain largely molten; as a result, the strength of the mantle rock can be sufficient to prevent the warm displaced metal core from settling back to the center of the body. However, to dramatically alter core cooling rates, the impact energy needs to be great enough to open a crater large enough to expose the core. An example of such a scenario is shown in Figure 3.5, which depicts the results of an impact at 6 km s^{-1} occurring 60 Myr after the onset of cooling. During the impact the transient cavity reaches the core and flips the structure of the body inside-out, bringing the inner portions of the planetesimal, including the iron in the core, near the surface (Collins et al., 2011).

The final structure of the body is shown on the left-hand side of Figure 3.6. The pools of iron close to the surface cool more quickly than larger pools buried at depth and much faster than the core material in the equivalent unimpacted planetesimal. The resulting cooling rates of iron in the target are shown in the histogram on the right-hand side of Figure 3.6. Cooling rates as high as $\sim$1000 K/Myr are seen for those materials that sit closest to the

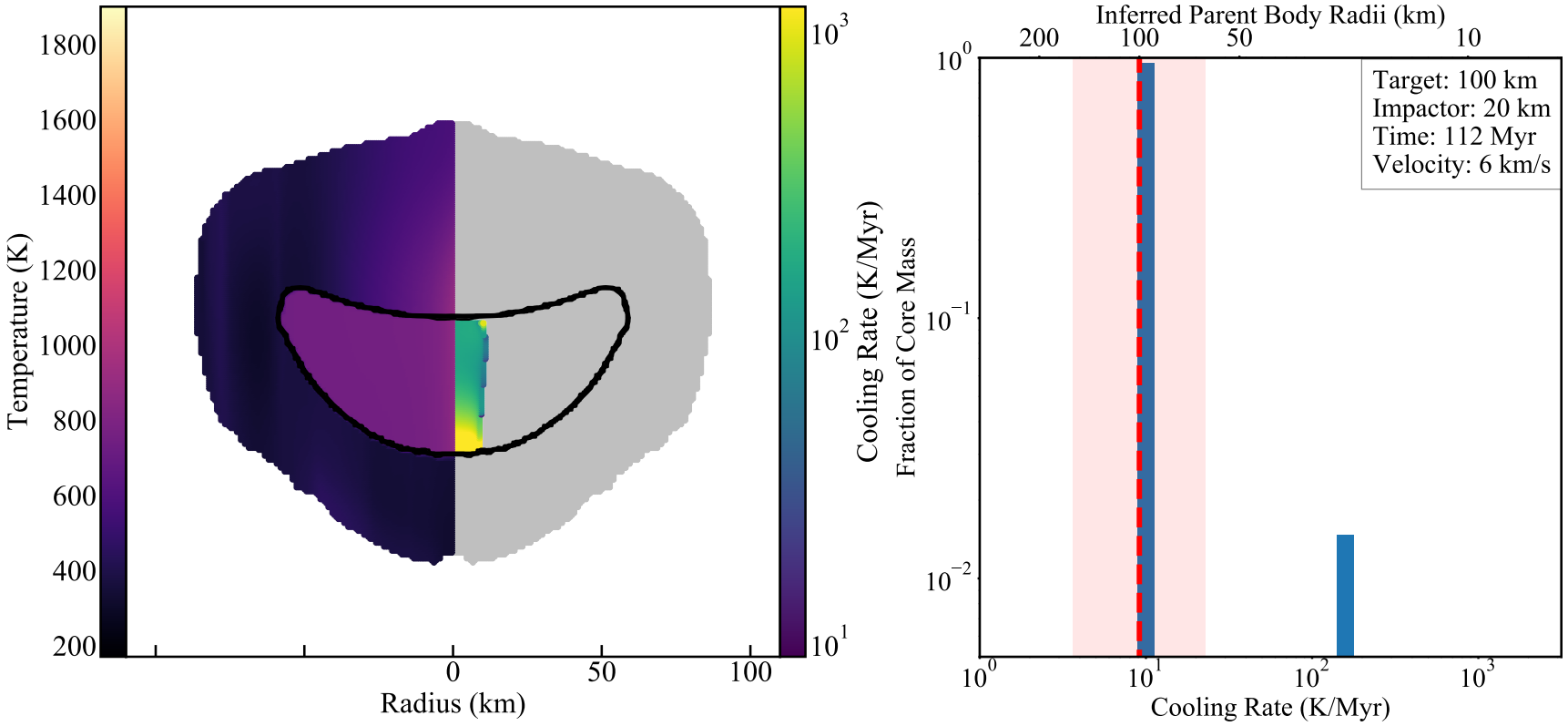

Figure 3.4: "Solid Regime:" an impact onto a 100 km radius body at 112 Myr by a 20 km radius dunite impactor at 6 km s^{-1}. (Left) Thermal profile of the post impact body. The gray regions are silicate material and any iron with temperatures below 773 K after the impact. The length scale is identical for the the x and y-axis. (Right) A histogram of the cooling rates in the core as a fraction of the core mass. The red dashed line denotes the cooling rate of an unimpacted body with the shaded region being the estimated uncertainty of the cooling rate The top axis marks the parent body radii that would be inferred from a given cooling rate for the conventional model. As published in Lyons et al. (2019).

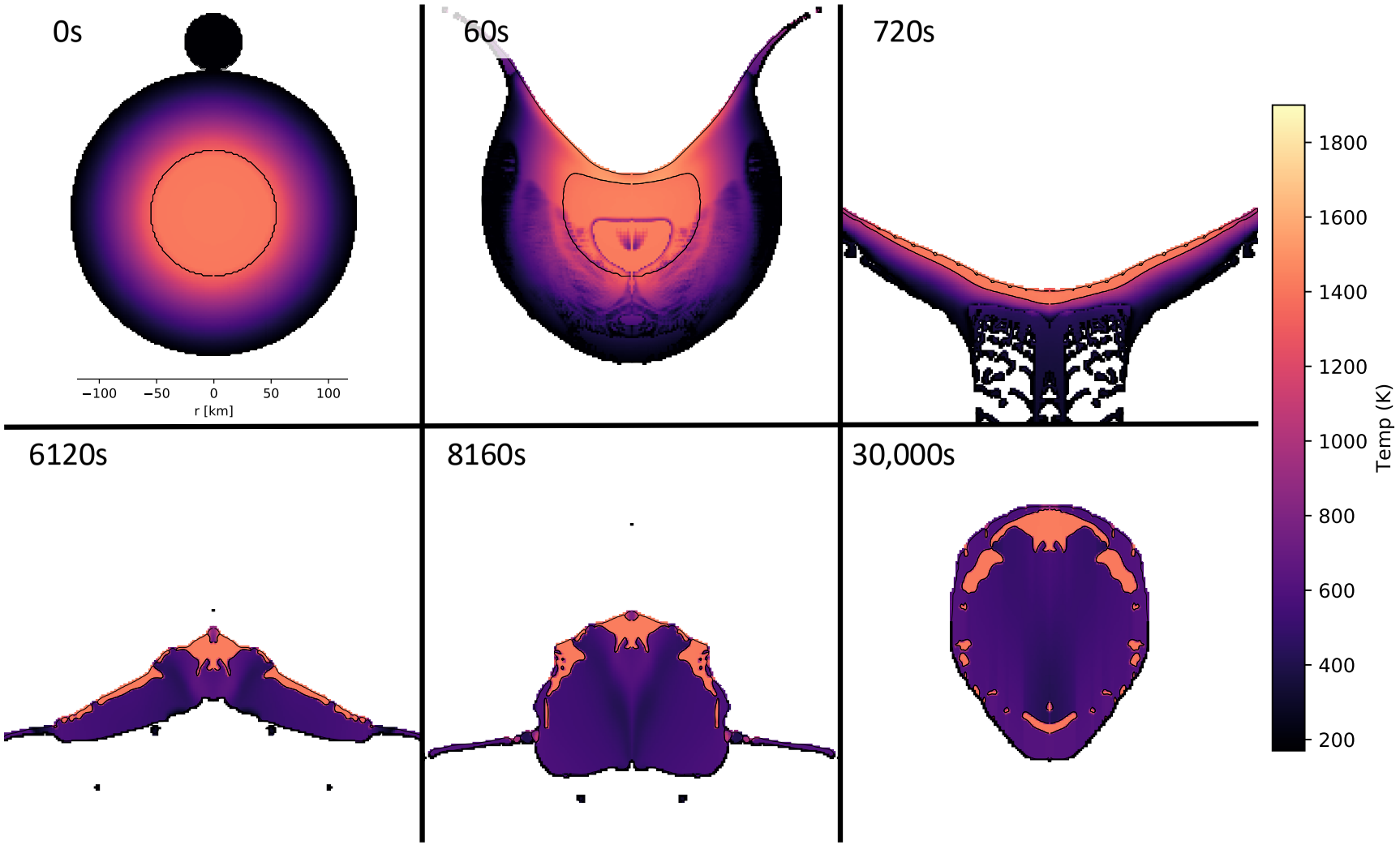

Figure 3.5: Thermal profiles at six different stages of an impact onto a 100 km radius body by a 20 km radius dunite impactor at 6 km s^{-1}. The black line denotes the boundary between iron and silicate. This impact is happening 60 Myr after the target started cooling. At this time the mantle has nearly entirely cooled but the core is still mostly molten. As published in Lyons et al. (2019).

surface, with most of the iron cooling at 100 - 800 K/Myr (as opposed to 10 K/Myr in the impact never occurred). Given that these values lie outside the uncertainty associated with the cooling rates of the unimpacted body (the gray shaded region), using even the rapid cooling, conventional models of Haack et al. (1990) it would be concluded that these meteorites sampled a parent body that was ∼20 km in radius, rather than the actual 100 km radius.

3.3.2 Time Dependence

The results above show that the timing of the collision greatly affects how a planetesimal responds to an impact. An impact that occurs when the body is largely molten or one that has cooled well below the temperatures when the Widmanstätten pattern forms results in very little change in cooling rates at 773 K compared to the unimpacted case. Impacts during the middle period of a body's thermal evolution, on the other hand, can produce large increases in cooling rates. To better understand these changes we performed a suite of impact simulations, varying the time, and thus the thermal structure of the target, when the impact occurred. Here we focus on those cases of a 20 km impactor into a 100 km radius target, considering impact velocities of both 3 and 6 km s^{-1}. We simulated impacts every 10 Myr of a 100 km body's cooling history. The distribution of cooling rates in the iron for each of these scenarios are shown in Figure 3.7. The points indicate the median cooling rate in the postimpact remnant while the vertical lines represent the range of cooling rates seen by 90% of the iron. The red dashed line again indicates the cooling rate expected in the unimpacted body and the gray shaded region is the 2.5x uncertainty on cooling rate determinations. In Figure 3.7, the impacts at 10 and 20 Myr with a 6 km s^{-1} impactor catastrophically disrupt the body leaving behind no final remnant larger than 50% of the original mass. We performed two impacts at 70 Myr because the core is very nearly solid, but has not cooled below the solidus; thus one impact simulation assumes a solid core while another assumes a molten core with a viscosity of 10,000 Pa s. The higher viscosity here

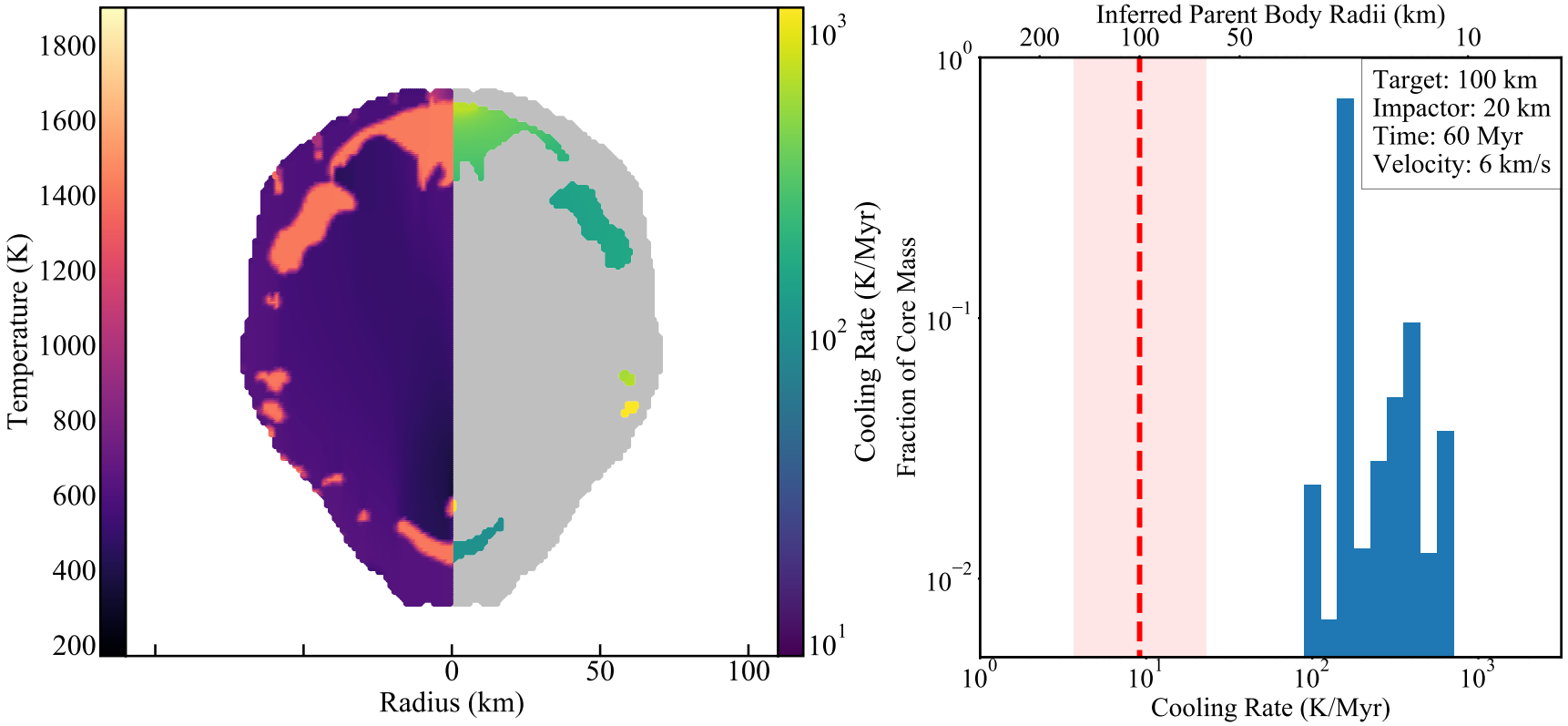

Figure 3.6: "Molten-Interior Regime:" an impact onto a 100 km radius body at 60 Myr by a 20 km radius impactor at 6 km s^{-1}. (Left) Thermal profile of the post impact body. The gray regions are silicate material and any iron with temperatures below 773 K after the impact. The length scale is identical for the the x and y-axis. (Right) A histogram of the cooling rates in the core as a fraction of the core mass. The red dashed line denotes the cooling rate of an unimpacted body with the shaded region being the estimated uncertainty of the cooling rate The top axis marks the parent body radii that would be inferred from a given cooling rate for the conventional model. As published in Lyons et al. (2019).

was chosen to describe a fluid with crystallized materials suspended within it. This higher value still allows for significant flow of the core during the impact, resulting in a similar final remnant and variations in cooling rates as in Figure 3.6.

Our simulations reveal three distinct regimes, identified in Figure 3.7, that dictate how the metal in the differentiated body is affected by the collision. In the first, "Molten Regime" the collision occurs early, before significant portions of the core or mantle solidify. In these cases, nondisruptive impacts can produce a large crater on the planetesimal, which may expose the core, but the silicate and iron flow so readily that upon relaxation, they assume a shape very similar to the pre-impact body. As a result, if the impact does not result in disruption of the target, there is very little change in the core cooling rate between the impacted and nonimpacted scenarios.

The second, "Solid Regime" corresponds to very late impacts, which occur when the mantle and core of the target planetesimal have crystallized, giving the core significant strength. In nondisruptive impacts in this regime there is little flow of the mantle and core after the impact, and instead leads to deformation. The effect on the thermal evolution of the core is thus controlled by how material is heated by the impact and cooler, outer mantle materials are mixed inwards during the impact. Both of these effects can disturb the subsequent transfer of heat in this scrambled body, but generally, these effects are minor. There is a notable exception at a particular time within this regime. Impacts 100 Myr after formation, both at 3 and 6 km s^{-1}, results in an increase and wide variation in recorded cooling rates. At this time, the temperature of the core is nearly that of the metallographic closure temperature and therefore is particularly sensitive to changes in cooling rate. As discussed in relation to Figure 3.4, some heat is deposited into the mantle due to the impact. That heat will diffuse into the core. Portions of the core in contact with unheated mantle will then cool very quickly, while those nearest to the hot plug cool slowly. The temperature range over which this reheating occurs is expected to be short but needs to be investigated further.

The third, "Molten-Interior Regime" is the period when impacts can have the greatest effect on the cooling rates of the core. This corresponds to times when the planetesimal has cooled enough that the outer mantle has largely solidified, but the core still retains enough heat that it has very low strength or is still partially molten and behaves like a fluid. Because of the weak/fluid nature of the core, it readily deforms as the crater is opened and during the subsequent relaxation. This can lead to uplift of core materials and redistribution of mantle material far away from the impact site, similar to the evolution of target material typical in the first regime. However, because of the cooler, stronger nature of the mantle, the core remains exposed or its insulation around the impact site remains thinned as the mantle rock does not flow back to envelop the core. As a result, the metal in the core can remain close to the surface of the planetesimal, either as a largely singular, coherent object with minimal insulation on top of it, or as distinct melt pools scattered throughout the upper mantle of the body. This leads to more rapid, and generally nonuniform, cooling of the metal during the subsequent thermal evolution. This regime is particularly sensitive to the S content in the core. With different bulk S values, the range of temperature and extent to which the core is molten will vary. This would likely affect the time range over which a planetesimal is classified within this regime.

The regimes identified above provide a rough guideline of how a planetesimal is affected by an impact. The details and boundaries between the regimes, however, vary with the details of the impact. For the same impactor size, low-velocity impacts do not excavate as deeply as higher velocity impacts, thus for the 3 km s^{-1} impacts the effect on the core is generally less than the 6 km s^{-1} cases considered here. Nevertheless, accelerated cooling, and increases in cooling rates, are still seen in the low-velocity scenarios, particularly in the later impacts (Figure 3.7). This is due to erosion of the silicate mantle at the sight of the impact, resulting in a much thinner insulating layer in that area. Smaller impactors at larger velocities may yield similar effects as the larger impactor cases considered here.

From our suite of simulations, and as indicated in Figure 3.7, it is clear that the thermal

structure of the target plays an important role in determining the postimpact properties of the surviving remnant. As a result, the timing of the impact will have a critical effect on the thermal evolution of the metal contained in a given parent body.

3.3.3 Effects on Different Planetesimal Sizes

In addition to the 100 km radius bodies, we investigated how impacts would have affected 50 and 200 km bodies, focusing on the "Molten-Interior Regime" for each. Because the cooling timescale is a strong function of the planetesimal radius, the absolute epoch where a planetesimal resides in this regime is different for each body. Figure 3.8 shows the final structure after two similar impact scenarios on 50 and 200 km radius targets, as well as the resulting cooling rates in each case. The 50 km body was impacted at 3 km s^{-1} by a 10 km radius impactor 15 Myr after it began to cool; a 6 km s^{-1} impact catastrophically disrupted the body. The 200 km target was impacted at 6 km s^{-1} by a 40 km radius impactor, 250 Myr into its cooling. The final structures of the planetesimals are similar, with the cores exposed near the surface of the bodies. This is a qualitatively different outcome to the distinct melt pools seen in Figure 3.6, while the transient crater reaches the core, the core is not dispersed near the surface but remains a singular chunk of metal with little to no insulating silicates around the point of impact. This, however, still results in variable cooling rates for the iron in these bodies because of the close proximity to the surface, resulting in similar variations to those observed in Figure 3.7, as shown by the corresponding histograms of cooling rates. Thus impact-induced disturbance of core cooling rates can occur within parent bodies of a variety of sizes.

3.4 Discussion & Conclusions

Until now, the detailed effects of impacts on the cooling rates of iron meteorites had not been considered in detail. Previous models either assumed no significant effects arose due

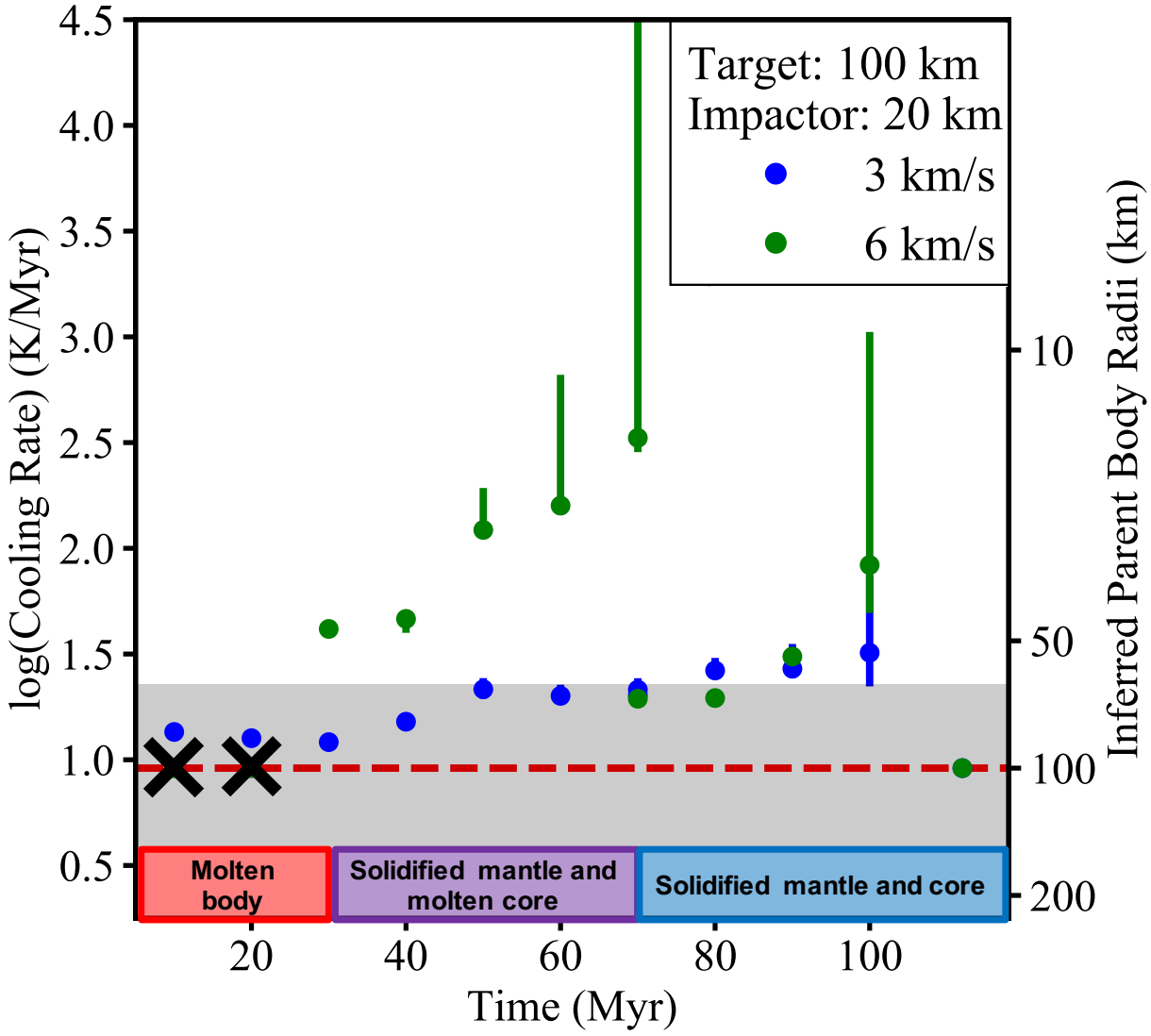

Figure 3.7: The cooling rates of the final remnants for impacts simulations onto a 100 km radius body with a 20 km radius dunite impactor at different times in the body's history. Impacts occurred at 3 km s^{-1} (blue) and 6 km s^{-1} (green). The red dashed line is the unimpacted cooling rate of the target with corresponding uncertainty in gray. The points represent the median cooling rate of the iron and the lines denote the 90% spread. The two earliest impacts, 10 and 20 Myr, at 6 km s^{-1} are catastrophically disruptive and a cooling rate is not reported. As published in Lyons et al. (2019).

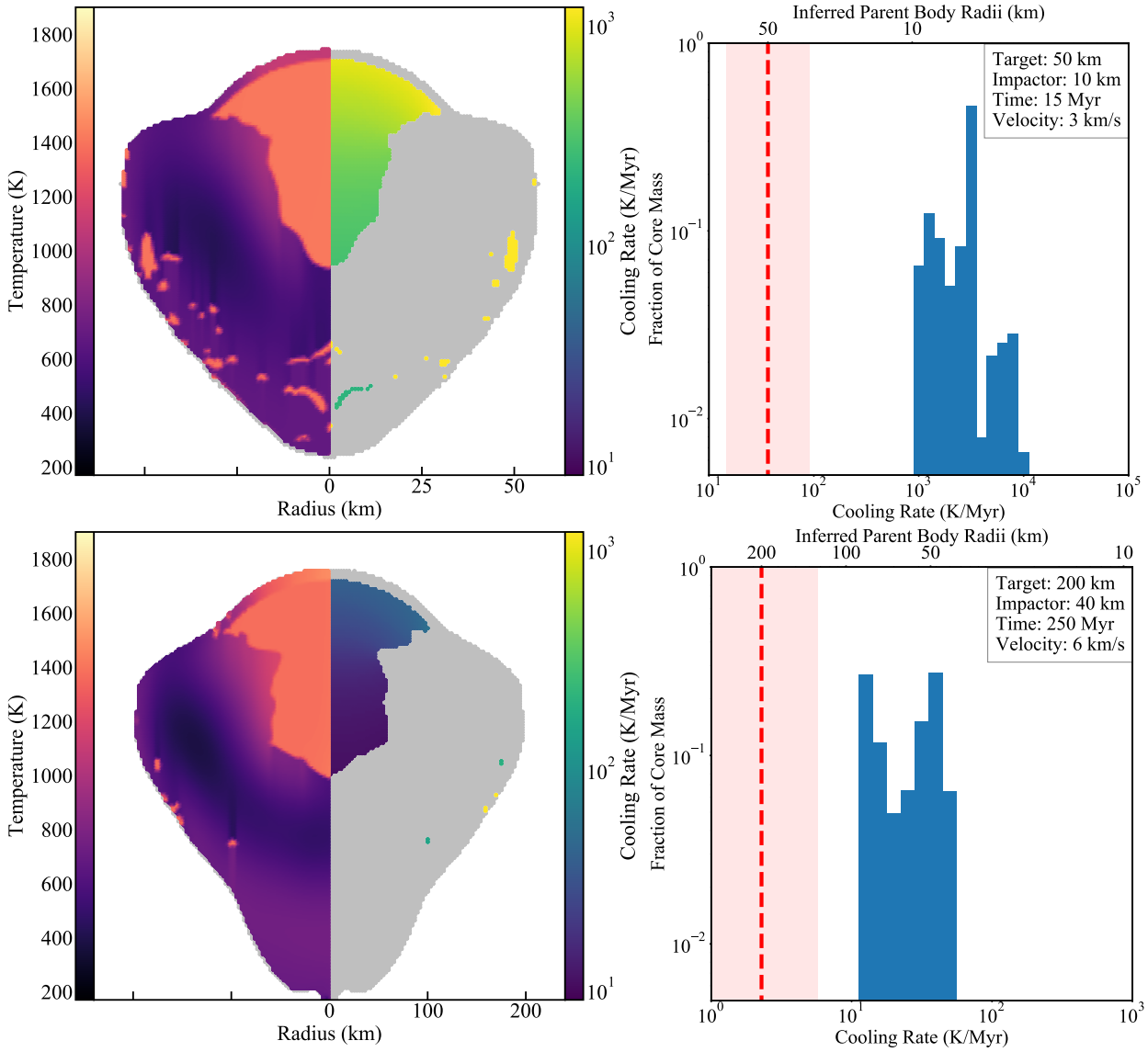

Figure 3.8: "Molten-Interior Regime:" (Left) Thermal profile of the post impact body. The gray regions are silicate material and iron with temperatures below 773 K after the impact. The length scale is identical for the the x and y-axis. (Right) A histogram of the cooling rates in the core as a fraction of the core mass. The red dashed line denotes the cooling rate of an unimpacted body with the shaded region being the estimated uncertainty of the cooling rate The top axis marks the parent body radii that would be inferred from a given cooling rate for the conventional model. (Top) Impact onto a 50 km radius body at 15 Myr by a 10 km impactor at 3 km s^{-1}. (Bottom) Impact onto a 200 km radius body at 250 Myr by a 40 km impactor at 6 km s^{-1}. As published in Lyons et al. (2019).

to impacts (Haack et al., 1990) or considered cooling of fragments that would be produced after hit-and-run impacts (Yang et al., 2011). These scenarios only represent a subset of the possible collision histories and events expected in the early Solar System. Here we have investigated the more common, high velocity, erosive collisions (Leinhardt and Stewart, 2012; Davison et al., 2013) between planetesimals in the first ∼100 Myr. We have found that such collisions can lead iron to cool at much faster rates than if such impacts did not occur. Changes in iron cooling rates appear to be most likely when the mantle is crystallized and the core behaves as a fluid. This period of a body's cooling history can last nearly 50 million years for a ∼100 km radius planetesimal, occurring roughly between 20 - 70 Myr after reaching their peak temperatures. Impacts at this time are expected to be frequent (30 - 35% of impacts in the first 100 Myr occur during this time period (Davison et al., 2013)), and impact fluxes at later times may be enhanced should dynamic instabilities arise among the giant planets (e.g. Tsiganis et al., 2005). As such, rapid cooling rates in meteorites may be a sign of these energetic events.

Iron meteorites from bodies that experienced impacts during the "Molten-Interior Regime," may record a range of cooling rates, rather than a single cooling rate as predicted if no impacts were to occur. As shown in Table 2.1, certain iron meteorite groups have samples with cooling rates that differ by nearly two orders of magnitude. In the absence of impacts, this would require a variety of planetesimals with identical compositions to form, so that these samples would be grouped together based on their chemistry, but exhibit very different cooling rates. However, if these groups sample a core from a body that was impacted as considered here, then it is possible to explain their formation in the framework of just a single parent body. Such events would provide an additional means of producing larger variations in cooling rates along with the hit-and-run impacts as reported in Yang et al. (2011).

The presence of a Ni-cooling rate relation is equally as important of a constraint on these iron meteorite groups as the variation in cooling rates. A model must describe both in order to explain these magmatic meteorites. Figure 3.6 showcases an impacted planetesimal

with increased and variable cooling rates. But due to the absence of a coherent core, the correlation between bulk Ni and cooling rate would not likely be produced. Such an impact scenario would not be the formation mechanism for iron meteorite groups in which such a relation is observed. However, as shown in Figure 3.8, there are outcomes of impacts that can result in both variations in cooling rates and maintain a large, coherent iron core. This may allow the opportunity for fractional crystallization to occur.

While the cooling rates recorded throughout a body postimpact are dependent on the timing of the impact, processes such as porosity evolution or regolith formation may affect the cooling rate further. Mantle porosity and surficial regolith would slow the cooling of the core due to their lower thermal conductivity (Warren and Rasmussen, 1987). In this study we followed the procedure outlined in Haack et al. (1990), starting with an already differentiated body at 1900 K, where melt dominates and porosity is quickly lost. In fact, porosity in planetesimals are expected to be readily lost at temperatures >700 K (Yomogida and Matsui, 1984; Hevey and Sanders, 2006), meaning such effects are likely only important when the planetesimal has cooled significantly. Further, we assumed no regolith growth on the body as well. The amount of regolith growth on a 100 km radius body is likely negligible over the short ∼100 Myr time period considered here (Housen et al., 1979; Warren, 2011). However, in cases of very rapid cooling, the time window over which significant amounts of regolith could develop and prolong cooling would be small as the temperature range over which the Widmanstätten pattern develops is only of order ∼300 K. Thus for cooling rates >100 K/Myr, the time over which the regolith would have to develop to have a significant affect on the results presented here would be limited to 3 Myr or less.

The large-scale redistribution of materials during impacts may have other effects that are important in considering the histories of iron meteorites. The iron melt pools near the surface of the body may also facilitate the excavation of this material as iron meteorites by subsequent impacts. The break-up of an entire planetesimal would not be necessary to excavate the iron and would greatly decrease the impact energy needed for their ejections

as meteoroids. Further, the flow of materials within a planetesimal may lead to mixing of silicates and metal in some regions. Fine-scale mixing cannot be resolved in our current numerical models, but significant flow, and shear, across the two materials is readily seen. Entrainment of silicates in the metal may occur in regions of very high shear, but it is unclear if materials would settle out again after the mixing. Whether such effects could play a role in the formation of stony-iron meteorites like the mesosiderites is being investigated (Bowling et al., 2017), but entrainment is likely limited to small volumes and those impacts that lead to very rapid flow of materials.

While we have demonstrated that impacts can increase the cooling rates of iron meteorites, it is worth noting that many iron meteorite groups have inferred cooling rates that are entirely consistent with cooling in the onion-shell structure of Haack et al. (1990). Another important result of our work is that the absence obvious changes in cooling rates does not imply the absence of impacts during parent body cooling. The outcome of collisions depends sensitively on the thermal state of the target at the time of impact. Those bodies which experienced large impacts in their "Molten Regime", when the mantle was largely liquid, would regain a canonical differentiated structure, with a molten core surrounded by a significant silicate mantle as shown in Figure 3.3. Such a body would then cool, with the core crystallizing in a manner that would be difficult to distinguish from the scenario if the impact had not occurred at all. The same can be said of impacts that occur during a planetesimal's "Solid Regime," when both the mantle and core have crystallized, as shown in Figure 3.1. Thus records of the impacts that iron meteorite parent bodies experienced may not exist if those impacts occurred when the body is entirely molten or solidified. Whether signatures of these impacts may be seen in samples of the mantles (achondrites) should be investigated.

CHAPTER 4

REVIEW OF WIDMANSTÄTTEN PATTERN FORMATION MODELS AND DETERMINATIONS OF IRON METEORITE COOLING RATES

The metallographic cooling rates as described in Chapter 3 are a simplification of the process by which they are inferred. The Widmanstätten pattern, a common feature of these meteorites, represents the inter-woven, cross-hatched texture that developed from the exsolution of kamacite (α, Ni poor, body-centered cubic) from taenite (γ, Ni rich, face-centered cubic) formed during the prolonged cooling that the parent bodies experienced (Wood, 1964; Goldstein and Ogilvie, 1965). Because both the growth of kamacite and the diffusion of Ni are temperature dependent processes, the sizes and Ni concentrations in each band can be used to determine the cooling rates of an iron meteorite (Wood, 1964; Goldstein and Ogilvie, 1965; Moren and Goldstein, 1978; Willis and Wasson, 1978; Rasmussen, 1981; Haack et al., 1996; Hopfe and Goldstein, 2001; Yang and Goldstein, 2006).The methods by which these cooling rates are estimated follow similar procedures as those defined nearly 50 years ago. Understanding the intricacies of inferring the cooling rates of iron meteorites requires an understanding of all the methods that are utilized and the assumptions that are built into them. Here I will review the mechanics of this growth and the various methods employed used over the last half century to model and interpret these mineral bands. I expand upon these models and examine them in the presence of impacts in Chapter 5.

The framework for understanding Widmanstätten pattern formation is as follows. The growth begins at the temperature when the iron enters the two-phase region ($\alpha + \gamma$) of the phase diagram illustrated in Figure 4.1. During cooling of the iron core, kamacite nucleates at irregular intervals throughout the taenite (Figure 4.2a). The maximum temperature at which kamacite nucleates is expected to be after phosphides begin to form, which is approximately 700 C (Hopfe and Goldstein, 2001). The details do vary, though, as the phase

diagram is sensitive to the concentration of P and subsequently P saturation which can lead to a narrower $\alpha + \gamma$ region. This can significantly affect the amount of Ni in both taenite and kamacite in the final Widmanstätten pattern. As kamacite continues to precipitate, the taenite band becomes more and more narrow, as seen in the cartoon of the growth in Figure 4.2. At the interface between the two minerals, the newly formed kamacite has the Ni concentration as determined by the solvus curve (boundary between the α and $\alpha + \gamma$ regions) at a given temperature from Figure 4.1. The taenite at the interface will also be equal to that of the solvus due to the conditions of microscopic equilibrium (de Groot, 1951). As a result, the taenite at the interface has increasingly larger concentrations of Ni than the immediately adjacent kamacite at the same temperature. The taenite at the interface also has higher Ni concentrations than other portions of the taenite band. Diffusion within the minerals works to smooth out these concentration gradients, carrying Ni from the high concentration regions at the interface to the interiors of the taenite and kamacite bands. The formation of kamacite, the movement of the boundary between the minerals as the kamacite grows, and the diffusion of Ni within them (all of which are temperature dependent) must all be modelled together to properly capture the growth of the Widmanstätten pattern.

The overall framework for Widmanstätten pattern formation is that there is a narrowing and increasing Ni content of the taenite band over time (Figure 4.2a-c). The formation ends once diffusion and grain growth slow to the point that the grain sizes and Ni-concentrations are preserved. The final product is a distinctive M-shape curve (due to their shapes) of Ni concentrations within the taenite (Figure 4.2d). As each component is temperature dependent, the rate at which a given sample cools is a great determinant of the final shape of a given Widmanstätten pattern.

One of the earliest papers exploring how cooling rates determined the properties of the Widmanstätten pattern was the seminal study of Wood (1964). Figure 4.3 illustrates the process of matching the measured Ni concentration profile of a single band to the best matching simulated growth curves. Figure 4.3a is the measured values of the (then unclassified) IAB

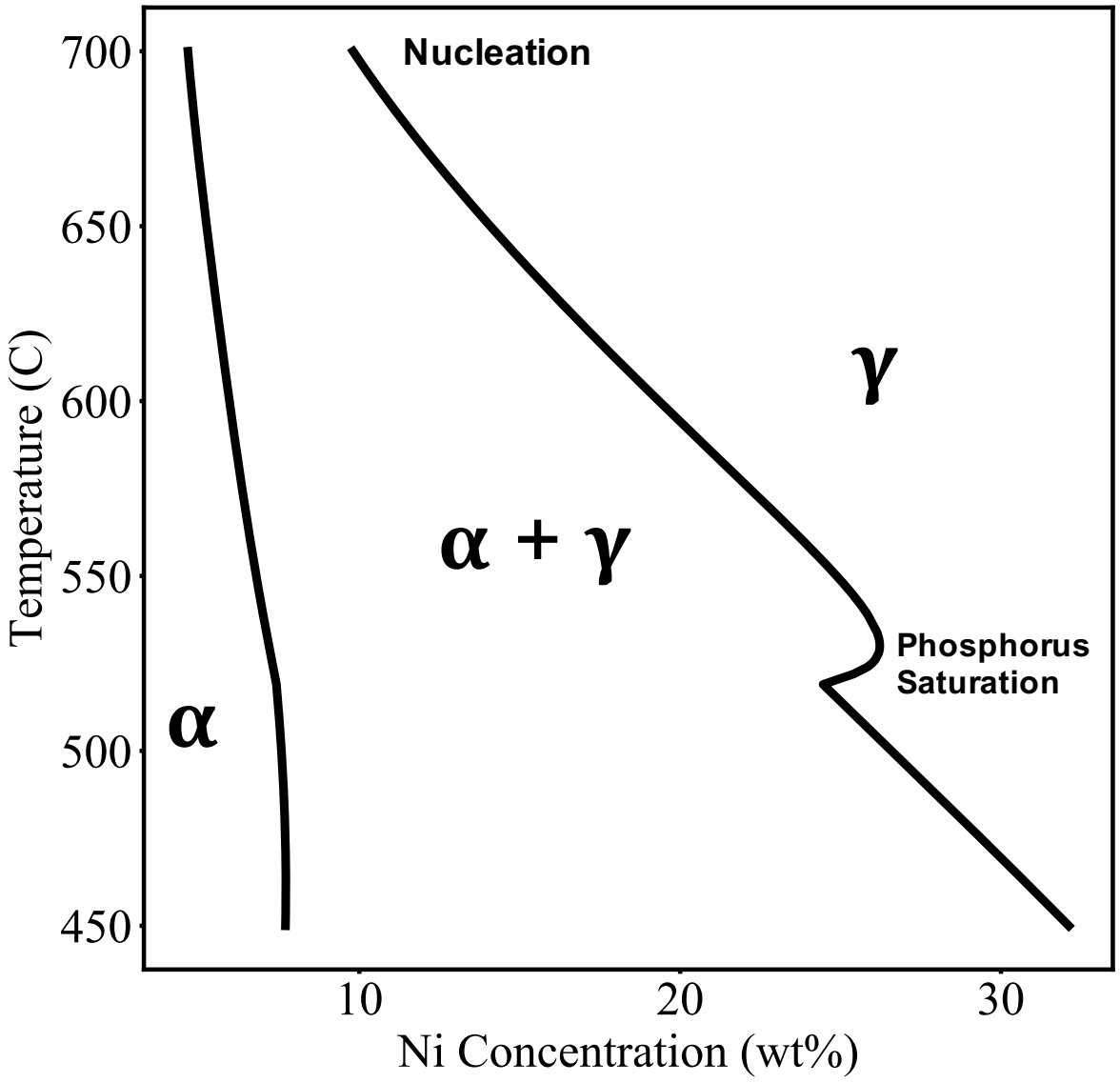

Figure 4.1: Schematic of the phase diagram, the temperature as a function of Ni concentration, of the kamacite-taenite system allowing for P saturation (the largest effect of this saturation denoted on in the figure. α is the kamacite region and γ the taenite. Adapted from Hopfe and Goldstein (2001) and Dauphas (2007).

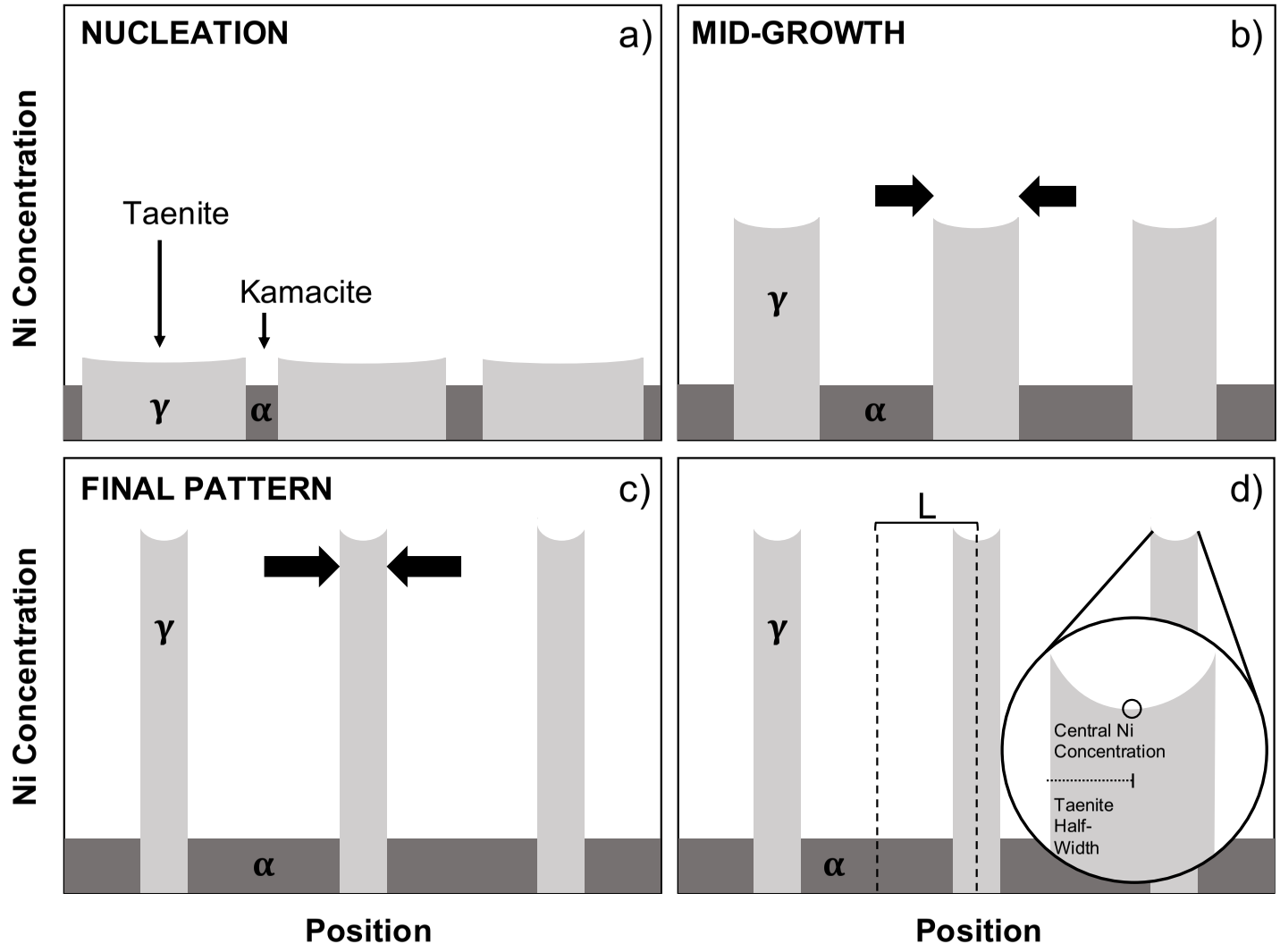

Figure 4.2: Schematic of the formation of the Widmanstätten pattern. a) shows the initial nucleation of the kamacite at regular intervals throughout the taenite. b) is an illustration of the growth of the kamacite bands as they restrict the taenite bands into smaller and smaller regions. c) is the final Widmanstätten pattern of narrow taenite bands with high Ni concentrations. d) defines key variables associated with the Widmanstätten pattern. L is the impingement length; half distance between two kamacite nucleation sites. The taenite half-width is the half the size of the taenite band. The central Ni concentration is the concentration at the center of the taenite band.

Odessa meteorite with some failed simulated curves to the right in Figure 4.3b as reported in Wood (1964). Figure 4.3c shows growth curves that more closely match the shape of the measured values with Figure 4.3d providing a best-fit match at a constant cooling rate of 1.5 C/Myr.

This work more closely explored the relationship between the central Ni concentration of taenite and the half-width of that same band and compared them to model results. Each Widmanstätten pattern in a meteorite becomes a single data point in such a relationship. However, both the central Ni concentration and the half-width are dependent on the initial distance between two kamacite nucleation sites, also known as the impingement length ("L" in Figure 4.2d). The initial impingement length for a single Widmanstätten profile is not constant throughout a given meteorite. Therefore, measurements from the same meteorite will not produce the same central Ni concentration or half-width but provide a series of points relating these two quantities. A large suite of simulations can be performed setting the bulk Ni of the meteorite and the cooling rate constant but varying the initial impingement lengths. This will produce iso-cooling-rates curves illustrating the relationship between the central Ni concentration and the taenite half-width. This process can be repeated for many cooling rate values. The iso-cooling-rate curve to which the measured meteoritic values most closely match is inferred to be the cooling rate of that meteorite. Figure 4.4 from Wood (1964) shows such diagrams for two meteorites, Canyon Diablo in Figure 4.4a and Arispe in Figure 4.4b. In each, the solid black curves denote these iso-cooling-rates with each labeled with their respective constant cooling rates. The black points are the measured values from various Widmanstätten patterns throughout the given meteorite. Via this method, the cooling rate of Canyon Diablo was found to be $\sim$0.5 C/Myr and Arispe $\sim$2 C/Myr via linear interpolation. With a 1D conductive cooling model (similar to Haack et al. (1990)), the size of the parent body was also inferred from these cooling rates, finding radii between 50 - 300 km, linking meteorite parent bodies to asteroids and not larger embryos or protoplanets.

This methodology was employed to determine the cooling rates of iron inclusions in

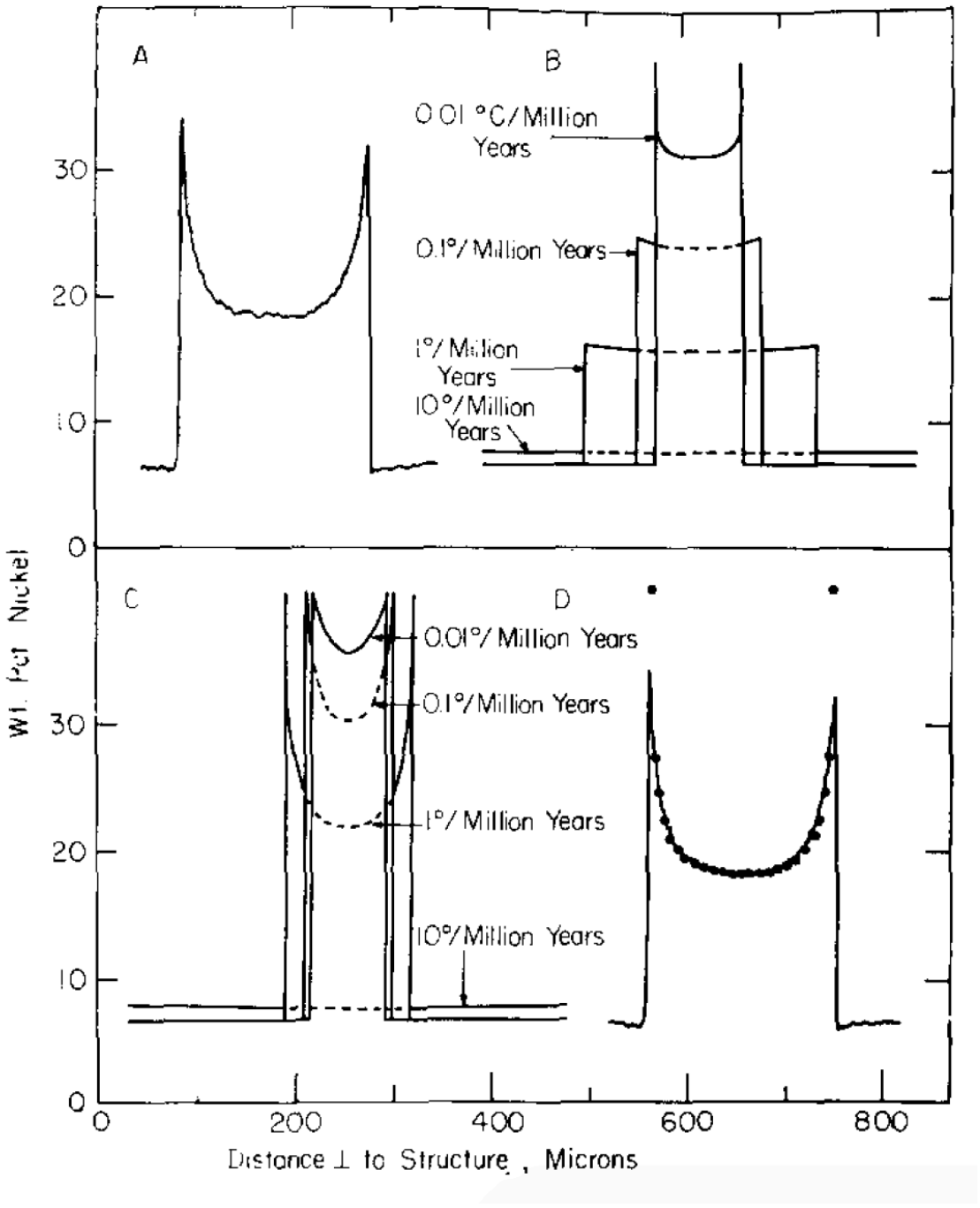

Figure 4.3: An example of the curve fitting process taken from Wood (1964) for the IAB Odessa meteorite. A) The measurements of the Ni concentration across the taenite band. B) Examples of numerical growth model results that do no match the measured curvature at all. The associated constant cooling rates are labeled. C) More numerical Ni profiles, now more closely matching the measurements. D) The final matching curve with a constant cooling rate of 1.5 C/Myr.

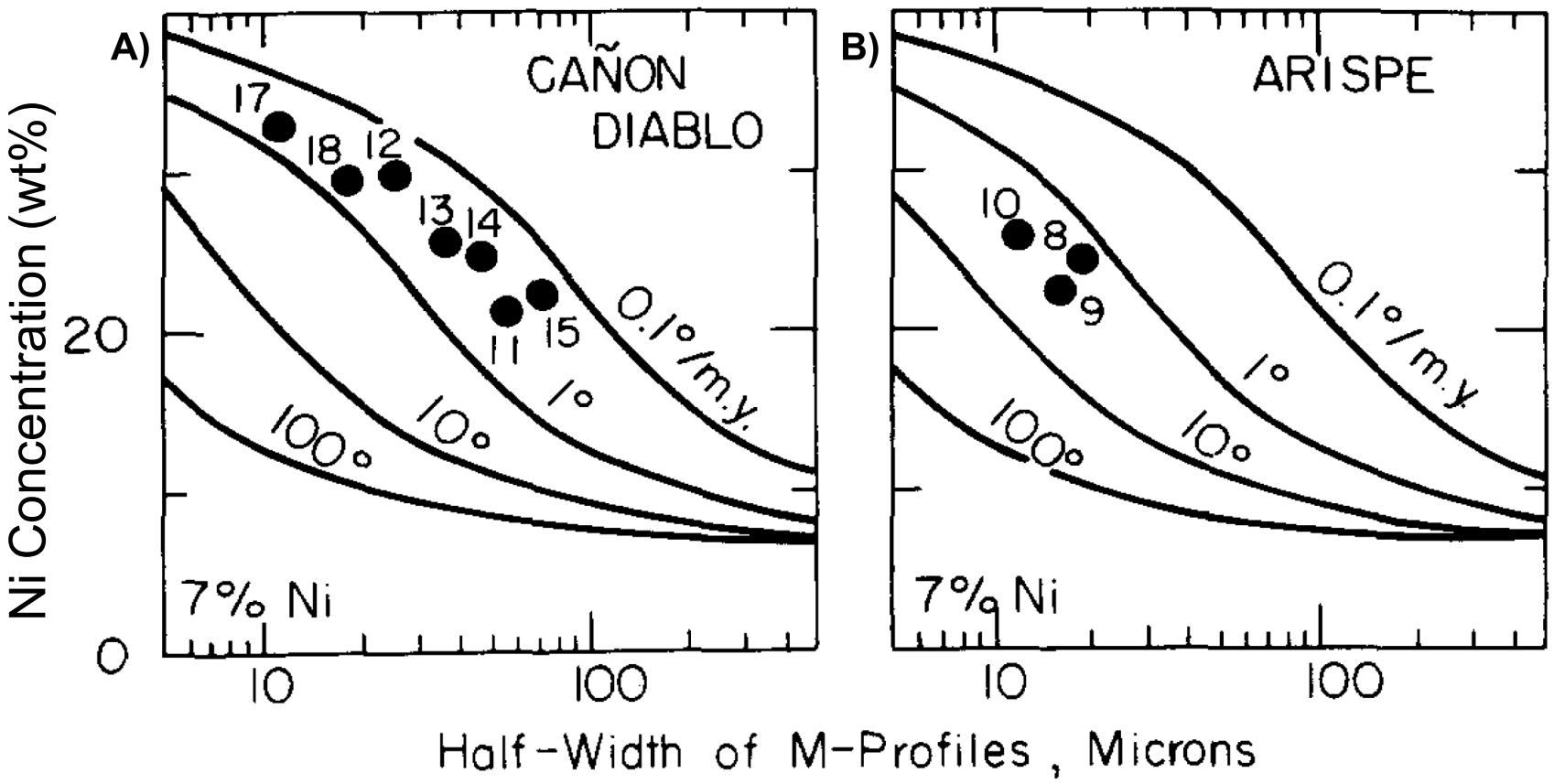

Figure 4.4: Two Wood diagrams from Wood (1964). Each meteorite plots the Ni concentration as a function of taenite half-width. The iso-cooling rate curves (black lines) determined via numerical models are plotted alongside individual Widmanstätten pattern measurements (black points). Using linear interpolation, the cooling rate of Canyon Diablo (A) to be ∼0.5 C/Myr and Arispe (B) to be ∼2 C/Myr.

chondritic meteorites Wood (1967). From these cooling rates, along with a 1D cooling code of a spherically symmetric chondritic planetesimal, the depth at which the chondrites originated from within their parent bodies were estimated. Matching measured Widmanstätten pattern central Ni concentrations and taenite half-widths with numerical models would go on to be a common method in which to determine metallographic cooling rates, with the central Ni concentration vs. taenite half-width being dubbed the "Wood Diagram" (Moren and Goldstein, 1978; Haack et al., 1996; Yang and Goldstein, 2006).

The Widmanstätten growth models proved useful in determining the properties of the original parent body (Goldstein and Ogilvie, 1965). Numerical models were tested against highly precise electron microprobe measurements of the Ni profiles. The sizes of the parent bodies were taken into account in the numerical models by factoring in the internal pressures. Doing so introduced pressure dependent Ni diffusion coefficients, a high-pressure phase diagram for the kamacite-taenite system (up to 50 kbar), and an adjusted nucleation temperature taking into account undercooling. Undercooling occurs when kamacite does not nucleate when it enters the three-phase region but only once it reaches an even lower temperature. What causes this delay in kamacite formation is not well understood and is beyond the scope of this review. Figure 4.5 illustrates their findings with curves looking at the expected kamacite size as a function of planetesimal radius. Each curve looks at an increasing amount of undercooling. The larger the parent body, the slower the cooling in the core. This increase in time for diffusion leads to a larger kamacite band. At a radius of $\sim$500 km (4 kbar), any further increases in pressure result in the kamacite band width to sharply decrease. Beyond 800 km radius (>10 kbar) the kamacite bands would not grow nearly large enough to match any known iron meteorites. Therefore, larger bodies will not form Widmanstätten patterns in the center of their cores (outer regions of the core may remain below the pressure threshold depending on the parent body size). This creates a threshold of < 12 kbar and a maximum parent body size of $\sim$800 km in radius. This upper bound on parent body sizes implies that iron meteorites have asteroidal origins (a similar

conclusion to that of Wood (1964)).

The metallographic cooling rates of the IVA iron meteorite group came under further scrutiny in multiple papers in 1978, each utilizing the Widmanstätten pattern. Both Moren and Goldstein (1978) and Willis and Wasson (1978) estimated the cooling rates of several iron meteorites in the IVA group. In each case, a numerical model (similar to those described above) was used to model the growth of the Widmanstätten pattern and compare the measured values to the iso-cooling-rate curves of the Wood Diagram. Moren and Goldstein (1978) found a nearly order of magnitude variation in cooling rates between meteorites within the IVA group, which would be corroborated by future works. They suggested the IVA meteorites would need to sample multiple parent bodies, as a single parent body would only exhibit (nearly-) uniform cooling rates. However, Willis and Wasson (1978) found only a factor of two variation in the cooling rates and proposed a single parent body for the IVA group. Moren and Goldstein (1978) attributed the discrepancy in cooling rates between the two studies to differences in the choices of Ni diffusion coefficient, parameterization of the effect P has on the diffusion coefficient, and the Ni solubility in kamacite. The cooling rate discrepancies can be best seen in Figure 4.6 which compares the Wood diagrams from each study for the meteorite Gibeon. Moren and Goldstein (1978), Figure 4.6a, found a cooling rate of 35 - 40 C/Myr where Willis and Wasson (1978), Figure 4.6b, found a cooling rate of 25 C/Myr. Altogether, the differences in cooling rates, their variations, as well as subsequent inferences about the parent bodies, showcase the sensitivity of the published metallographic cooling rates to the underlying numerical models and assumptions that go into them.

Rasmussen (1981) determined an improvement to the canonical Widmanstätten pattern growth model in which the starting Ni concentration for a given simulation is set by local bulk concentration in the area of the lamellae in question, instead of for the bulk meteorite. The Ni concentration throughout a meteorite can vary on the scale of cms. This consideration can change the initial Ni concentration by nearly 20% compared to bulk values. Although, such variations have not been observed in subsequent studies (Yang and Goldstein, 2006). For the

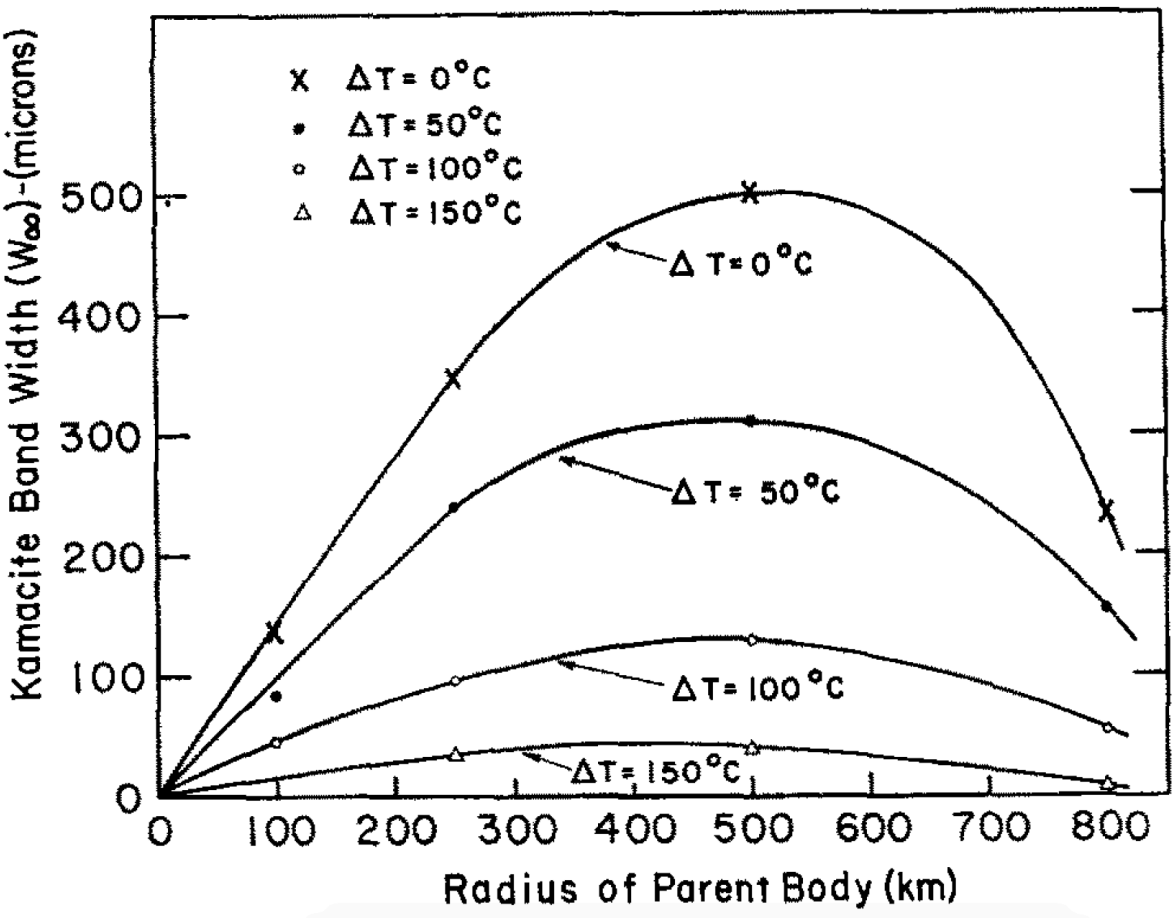

Figure 4.5: Results of numerical models of Widmanstätten pattern growth for various sized planetesimals (larger the radius, the higher the pressure during formation) as reported in (Goldstein and Ogilvie, 1965). Each curve assumes a given amount of undercooling labeled as ΔT. The larger the parent body, the slower the cooling in the core. This increase in time for diffusion leads to a larger kamacite band. However, pressure is also increased and impedes the growth of kamacite after $\sim$500 km (4 kbar). Beyond 800 km (10 kbar) the kamacite bands are smaller than any known recorded values.

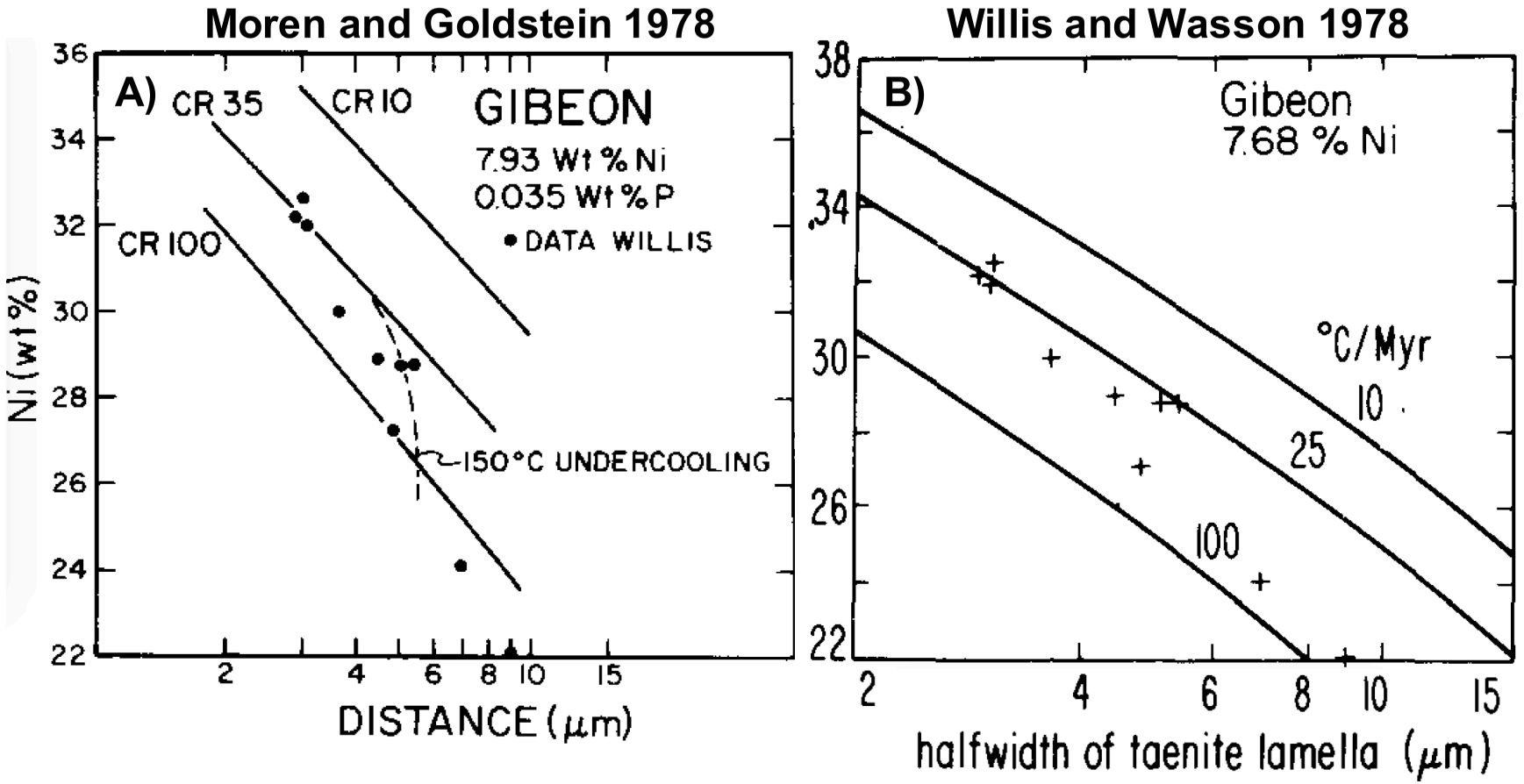

Figure 4.6: A comparison of two Wood diagrams for the determination of the cooling rate of the IVA meteorite Gibeon from A) Moren and Goldstein (1978) and B) Willis and Wasson (1978). Moren and Goldstein (1978) found a cooling rate of 35 - 40 C/Myr where Willis and Wasson (1978) found a cooling rate of 25 C/Myr. In addition to the difference in average cooling, the range of values is nearly an order of magnitude in Moren and Goldstein (1978)

Cape York meteorite in the IIIAB family, the Ni concentration increases 7.84 to 9.39 wt% for the specific case seen in Figure 4.7. Figure 4.7a is the best fit utilizing the conventional method (bulk meteorite) and Figure 4.7b is the fit with the local Ni concentration. The author claimed this adjustment allowed for a more accurate model of the entirety of the M-profiles. Not only did the central Ni concentration and the half-width match, but the curvature of the Ni profile in the taenite band had a better fit. In turn, the cooling rate was expected to be more accurately inferred. The cooling rates found using this method could increase or decrease by nearly an order of magnitude compared to using only the bulk Ni concentration. However, this method was not widely adopted.

Widmanstätten pattern growth models were later applied to the stony-iron mesosiderites in Haack et al. (1996). In this work, not only were the Wood diagrams utilized to constrain the cooling rates, but also central Ni concentration vs. half-width plots for the kamacite lamellae of the Widmanstätten pattern. The combination of these methods provided a check to the inferred cooling rate from an individual pattern and therefore a check on the underlying numerical growth model. This method determined that the mesosiderites cooled at a rate less than 0.5 C/Myr with exact values between 0.02 - 0.03 C/Myr, which is more slowly than any previously recorded iron meteorites. In order to achieve such slow cooling rates, a parent body between 200 - 400 km in radius would be needed, depending on the many assumption made in the thermal models such as iron fraction in the original chondritic material and (mega)regolith thickness. This study also marked the first consideration of variable cooling rates during the cooling of a meteorite parent body and its effect on the Widmanstätten pattern growth. Although only briefly noted, an instantaneous change of cooling rates from 1 C/Myr to 0.02 C/Myr at 425 C was modeled and shown to differ from the iso-cooling rate curves in a Wood Diagram.

An updated the phase diagram for the kamacite-taenite system was published in Hopfe and Goldstein (2001). Here, the effect of P in the metal (in particular P saturation) was quantified and a polynomial fit was determined for both the binary Fe-Ni and ternary Fe-Ni

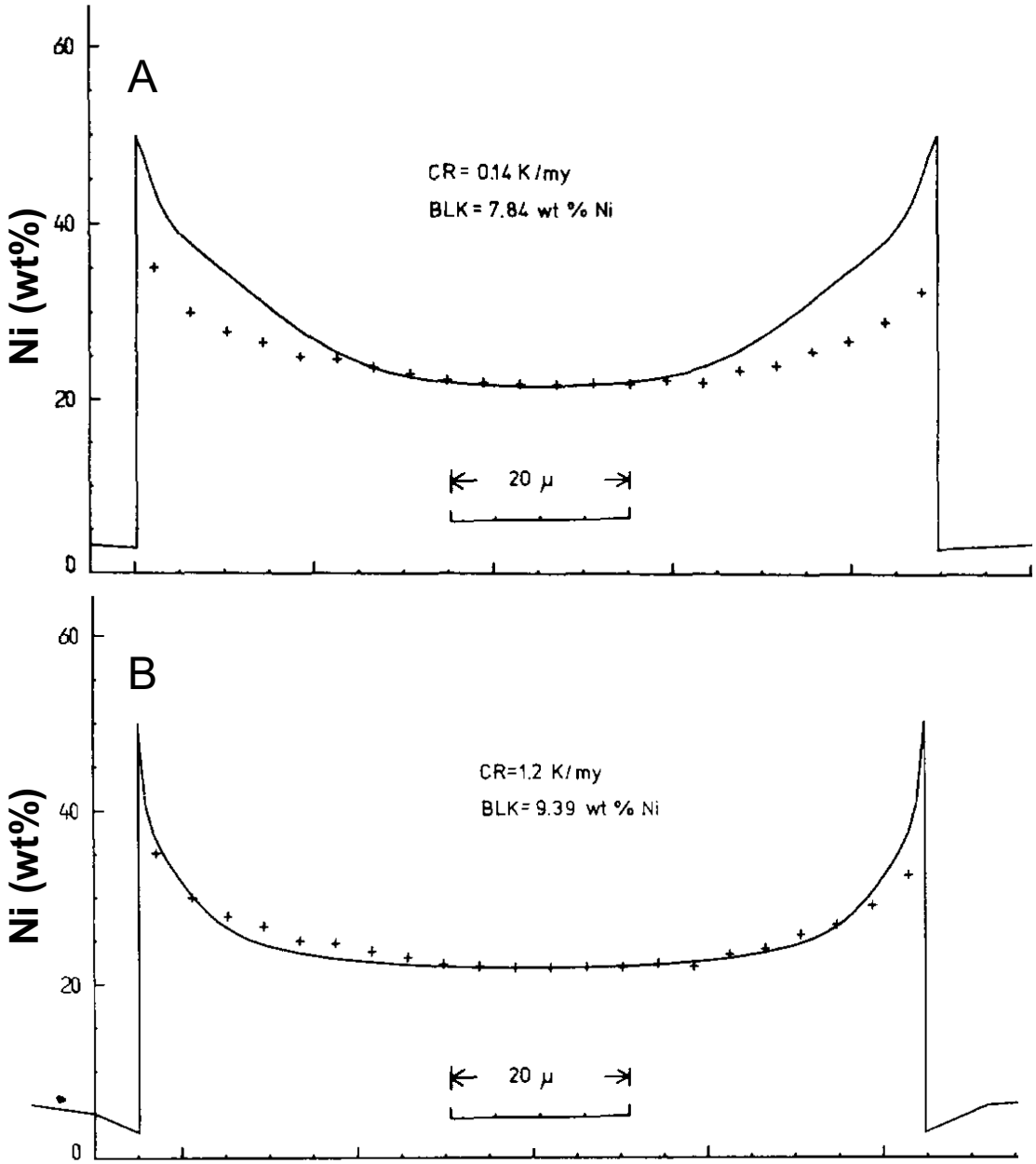

Figure 4.7: Curve fitting examples from Rasmussen (1981) illustrating their localized Ni corrections. A) The best fit curve for a sample Widmanstätten pattern from the IIIAB Cape York meteorite. The numerical model (black line) uses the bulk Ni concentration of 7.84 wt% and does not match the overall curvature of the measured values (black marks). The numerical fit has a constant cooling rate of 0.14 C/Myr. B) The best fitting numerical model now with a locally measured Ni concentration of 9.39 wt%. This better fitting numerical curve is produced with a constant cooling rate of 1.2 C/Myr, nearly an order of magnitude increase compared to the uncorrected value.

(P saturated) solvus lines. This parameterization of the phase diagram would be utilized in many subsequent works. Diffusion coefficients were also updated to include the effects of P saturation. Their phase diagram is utilized in this Thesis in Chapter 5 and is illustrated in Figure 4.1. They presented a detailed look at the effects of cooling rates, P concentration, and diffusion coefficients on the shapes of the final M-shape curves for growth models, the Wood diagrams, as well as the equivalent diagram for the kamacite lamellae. Their model was tested on the mesosiderites in direct comparison to Haack et al. (1996). They found the mesosiderites cooled at ∼0.2 C/Myr, which was nearly an order of magnitude faster than values reported in Haack et al. (1996). This work marked a major revision to many of the historically used physical properties of the growth models.

Yang and Goldstein (2006) corrected for the orientation of the kamacite-taenite grains during laboratory measurements, refining cooling rate determinations. A given iron meteorite sample is cut and polished with an unknown orientation with respect to the Widmanstätten growth plane. Taking measurements along the Widmanstätten pattern on the surface can result in M-shaped curves with incorrect half-widths and distorted curvatures. Determining the true orientation and geometrically correcting the measured values can change the inferred cooling rates significantly. This correction is done by picking two surfaces and finding the angles of each compared to a shared edge. Using these angles, and crystallographic geometry, the angle between the current polished surface and the growth plane can be determined. With this angle, the true taenite half-width can be determined by multiplying the apparent half-width by the sine of the angle. An updated taenite half-width, along with a numerical Widmanstätten pattern growth model, can provide an updated cooling rate. For the case of the Casas Grandes IIIAB meteorite, the increase in cooling rate is nearly 2.5x. Similarly, the IIIAB Bella Roca meteorite, for which the Ni concentration measurements across the taenite band featured in Figure 4.8a, had an increase in cooling rate. Figure 4.8b showcases the change in taenite half-width when the orientation correction is applied (dark circles). This results in a cooling rate that is 4.0x faster than previously reported. These correc-

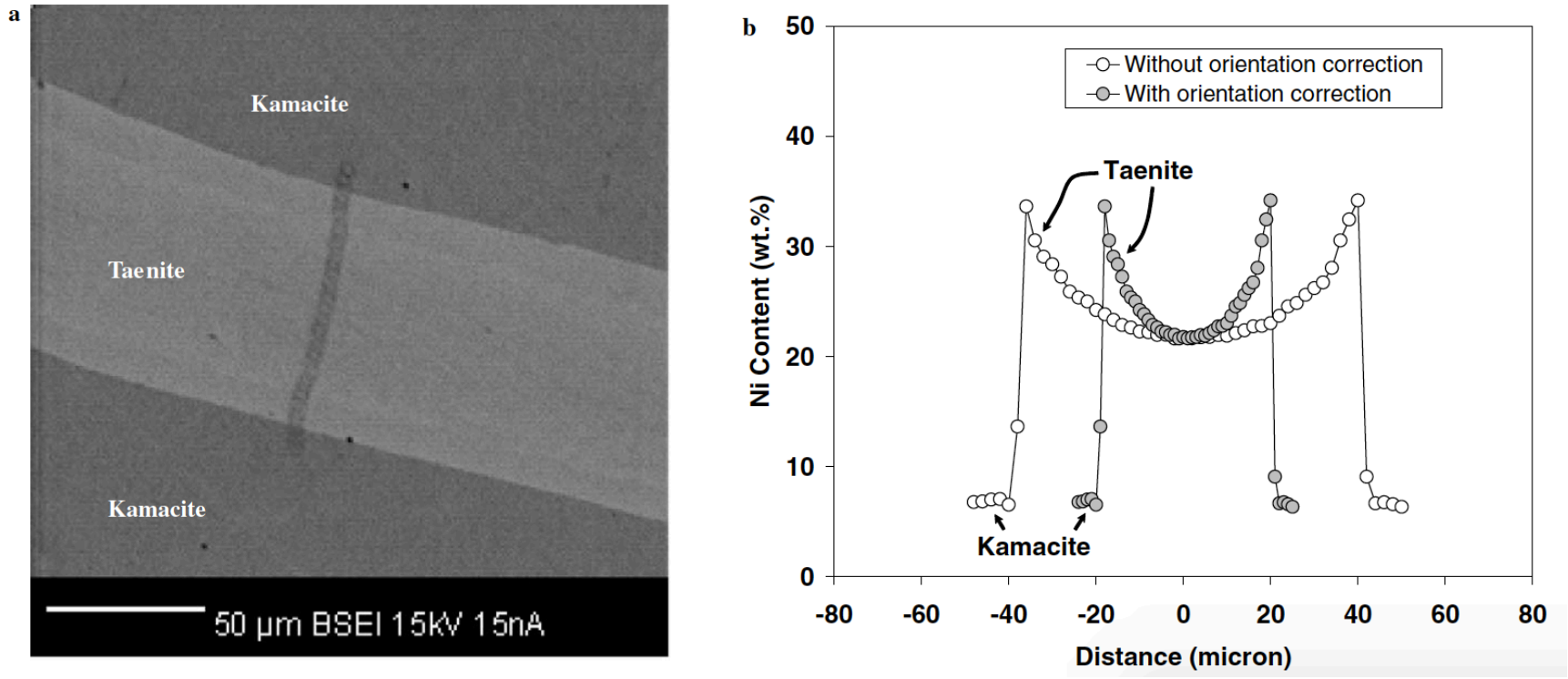

Figure 4.8: Example of the orientation correction as published in Yang and Goldstein (2006). A) The Ni concentration measurements across the taenite band of the IIIAB Bella Roca meteorite. The darker circles are the individual measurements. B) The resulting Ni profile is plotted in as the white circles, with no corrections made. The numerical model best fit (black line) fits these data points well. The shaded circles are the corrected positions and nearly half the taenite half-width resulting in a cooling rate nearly 4x faster.

tions can only increase the estimated cooling rates because the half-width of the corrected taenite band can only decrease in size. They propose such uncorrected samples to be the reason behind exceptionally slow cooling rates determined in previous studies, particularly the mesosiderites. Slow cooling rates often times produce very narrow taenite half-widths because of the increased growth times (all other things remaining unchanged). The uncorrected geometry would naturally decrease the cooling rates of any given meteorite group. A systematic increase in cooling rates across all meteoritic groups would also decrease the expected radii of each respective parent body (Haack et al., 1990).

In the following chapter I will detail work addressing a key assumption of these Widmanstätten pattern growth models discussed in this chapter that had yet to come under scrutiny; constant cooling rate throughout the growth of the Widmanstätten pattern.

CHAPTER 5

WIDMANSTÄTTEN PATTERN RESPONSE TO IMPACT EVENTS

5.1 Introduction

Early models for the thermal evolution of differentiated planetesimals predicted that the cores would cool uniformly (at a relatively constant rate) as a result of the high thermal conductivity of iron as well as the insulation provided by the silicate mantle surrounding it (Haack et al., 1990). Any given sample from a planetesimal core was expected to have the same or similar cooling rates. However, rapid cooling rates and nonuniform cooling can be produced in a single metallic core if the insulating silicate mantle and regolith was significantly thinned (Yang et al., 2008; Lyons et al., 2019). Impacts among planetesimals are expected while planetesimals are cooling during the first 10 – 100 Myr of Solar System history, as the growing planets and embryos scattered small bodies during their accretion and dynamical restructuring (Davison et al., 2013). The types of collisions that would occur would range from low-velocity hit-and-run encounters that could strip the mantle off of the differentiated planetesimals and embryos, leaving a predominantly iron body behind (Asphaug, 2010), to high-velocity impacts that would erode the outer layers of planetesimals and excavate their hot interiors (Chapter 3). Yang et al. (2008) demonstrated that the rapid cooling observed in the IVA meteorite group, and the correlation of Ni concentration and cooling rates could be reproduced by the cooling of a body that experienced such an event.

In estimating the cooling rates, models for Widmanstätten pattern growth, which track the sizes of mineral grains and concentrations of Ni, are used to compare to the observed structures in the iron meteorites. To date, these models have assumed constant cooling rates during the period of Widmanstätten pattern growth (Wood, 1964; Moren and Goldstein, 1978; Hopfe and Goldstein, 2001; Yang et al., 2008). However, collisions of the type described above would yield significant changes or nonlinear cooling histories of the metal

contained within a given planetesimal. Here we investigate how the Widmanstätten pattern develops under variable cooling histories expected for impacted planetesimals and the implications for identifying signatures of collisions in iron meteorites. We outline our modeling procedure and compare constant and variable cooling rates in Section 5.2. Section 5.3 looks at specific examples of nonmonotonic cooling associated with impacts, and we conclude with a discussion on the constraints of observing these examples in the meteoritic record in Section 5.4.

5.2 Methodology

The cooling rates for iron meteorites are often determined by comparing measured elemental concentrations across the taenite and kamacite bands of the Widmanstätten pattern in iron meteorite samples to numerical models of the pattern's growth. The methods by which these cooling rates are estimated follow similar procedures as those defined over 50 years ago (Wood, 1964). In this work we will focus on two such methods: the Wood Diagram and fitting the taenite Ni concentration profile (curve fitting).

Both approaches require the Widmanstätten pattern formation to be numerically modeled in order to compare to meteoritic measurements. The formation of kamacite, the movement of the boundary between the minerals as the kamacite grows, and the diffusion of Ni within them (all of which are temperature dependent) must all be modeled together to properly capture the growth of the Widmanstätten pattern. The distinctive M-shape curve of Ni concentrations within the taenite (Figure 4.2d) is the final product the many processes. These profiles are seen in iron meteorites, and comparisons between the model predictions and data can be used to determine the cooling history of those samples. The numerical profile most closely matching the measurements in the meteorite is used to infer the cooling rate that the iron experienced (Wood, 1964; Rasmussen, 1981; Yang and Goldstein, 2006). In addition to the curve fitting method, researchers have used the relationship between the central Ni concentration and half-width of a collection of individual taenite bands within

a given sample as a basis for comparing meteoritic properties to model results (Wood Diagram). The iso-cooling-rate curves to which the measured values most closely match is inferred to be the cooling rate for that group (Wood, 1964; Moren and Goldstein, 1978; Haack et al., 1996; Yang and Goldstein, 2006).

5.2.1 Numerical Model

The numerical model used here to simulate the growth of the Widmanstätten pattern adopts a front-tracking, fixed finite-difference grid method described by Crank (1984) and is adapted from that described in Dauphas (2007). We model the region between two kamacite nucleation sites, which defines the initial impingement length, "L" (Figure 4.2d). This represents our full computational zone, which is broken up into 100 - 500 of grid cells of width δx. We track the change in concentration of Ni and widths of the kamacite and taenite bands as the system cools from the nucleation temperature of kamacite based on the assumed composition of the meteorite to the metallographic closure temperature of 450 C, which is the temperature at which the diffusion of Ni is so slow that changes in Ni concentration and grain sizes essentially cease.

The concentration of Ni is calculated as a function of time using Fick's second law:

$$\frac{\partial C}{\partial t} = \frac{\partial D}{\partial x}\frac{\partial C}{\partial x} + D\frac{\partial^2 C}{\partial x^2} \tag{5.1}$$

with C being the concentration in wt% and D is the diffusion coefficient. This equation is evaluated using the Iterated Crank-Nicholson (ICN) scheme. We calculate the new C at each grid point using a finite difference, forward time centered space scheme (FTCS). The diffusion coefficient for kamacite, D^{α}, is constant at a given temperature while the taenite D^{γ} coefficient is calculated as a function of Ni and P concentration (Hopfe and Goldstein, 2001). The concentrations are symmetric across the left and right boundaries of the computational grid (no flux). The time step is determined by the grid spacing, the diffusion coefficient of

kamacite (since it is larger than the taenite diffusion coefficient at the same temperature), and the stability factor M; such that $dt = \frac{dx^2}{MD^\alpha}$. The value of M needs to be larger than 2 to guarantee that the integration is stable. Larger values of M lead to smaller time steps and greater resolution. We adopt a value of 250 as it was the smallest value at which numerical effects of the ICN method were not discernible.

The position of the kamacite-taenite interface moves as the temperature decreases and kamacite becomes more abundant. An interpolation of the Lagrangian type is used to calculate the first and second derivatives for the two cells around the interface (Crank, 1984). During each time step, the concentration is determined and the displacement of the interface due to the growth of the kamacite band is calculated. The calculations are outlined in more detail in Dauphas (2007).

5.2.2 Model Validation

The numerical approach outlined above is necessary as no analytic solution to the coupled growth of minerals and diffusion of Ni exists. However, Jost (1952) outlined a simplified, though unphysical, scenario in which the diffusion coefficients, boundary concentrations, and interface concentration were set to constant values, allowing an analytic solution for the Ni-concentration to be derived. We have applied our model to simulate this same situation to validate our numerical methodology. The analytical solution for the concentrations within each phase as well as the position of the interface are fully described in Jost (1952) as well as Dauphas (2007). Figure 5.1a shows the profile and agreement between the model and the analytic solution. There is extremely good agreement with respect to the calculated interface position of 1.548 (identical to 6 significant figures) as well as the overall concentration profile to the analytic solution.

We also used our model to reproduce the full Widmanstätten growth results reported in Hopfe and Goldstein (2001) and Dauphas (2007). Assuming a bulk Ni concentration of 8.14 wt%, P concentration of 0.16 wt%, an initial impingement length of 700 μm, and a constant

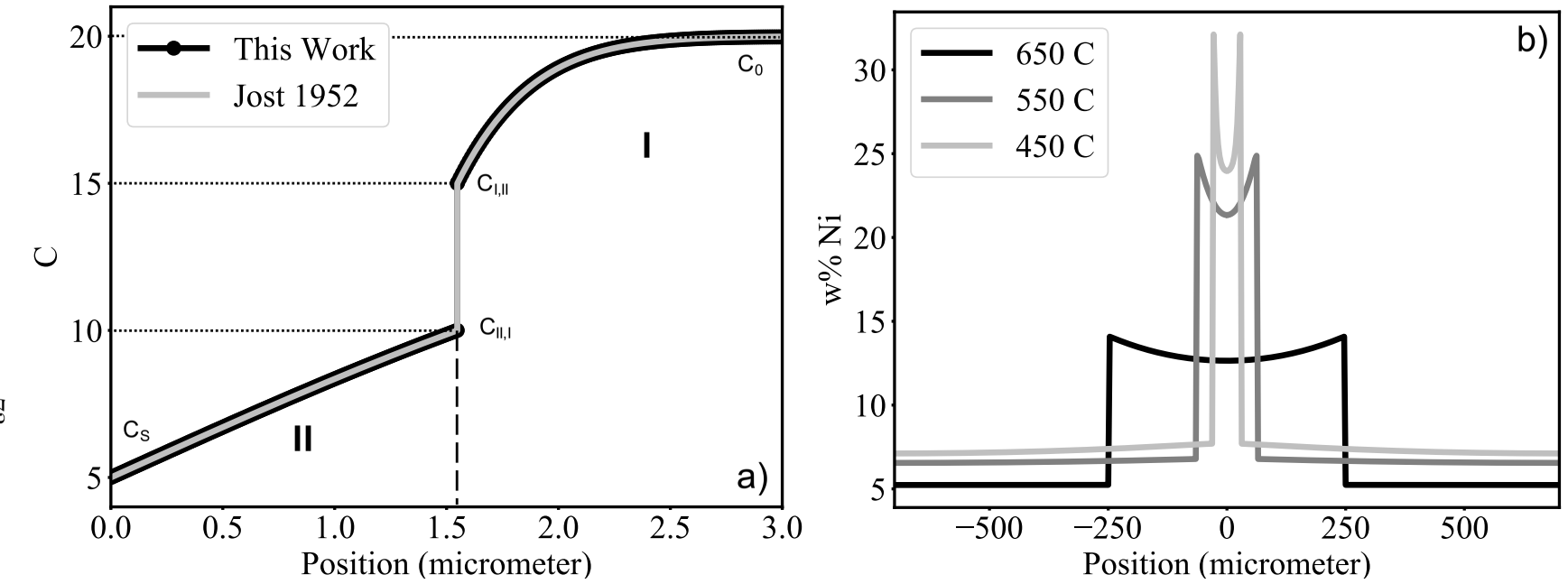

Figure 5.1: a) Illustration of our numerical model compared to an unphysical situation numerically solved in Jost (1952). The above curves agree nearly identically with residuals no larger than 10^{-4}. A detailed outline of the problem can be found in Dauphas (2007). b) The Widmanstätten pattern curves at various temperatures during growth. The hottest temperature being early in its growth and the lower, later. This is a technical test comparing our model to that of Dauphas (2007) and Hopfe and Goldstein (2001). We find results for the central Ni concentration and taenite band half-width that are in good agreement with both studies.

cooling rate of 50 C/Myr, we calculated the growth of the Widmanstätten pattern over time. Figure 5.1b shows the result of our model at three temperatures during the cooling of the sample and illustrates the evolution outlined above and shown schematically in Figure 4.2. Hopfe and Goldstein (2001) found a final taenite half-width of 31.9 μm and a central Ni concentration of 23.96 wt% while Dauphas (2007) reported values of 27.2 μm and 23.93 wt% respectively. Our final profile has an interface position of 26.93 μm and a central Ni content of 24.05% which is within the $\sim$5 μm error allowed in Dauphas (2007) due to the initial kamacite seed size.

In addition, we applied our model to reproduce the Wood Diagram shown in Yang et al. (2008) in their investigation of the origin of the IVA iron. We ran a suite of numerical models assuming the meteoritic composition of the IVA meteorite Gibeon with several constant cooling rates while varying the initial impingement length. This produces the aforementioned iso-cooling rate curves over which the meteoritic data is plotted (Figure 5.2). From this Yang et al. (2008) estimated a cooling rate of 1500 C/Myr (with a range from 800 - 2200 C/Myr) which we find good agreement with, particularly given the factor of 2.5 uncertainties estimated for such inferences (Wood, 1967; Taylor et al., 1987; Williams et al., 2000; Harrison and Grimm, 2010). In total, these agreements give confidence in our numerical approach.

5.3 The Effects of Variable Cooling Rates

Applications of the type described in Chapter 4 to meteorite analyses assume a constant cooling rate throughout the time of Widmanstätten pattern formation. However, neither the models nor meteoritic evidence restricts the cooling rate of an iron meteorite parent body to be constant throughout this time. While a differentiated planetesimal with an insulating mantle will produce a thermal history that has a near constant cooling rate (Haack et al., 1990), as discussed earlier, events such as impacts can drastically disrupt and alter the cooling history of the parent body (Chapter 3). Impacts would have been frequent over the tens to hundreds of million years over which meteorite parent bodies cooled. Therefore, it is

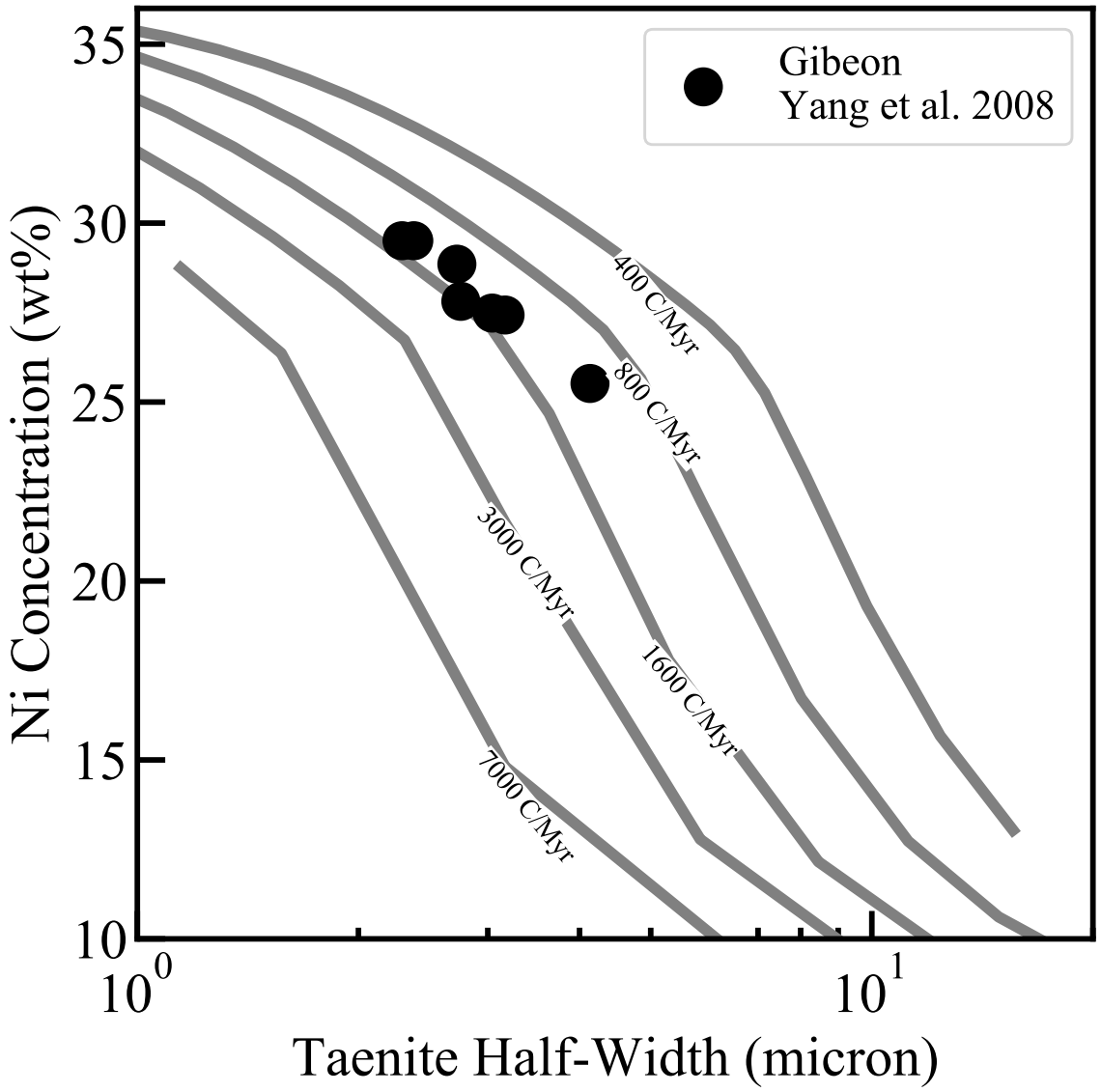

Figure 5.2: Example of our Widmanstätten pattern growth model used to create a Wood Diagram to estimate the cooling rate of the IVA Gibeon meteorite as done in Yang et al. (2008). The gray curves are the iso-cooling-rate curves as calculated with our model and the black points are individual measurements from Gibeon as reported in Yang et al. (2008). We find good agreement with their inferred cooling rate.

important to understand what effects this may have on the formation of the Widmanstätten pattern.

5.3.1 Stripped Mantle

The extent to which an impact alters a parent body will depend sensitively on the impact velocity and geometry of the impact. These parameters play critical roles in determining the post-impact structure of the impactor (defined as the smaller planetesimal) and target (the larger body) (Leinhardt and Stewart, 2012). Hit-and-run impacts are grazing, oblique impacts near the mutual escape velocity of the two bodies. Generally, the target body is unaffected during these events, but the impactor is either destroyed or strung out into smaller, planetesimal-sized fragments (Asphaug et al., 2006; Asphaug, 2010). These smaller remnants can vary in size and composition; if they originated from a differentiated body, it is possible that some will even represent bodies that are largely composed of iron, with little to no silicate layer surrounding them. Such remnants can be of particular interest due to their stark contrast to the expected structure of a differentiated body. While hit-and-run impacts may not be on the only method by which the mantle can be stripped away (i.e. sequence of smaller impacts removing the mantle), it may be the most common process.

Yang et al. (2008) modeled the 1D thermal evolution of plausible stripped cores as means of understanding the origin of the IVA irons. They determined that a 150 km radius iron body with less than 1 km of silicate mantle could produce the range of cooling rates inferred for the IVAs, provided the impact occurred early when the planetesimal was still largely molten. This structure would have led to samples with the highest cooling rates originating from the outer regions of the body, while the inner regions cooled more slowly. As a result, this would lead to in outward-in crystallization of the core as long as the solidified iron does not sink to the center of the stripped body. The melt in the interior would become enriched in Ni as pure Fe crystallized in the outer regions first with increasing amounts of Ni as the crystallization reaches the center of the core. The bulk Ni concentration would, therefore, be

inversely correlated with cooling rate. As discussed by Yang et al. (2008), this crystallization scheme is consistent with the Ni concentrations observed within the meteorites.

In Figure 5.3, we follow Yang et al. (2008) and show the thermal history of two possible iron-rich bodies that formed from a hit-and-run impact. The bodies are 150 km in radius and begin at a temperature of 1750 K. The two bodies differ in that one is assumed to be pure iron (left-hand side), while the other contains a thin, 0.6 km thick, insulating silicate layer on its surface (right-hand side). The thermal evolution of each body is calculated using the 1D model in Chapter 3, adopting model parameters from Yang et al. (2008). The bottom row of Figure 5.3 shows the temperature as a function of time at particular depths within the two bodies. While the center of each cools at similar rates in the two cases ($\sim$100 C/Myr), the outer most regions of the body, at 60 km depth or less, have very different thermal histories. With no silicate layer, early cooling rates can exceed 10^4 C/Myr at depths of less than 7.5 km in the bare iron body. The thin silicate layer provides slight insulation in the other, yielding maximum cooling rates in excess of 1000 C/Myr at depths less than 15 km. In both cases, there is an order of magnitude or more cooling rate gradient between the surface of the body and the center, consistent with the range of cooling rates observed in IVA meteorites.

If the IVAs are derived from such stripped iron bodies as proposed by Yang et al. (2008), then a natural consequence is that the cooling rates would not be constant throughout the formation of the Widmanstätten pattern. The top row of Figure 5.3 shows the cooling rate of the iron as a function of temperature at various depths in the 150 km radius bodies. The shaded region denotes the approximate temperature range of Widmanstätten pattern formation ($\sim$700 – 450 C). The cooling rate change at a single depth can be nearly a factor of two over this temperature range; for example, in the pure iron case at a depth of 4.5 km sees cooling rates of about 5600 C/Myr when the Widmanstätten pattern begins to form, before slowing to $\sim$2300 C/Myr when the metallographic closure temperature is reached (Figure 5.3a).

It is the detailed cooling history through this temperature range that controls Ni diffusion

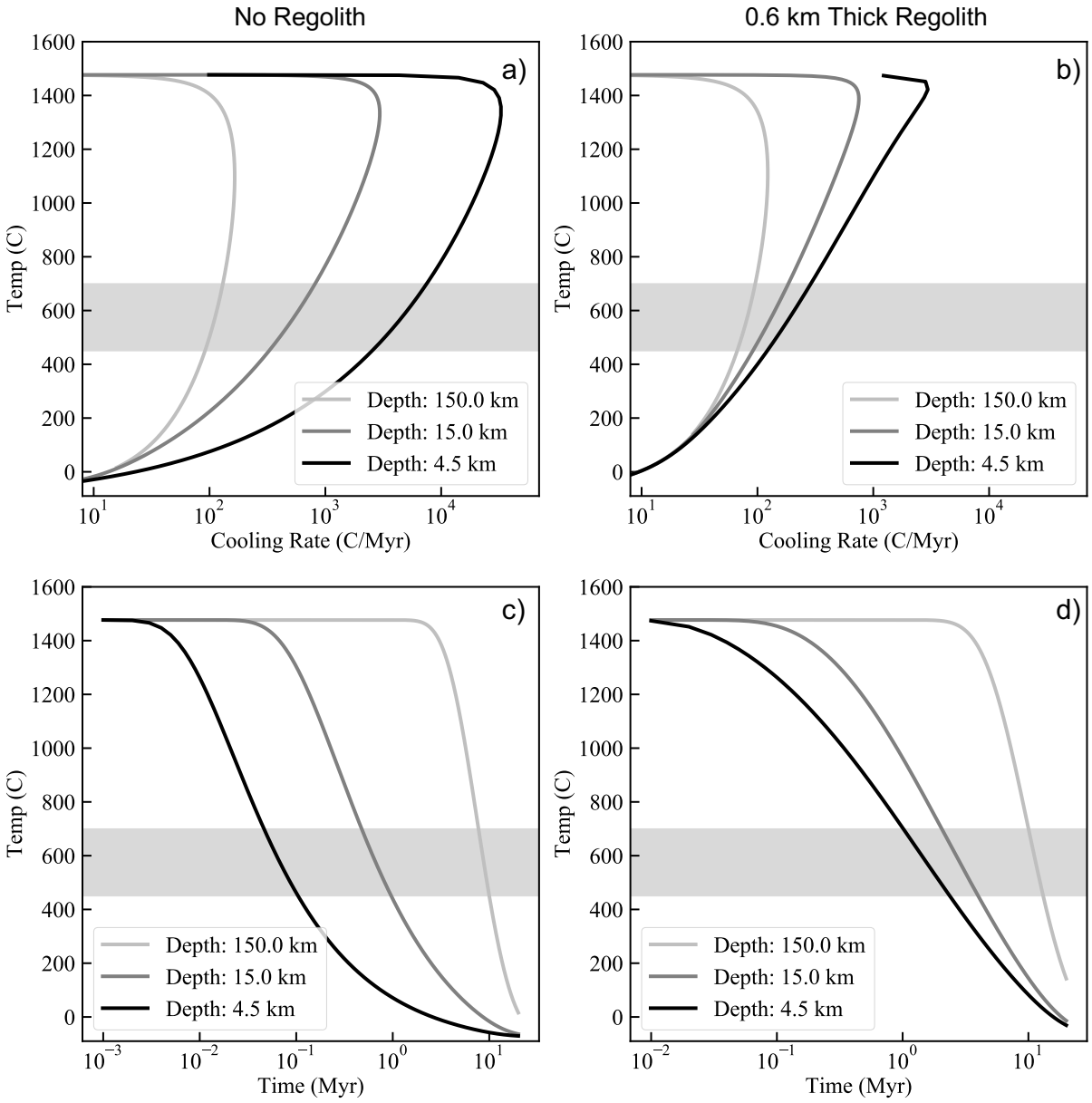

Figure 5.3: Looking at mantle stripped bodies, one with no regolith (left-hand side) and another with 0.6 km (right-hand side), we can see how the cooling rate changes as a function of depth in each body at two distinct temperatures. The cooling rates recorded at 700 C denote the beginning of Widmanstätten pattern formation and 450 C marks the end. The temperature as a function of cooling rate and time are also illustrated for both bodies. As is expected, the increased insulation due to the regolith slows the cooling. However, there can still be considerable variation in cooling rates throughout the lifetimes of the bodies.

and grain growth within the iron. As such, we used the calculated thermal evolution profiles as inputs into our Widmanstätten pattern formation model to understand how the variations in cooling rate impacted the properties of the taenite and kamacite. We carried out a suite of simulations, varying the initial impingement lengths between the kamacite nucleation sites to determine how the Widmanstätten pattern would form under these cooling histories. The suite of simulations combined to yield the Wood Diagram shown in Figure 5.4. In these calculations we use the properties of the Gibeon meteorite (as in Figure 5.2) with the bulk Ni concentration set to 8.04 wt%, P concentration to 0.04 wt%, and a kamacite nucleation temperature of 640 C. Each model was stopped at 450 C, which is the metallographic closure temperature. We plot the constant cooling rates of 400, 800, 1200, 1600, 3000, and 7000 C/Myr for reference, along with the curves predicted if one follows the thermal profiles of the stripped core at depths of 4.5, 7.5, and 15 km. Each of these depths follow the thermal histories as described in Figure 5.3 for the stripped iron core with no remaining regolith. Nearest to the surface, the 4.5 km depth case enters the Widmanstätten pattern formation region cooling at about 5615 C/Myr and slows to 2375 C/Myr at the closure temperature. For a depth of 7.5 km the cooling rate decreases from about 2175 to 950 C/Myr, while at 15 km depth, the cooling rate changes from about 650 to 325 C/Myr.

We see that for narrow half-widths the curve from a stripped body align with slower, constant cooling rates, close to, but slightly faster than those experienced near the metallographic closure temperatures of 450 C for each depth. At larger half-widths, the curves are closer to the more rapid cooling rates seen when kamacite first nucleates, though align better with slightly slower values.

This behavior can be explained when thinking about the timescales of the various processes at work. A sample that cools quickly will lock in a low initial central Ni value (via the phase diagram; Figure 4.1) and large half-width (relative to the initial impingement length), as there would be little time for diffusion to redistribute the Ni or for the phase boundary between the taenite and kamacite to migrate. Even if the cooling rate slows over time, these

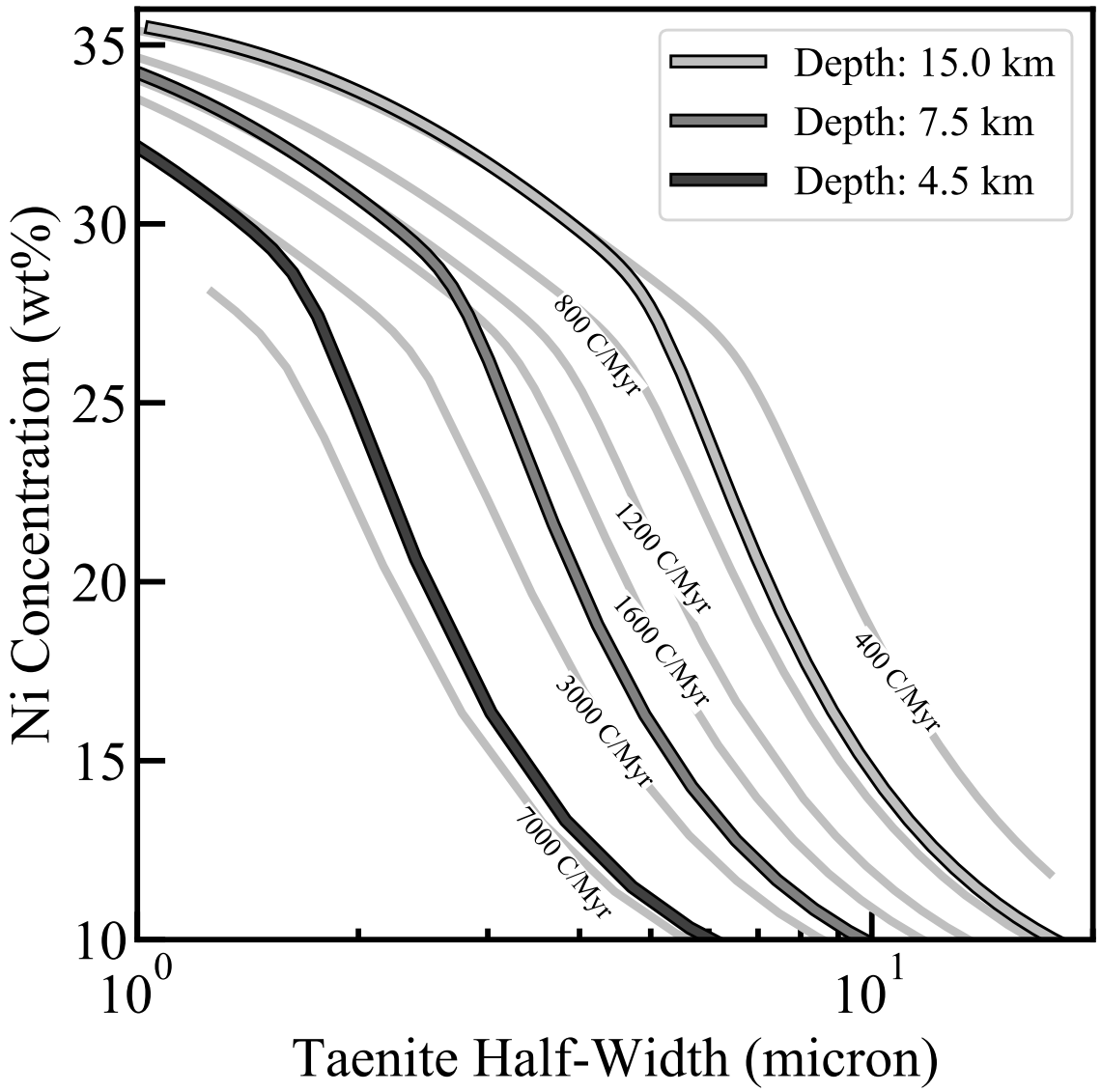

Figure 5.4: Comparison of the iso-cooling-rate curves, in gray, and the stripped mantle cases at specified depths in a 150 km radius iron body.

processes would be very slow as lower temperatures would have been reached, preventing much evolution than what was recorded by the initial rapid cooling. This effect is less severe for narrow taenite bands (small initial impingement lengths); while fast cooling rate still sets the initial characteristics, the timescale for diffusion ($t_{Diff} \sim \frac{(\Delta x)^2}{D}$) can still be small or comparable to the cooling time even at the lower temperatures, allowing for the processes to leave measurable effects at the slower cooling rates. In these cases, the final taenite bands will then more record those cooling rates nearest to the end of formation. At intermediate taenite half-widths, the curve transitions between the constant cooling rate curves that bound it.

Therefore, for a given depth, the Widmanstätten pattern will capture the characteristics of the latest cooling rates during its formation when the impingement lengths are narrow and the faster cooling rates when the impingement lengths are larger. Returning to the half-width and Ni-concentrations reported for Gibeon (Figure 5.2), we find that the data cluster at taenite half-widths of 4 μm or smaller. Yang et al. (2008) inferred that this meteorite originated in an iron-rich body with a minimal silicate layer, and assuming constant cooling, estimated a cooling rate somewhere between 750 - 3000 C/Myr, pointing to an origin within 15 km depth from the parent body. Our results, accounting for the changing cooling rates during Widmanstätten pattern formation, is still consistent with this interpretation, as the thermal profiles of depths in this region would lie near those of the Gibeon meteorite. The data largely come from small taenite half-widths (<4 μm), meaning the ∼1500 C/Myr average reported by Yang et al. (2008) corresponds to the cooling rates that occurred as the metallographic closure temperature was reached. The largest taenite half-width point in the Gibeon data set provided by Yang et al. (2008), at 4 μm and Ni-concentration of ∼25 wt%, if accurate, suggests that the meteorite originated somewhere between 7 and 15 km depth, to ensure the slow cooling rates at the metallographic closure temperature (matched by the data at 3 μm and smaller) while not recording significantly faster cooling rates at the larger half width of 4 μm.

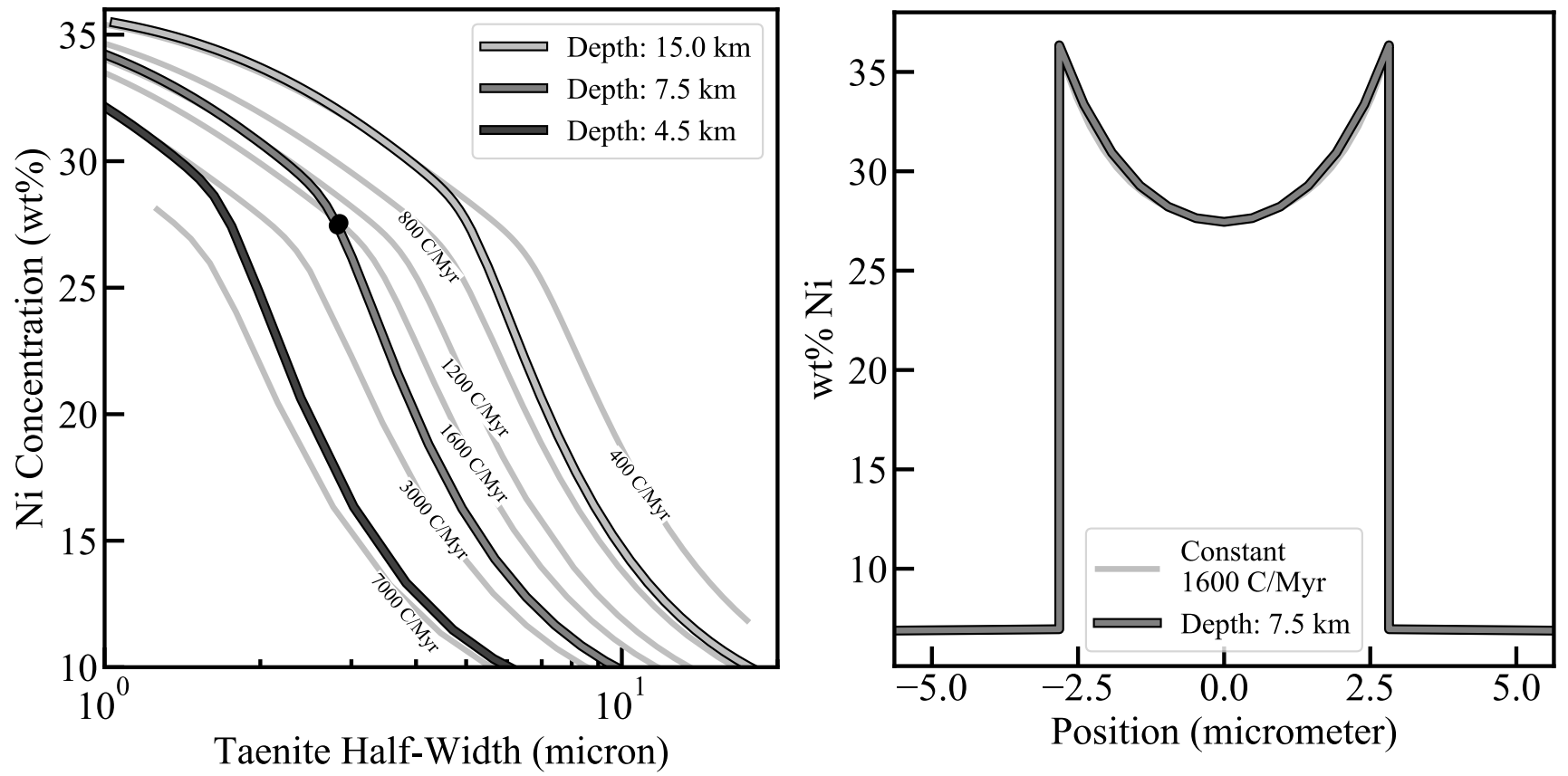

Figure 5.5: We can look at the profiles themselves to get a better idea of the variations caused by the mantle stripping event. The black dots (overlapping) denote the location where the 7.5 km deep curve intersects with the constant 1600 C/Myr curve. We can plot both of these on top of each other and compare their full Ni concentration. When looking at the curve fits, they do not showcase any considerable difference.

In addition to the Wood diagram, cooling rates can be inferred by fitting Ni concentration profiles across mineral bands with model predictions. We also investigated if any differences would be found in profiles for impacted versus constant cooling histories. Figure 5.5 examines this at one particular point at the intersection of constant and impacted cooling profiles in the Wood diagram, meaning regions where the predicted taenite half-width and Ni concentration are identical in the two cooling histories. The point considered here is denoted by the black points on the Wood diagram on the left-hand side of Figure 5.5. Here the cooling history of the 7.5 km deep region of the stripped mantle core intersects the 1600 C/Myr iso-cooling-rate curve at a taenite half width of about 2.8 μm and central Ni concentration of 28 wt%. In these cases, the stripped mantle case began with an impingement length of 48 μm and the constant cooling rate case with an impingement length of 46 μm. The panel on the right compares the overall shape of the profiles in the two cases, demonstrating no significant difference in the shape of the profiles that are predicted. We similarly find no discernible difference between any set of two intersecting curves, be it in the "transition" region, as illustrated in Figure 5.5, or when the curves are well aligned.

5.3.2 High Energy, Small Body Impacts

Another set of impacts that would have affected the cooling rates of iron meteorites in the early Solar System were collisions between small bodies at high velocities. While details vary with orbital evolution of the giant planets, a 100 km radius planetesimal in the asteroid belt would have a $\sim$10% chance of experiencing at least one impact between itself and an impactor 20% of its size and a $\sim$20% chance of being hit by an impactor 10% its size in the first 100 Myr (Davison et al., 2013). The mean impact velocity onto a 100 km radius body during this time could be upwards of 10 km s^{-1}, with a long tail towards higher velocities (see also Johnson et al. (2016)). Due to the generally smaller mass of the impactors, these events would generally be subcatastrophic but would have greatly increased the cooling rates of the hot interiors of the target, including the iron in differentiated bodies, producing large

cooling rate variation.

I demonstrated in Chapter 3 that the acceleration in cooling rate will vary significantly with the timing of the impact, size of and velocity of the impactor, and the size of the planetesimal, as well as the location within the target (Lyons et al., 2019). The maximum effect occurs when the impact significantly erodes or displaces the insulating mantle or brings hot iron into contact with already cooled mantle or crust. Rather than consider all cases, we parameterize the thermal histories expected from plausible impacts in order to show their effects on the Widmanstätten pattern. Such cooling profiles may only represent a portion of the iron in the planetesimal, as variation in such events is expected (Figure 3.7). An example is shown in Figure 5.6, where we consider a sample cooling at relatively constant rate of ∼9 C/Myr (expected for a 100 km radius planetesimal with a 44 km radius core) that has its cooling rate accelerated due to an impact at various times during the formation of the Widmanstätten pattern. We assume that the cooling rate jumps to 500 C/Myr immediately after the impact and slows to 100 C/Myr at the time when the Widmanstätten pattern formation ends. Such a jump occurred in a head-on impact involving a 100 km radius target, 20 km radius impactor, and an impact velocity of 6 km s^{-1} after ∼100 Myr of cooling. While the exact thermal history will vary across different impact scenarios and within the parent body itself, we use these numbers for each case for ease comparisons among them. The highlighted curves are thermal histories of impacts that occurred at 25, 50, and 75% of the way through the temperature range Widmanstätten pattern formation (592.5, 545, and 497.5 C respectively) assuming the same composition as the Gibeon IVA meteorite as a base.

As we had done with the stripped mantle cases, these thermal histories were used as inputs into our Widmanstätten pattern model, varying the impingement lengths in order to determine the final taenite half-width and central Ni concentrations that would be found in iron samples. The curves associated with each impact are plotted in the Wood Diagram in Figure 5.7. The shade of each curve shown corresponds to those in Figure 5.6, while the

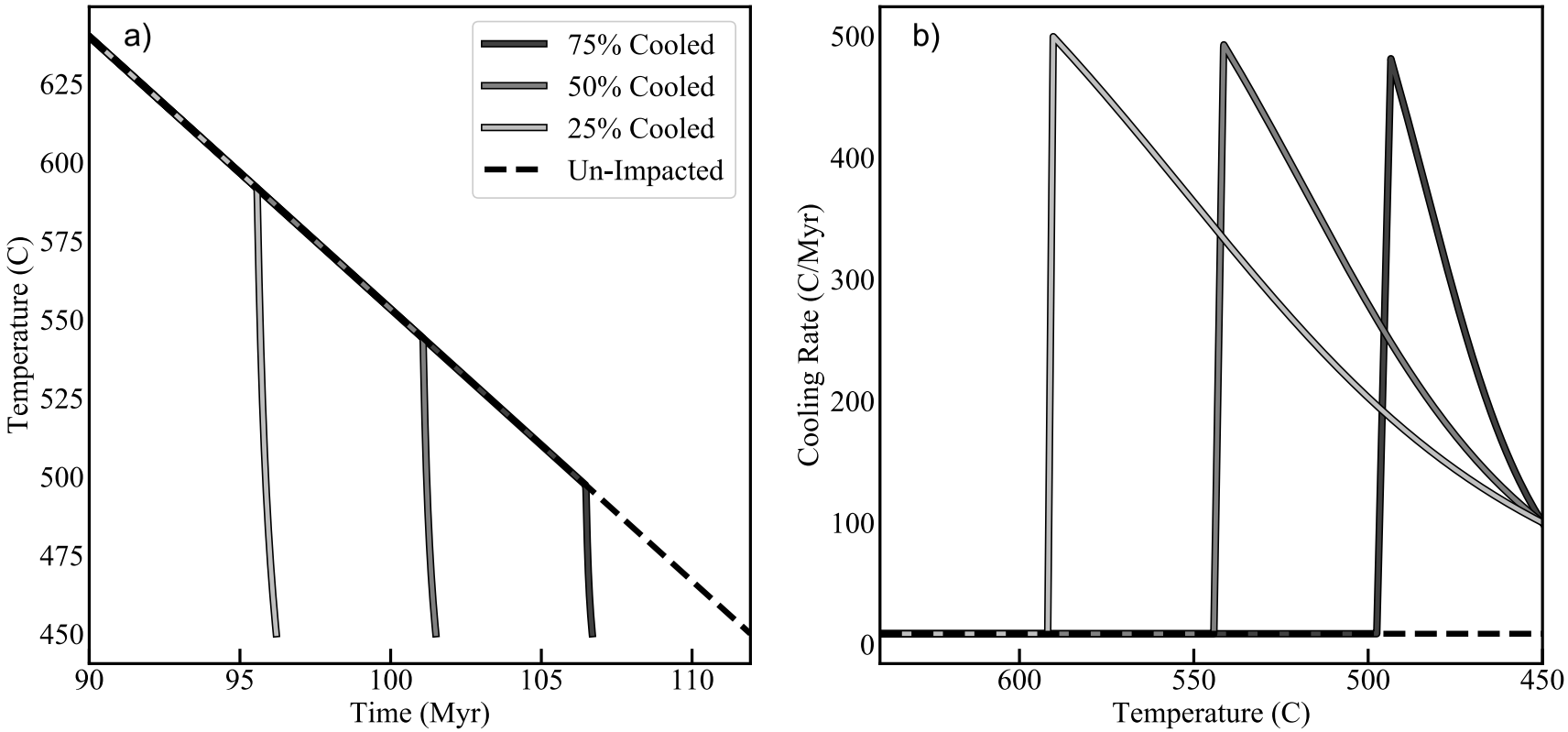

Figure 5.6: Three similar impacts to that of the iSALE simulation are shown here. Each impact occurred at a different period of Widmanstätten pattern formation. The black dashed line denotes the unimpacted case. Each impacted case breaks from this constant cooling rate case when the core is partly through the temperature range over which the Widmanstätten pattern forms. Particularly, 25, 50, and 75% cooled. (a) The temperature sharply decreases then the impact occurs. (b) The cooling rate varies greatly during the subsequent cooling of the impacted cases.

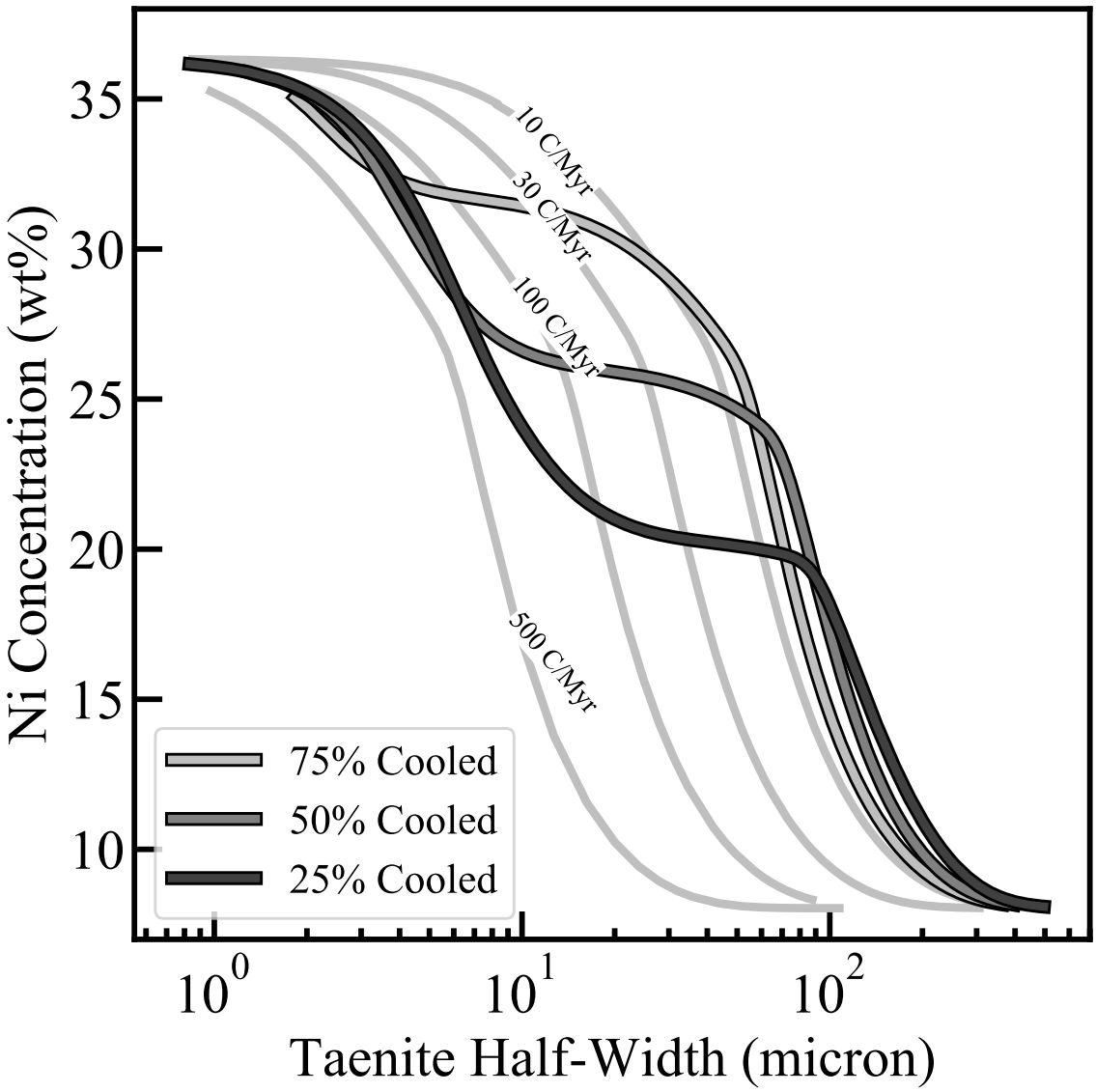

Figure 5.7: The Wood Diagram comparing the iso-cooling-rates in gray to the bold impacted curves. Each impacted curve denotes when an impact occurred during the Widmanstätten pattern formation: 25, 50, 75% through the temperature range of formation.

light grey lines represent iso-cooling rate curves at constant cooling rates. As seen in the stripped mantle cases shown in Figure 5.4, the impacted Widmanstätten curves diverge from those of the constant cooling rate cases, following one such curve at small taenite half-widths and others at large values. However, here the curves have the opposite structure from the stripped mantle cases. When the impingement length is large, leading to large taenite half-widths (the lower right of a Wood Diagram), the impacted curves closely match the constant cooling rate curve for the unimpacted body. At short impingement lengths, and thus narrow half-widths, the impacted curves have properties consistent with rapid cooling.

Again, this can be explained when thinking of the timescales involved. At large impingement lengths, the effects of the "slow cooling" are locked into the pattern when the impact occurs; the rapid cooling will slow diffusion and grain growth sufficiently (by dropping to lower temperatures) that they will be unaffected. This essentially locks in the same Ni-concentration and half-width relationship that occurred at the slow cooling rates. Likewise, the rapid cooling after the impact prevents the continued diffusion and grain growth that is expected for the small impingement lengths. However, at these small distances, the diffusion timescale would be much less, meaning changes in Ni-concentration would still have occurred during the slow cooling that the unimpacted sample would have experienced. By rapidly cooling the sample by impact, this prevents the diffusion from supplying the center of the taenite grain with more Ni as the kamacite grows. Thus, lower Ni-concentrations are locked in for a given half-width, as expected for rapidly cooled samples.

The transition between these two extremes for a given cooling profile crosses a variety of constant cooling rate curves. The point at which the impacted curves diverge from the unimpacted, constant cooling is set by what fraction of the Widmanstätten pattern has formed at the time the impact occurred. This is similarly due to the same diffusivity constraints discussed above. When the impact occurs late in the formation of the Widmanstätten pattern there is little time left for the Widmanstätten pattern to be perturbed, meaning that earlier impacts will be more easily recognized in meteorites.

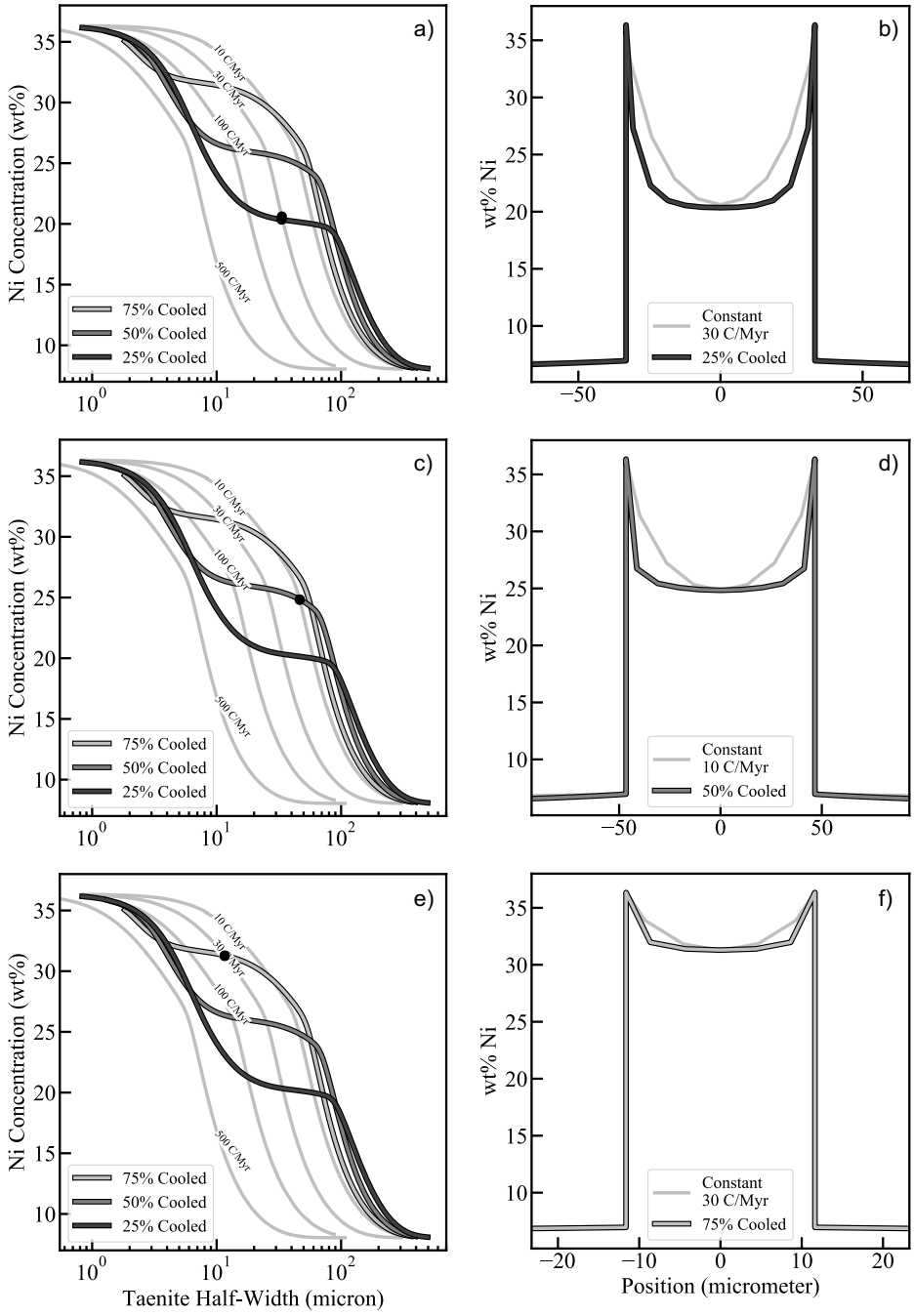

Figure 5.8: As was done in the stripped mantle case, we can look at the individual Ni profiles to see any variation that may occur due to the impact onto the planetesimal. The black points (left-hand side) denote the intersection of the constant cooling rate curve at 10 C/Myr and when an impact occurs 50% through Widmanstätten pattern formation. Zooming in on the taenite bands of each of these models (right-hand side) we see a considerably shallower taenite profile for the impacted case compared to the constant cooling rate

Again, the Wood Diagram is just one method for inferring the cooling rates of a meteorite group. As we did with the stripped parent body case, also examined the shapes of the Ni concentration profiles within the taenite. These profiles are shown along constant cooling rate profiles in the panels on the right-hand side of Figure 5.8. These comparisons are done for points where the impacted cooling profile of the Wood Diagram intersects that of an iso-cooling-rate curve. The black points have, by definition, identical central Ni concentrations and taenite half-widths, but we see in the right-hand column that the overall shapes of the profiles differ significantly from one another.

For example, the center panels (Figure 5.8c,d) compare the Ni-concentration profiles expected when an impact occurs when a sample has cooled 50% through the Widmanstätten pattern formation temperature range and a constant cooling rate case of 10 C/Myr on the Wood diagram. While the half-width and Ni-concentration of the center are necessarily identical in these two cases, the Ni-profile formed within the taenite for the impacted case is much shallower. This, again, shows the effect of the rapid cooling and resulting slow diffusion of Ni within the taenite. During slow cooling, Ni migrates from the taenite-kamacite boundary to the center of the taenite; however, here we see that process no longer was efficient, keeping the Ni low through much of the taenite, with very steep distributions near the grain boundary. A 5 wt% difference between the two Ni profiles, with the slow, constant cooling having higher values than the impacted case. Such differences would be large enough to be measured and a means of identifying that a sample was exposed to rapid cooling acceleration. Further, the required initial impingement length of the runs differed in these two cases. In this case, the 10 C/Myr constant cooling rate profile had an impingement length of 664 μm while the impacted profile was only 516 μm. Although it may be difficult to precisely measure impingement lengths in all cases, such differences can also be indicative of an impact event, with the size of kamacite grains varying accordingly.

The type of differences discussed above occurred in all cases explored in this "transition" region of the Wood diagram, regardless of when the impact occurred. We do not see similar

discernible differences in taenite Ni profiles for the constant and impacted case outside of the "transition" region. Thus, the effects of the impacts will only be identified if taenite has grown large enough; in the example used in Figure 5.8, this would require taenite half-widths >10 μm. If only smaller bands are present, then a more rapid cooling rate for a sample would be inferred than it actually experienced throughout the period of Widmanstätten pattern formation.

5.4 Discussion & Conclusions

Meteorites and asteroids are the remnants of planet formation and can provide direct insight into the initial population of planetesimals. Such objects, unfortunately, were not isolated for eons only to emerge unscathed upon our analysis but experienced a variety of events and perturbations that must be accounted for in order to properly interpret their histories. Understanding how signatures impacts involving these bodies may be hidden in the meteoritic record via the Widmanstätten pattern provides a means to infer the collisional history of their parent bodies, and can give insight into dynamics of the early Solar System, helping to answer questions surrounding how planets form.

Here we have shown the effects of nonlinear cooling on the development of the Widmanstätten pattern in iron meteorites. When such cooling occurs, when compared to constant cooling rates, we would find:

1. The taenite half-width and central Ni-content relationships (the Wood diagram) for nonlinear cooling approximately line-up or approach those of the constant cooling rate that a sample experienced when the Widmanstätten pattern began to form at large values of the resulting half-width.

2. The taenite half-width and central Ni-content relationships for nonlinear cooling approximately line-up or approach those of the constant cooling rate that a sample experienced at the metallographic closure temperature at small values of the half-width.

3. There is a transition between these two extremes where a change in cooling rates may be identified.

Whether the signatures of cooling rate changes can be confidently identified within a given meteorite sample will depend on the nature of the changes and the opportunities that the meteorite provides. Typical uncertainties in a given meteorite cooling rate are estimated to be of order a factor of 2; for example, while Yang et al. (2008) estimated a cooling rate of ∼1500 C/Myr for Gibeon, they estimated that uncertainties were such that the cooling rate ranged from 750 - 3000 C/Myr. A change in cooling rate thus would likely only be recognized or inferred if the cooling rates were comparable to this range (a factor of ∼4 change). While we saw cooling rate variations in the modeling of the exposed iron core in Figure 5.3, we rarely see such large variations during the formation of the Widmanstätten pattern. Thus, identifying these signatures may be limited to those cases where very large changes in cooling rates occur (for example in smaller pure iron bodies in the case of hit-and-run collisions).

The signal and changes in cooling rates identified in our small impact scenarios, however, do yield cooling rate increases that are orders of magnitude larger than what would otherwise occur. As a result, the likelihood of being able to identify these signatures in a given sample is greater. However, this requires finding taenite bands of the proper half-width. As shown in Figure 5.7, at very large half-widths, the impacted curves follow the constant cooling rate curves of the unimpacted body. At very short half-widths, the impacted curves record the very rapid cooling that the sample experienced at the end of Widmanstätten pattern formation, looking like constant cooling rates were experienced. However, at intermediate half-widths, here 10 - 100 μm, the impacted curves clearly diverge from the constant cooling rate ones. If half-widths of these sizes are identified and deviate from the constant cooling rates estimated when examining just the small half-widths, then this could serve as a signature of an impact. Evidence would be strengthened upon examination of individual taenite bands, as the Ni-diffusion profile should be relatively flat in the impacted cases in this region as compared to the predictions for constant cooling rate profiles.

An important corollary to this is that if only small half-widths, for example those <10 μm in Figure 5.7, are examined in a sample, they may be incorrectly interpreted as recording constant, rapid cooling. Again, despite the very slow cooling that the various samples in Figure 5.7 experienced at the beginning of Widmanstätten pattern formation, but the accelerated cooling after the impact prevented Ni diffusion from continuing to alter the compositions of the taenite band, freezing in a different half-width/central Ni-concentration relation than if that slower cooling had persisted. Such a sample may be thought to originate in a small parent body (Haack et al., 1990) or the center of a body formed in a hit-and-run impact such as that shown in Figure 5.4. In reality, the body may instead have been a large, $\sim$100 km, differentiated planetesimal that simply experienced a subcatastrophic impact late in its history.

In the literature, for individual samples, taenite half-widths are observed to range from 1 μm to nearly 100 μm (Wood, 1964; Rasmussen, 1981, 1989; Rasmussen et al., 1995; Haack et al., 1996; Yang and Goldstein, 2006; Yang et al., 2008, 2010b). There are no reported half-widths greater than 100 μm. The "transition" regions as well as the upper left-hand side of Figures 5.4 and 5.7 would likely be observable in the meteoritic record while the largest half-widths would have no measurable relevance. In each case, the evidence of an impact could be observable as long as it spans the 10 – 100 μm region. We can look to meteorite groups for which impacts are thought to play a role in their formation such as the IAB, IVA, IIIAB, and pallasites to verify that samples could record their hypothesized impacts. IVA, IIIAB, and pallasite meteorites Bushman Land (Yang et al., 2008), Haig (Yang and Goldstein, 2006), and Giroux (Yang et al., 2010b) cluster very closely at half widths <10 μm. On the other hand, IAB, IVA, and IIIAB meteorites such as Toluca (Rasmussen, 1989), Duchesne (Yang et al., 2008), and Drum Mountains (Yang and Goldstein, 2006) exhibit taenite half widths that span possible "transition" regions making themselves good candidates to identify collisions on their parent bodies.

For these same meteorite groups, the absence of any traces of an impact with in their

Widmanstätten patterns does not explicitly rule out that an impact (or impacts) took place. An impact could have occurred early in the thermal history of the parent body mixing up iron and silicate (in the case of the IABs) while subsequently cooling very similarly to an unimpacted planetesimal, and as such would not perturb the growth of the Widmanstätten pattern. There may also not have been any change in cooling rates during impacts during Widmanstätten pattern growth as was the case for a large mass fraction of the core explored in Chapter 3. These perturbations to the Ni profiles and the Wood diagrams as a result of changes to a sample's cooling rates are a valuable tool to further understanding the histories of meteorite parent bodies and planetesimals in the early Solar System.

CHAPTER 6

CONCLUSIONS & FUTURE WORK

6.1 The Role of Impacts

Meteorites provide a record of the processes that affected planetesimals, including heating, differentiation, cooling, and impacts. These effects are often treated independently of one another, however, we know that they would have been concurrent and their effects need to be understood together. In this dissertation, it was shown that impacts in the early Solar System would have greatly accelerated the cooling of planetesimals by exposing materials in the heated interior. The cooling rates in these cases would not be constant, and the scrambled nature of these bodies would lead to variable cooling histories experienced by any metal that they contain. This is all in contrast to the expectations for unimpacted bodies. The rapid and nonuniform cooling rates of metal in impacted bodies would affect the growth of the Widmanstätten pattern, offering a means to identify the traces of impacts in the meteoritic record. Given the questions surrounding the formation of various iron meteorite groups (e.g., IAB, IIE, IVA, IVB), this offers a means to better understand their formation and gain insight into the general dynamic history of the Asteroid Belt.

Previous studies had shown that hit-and-run impacts between large bodies can lead to the the changes in thermal evolution described above. Such events would be rare, however. This dissertation work focused on the more common, high velocity impacts between planetesimals. It was found that the outcome of these impacts are highly dependent on the thermal state of the target body. Early in the cooling of a planetesimal ($\sim$1 - 20 Myr for a 100 km radius body), when the mantle and core are both consist of a significant amount of melt, an impact can lead to total disruption the target due to the weak nature of the material. If the target survives, however, the remnant quickly returns to something resembling the pre-impact structure of the target as metal will quickly settle to the center surrounded by a lower density, silicate mantle. As the planetesimal continues to cool, the mantle will begin to

solidify and strengthen, while the core will remain heated with significant portions of melt (∼50 - 70 Myr). During this period impacts can expose or uplift the core, removing the insulating silicate layer and increasing the rate of cooling in the iron by orders of magnitude. At later times (>70 Myr), continued cooling leads to further strengthening of the mantle and the solidifying of the core, making it more difficult to excavate and expose the deeply buried iron. Thus many impacts will not lead to any significant changes in the cooling rates recorded by the core. Exceptions may occur if the impacts occur right when the Widmanstätten pattern is being formed (∼90 - 110 Myr), when cooling rates are being recorded by the iron.

Given the ranges of cooling rates recorded by iron meteorite samples, it is important to understand whether signatures of these impacts may be recorded in iron meteorites. This work illustrated that the Widmanstätten pattern is highly sensitive to the cooling history during its formation. When cooling is nearly uniform, the M-shape Ni concentration curves in the taenite bands are formed as have been described and used in past studies and can be used to determine metallographic cooling rates of iron meteorites. However, when a sample cools at a variable rate, details of the Widmanstätten pattern change. For instance, looking at two profiles, one impacted and the other unimpacted, with the same taenite band width and central Ni concentration, the curvature of impacted profile can be much shallower. Further, the general relations between Ni-concentration and taenite band width as reflected on the Wood diagram, offer a means to distinguish cooling histories. Such a signatures can be observable if cooling rate changes were large enough during the Widmanstätten pattern's formation. While identification of these signatures alone are not guaranteed, the combination of these effects may offer a tool into identifying signs of impacts into differentiated bodies.

Impacts will not only affect the cooling rates of materials. These events may implant material from the impactor into the target. In the case of iron from the impactor, relatively low velocity impacts into large targets can lead to the formation of a metal reservoir that is distinct from the core. This metal would undergo separate thermal evolution but still be

affected by any magnetic dynamo produced interior to the body. Similarly, higher energy impacts could excavate portions of the core into the mantle creating metal reservoirs. Such scenarios have been outlined by Maurel et al. (2019) and Maurel et al. (2020) as playing a role in the formation of the IIE iron meteorite group.

In addition, impacts can have major effects in terms of mixing materials in different portions of a target. These events are dynamic, launching ejecta into space that will then be re-accumulated onto the remnant, and displacing various layers during excavation and relaxation of the crater that forms. This can lead to large-scale mixing of materials from different regions of the target, both silicate and metal. Given many meteorites show a variety of ways that metal and silicates have been intermixed, such as the IAB, IIE, pallasites, and mesosiderites (Benedix et al., 2000; Scott et al., 2001; Ruzicka and Hutson, 2010; Yang et al., 2010b; Wasson, 2016), the effects of this mixing should be explored in greater detail.

6.2 Future Work

6.2.1 Planetesimal Impact History in a Dynamic Early Solar System

While planetesimal impacts undoubtedly occurred in the early Solar System, it is unclear how common the different varieties of these events would be and how they would change over time. The frequency and types of impacts would depend on the dynamical conditions and events that occurred as the planets formed. A number of dynamical scenarios have been proposed to describe the formation of the Solar System, focusing on reproducing the properties of the planets and their orbits. However, with the framework for interpreting iron meteorites outlined in the previous chapters, we can begin to mine the meteorite record as a means of understanding the dynamical evolution within the asteroid belt, and what this means for the dynamic assembly of planets.

The most common focus for models of the accretion of the terrestrial planets is understanding the properties of the largest planets, Jupiter and Saturn. These giant planets exert

a significant gravitational influence on the planetesimals and planets interior to their orbits. These influences will lead to the planetesimals having their eccentricities and inclinations excited, leading to crossing orbits and increasing relative velocities. However, the level to which this occurs depends specifically on the orbits of these planets and the distribution of solid matter in the terrestrial planet zone.

As illustrated in Davison et al. (2013), whether Jupiter and Saturn start off on circular (CJS) or their modern day eccentricities (EJS) can change the probability and average impact velocity of collisions among planetesimals in the early Asteroid Belt. For the EJS case, the impact velocities increased sooner (first million years) than that of the CJS with velocities near 7 km s^{-1} in EJS compared to $\sim$3 km s^{-1} for CJS. This is due to Jupiter moving closer and further from the asteroids on its eccentric orbit, effectively "stirring" the bodies to a greater degree. There was also a higher collisional probabilities early for EJS than CJS in the first million years. However, only after 1 Myr, the collisional probability for the EJS case decreases as planetesimals are more rapidly removed via collisions and excitation while the collisional probability of the CJS case stays constant until nearly 10 Myr. In each case, the mean velocity of an impact increases to between 8 - 10 km s^{-1} after 100 Myr of evolution. Differences in the frequency, timing, and velocity of collisions between these two dynamical scenarios were documented using a Monte Carlo simulation based on the accretion simulations of O'Brien et al. (2006). It was found that for the CJS case a 100 km radius body had a 10% chance of being impacted by a 20 km radius impactor in the first 100 Myr. In contrast, the chance of such an impact occurring under EJS conditions was only 3%. The differences in expected velocities and timing of these collisions were also documented.

Given that the impact history of a planetesimal is highly sensitive to its dynamical conditions, it can be hypothesized that distinct impact probabilities would occur under other models of Solar System evolution, such as the Nice Model, Grand Tack, or pebble accretion. Each of these models predict a different dynamic evolution for the Asteroid Belt. The Nice Model proposed that Jupiter and Saturn formed with circular orbits (CJS) and then,

through resonant interactions spurred on by a large population of cometesimals in the outer Solar System, obtained their current eccentricities and inclinations. With the Nice Model, an increase in collisions would be expected following the instability of the outer gas giants, which had been thought to occur several hundred millions of years after CAIs coinciding with the Late Heavy Bombardment (Gomes et al., 2005; Morbidelli et al., 2005; Tsiganis et al., 2005; O'Brien et al., 2006). However, subsequent work found that the terrestrial planets do not remain dynamically cold during the instability and would have their eccentricities and inclinations pumped up to such a degree as to be scattered out of the Solar System (Brasser et al., 2009). In order to reconcile a potential instability with the formation of the inner planets, additional dynamical models have shown that the instability would need to occur in the first few 10s of Myr (Clement et al., 2018). These dynamics would also lead to gravitational stirring of bodies in the Asteroid Belt, leading to significant excitement and collisions between the bodies present there.

The Grand Tack model also predicts a spike in collisions in the Asteroid Belt as a result of Jupiter's migration. After the formation of Jupiter and Saturn, their interactions with the gaseous disk would cause them to drift inward, only to return to their modern day orbits after falling into resonance with each other (Morbidelli and Crida, 2007; Walsh et al., 2011). A rapid excitement of the Asteroid Belt would occur at this point, as bodies in the inner Solar System are stirred by the inward migration of the planets and bodies from the outer Solar System are implanted during the outward migration. All of this would occur early, shortly after the formation of Jupiter and while the gaseous disk is around. This migration scenerio was motivated by the low mass of Mars which required a dynamical scenario that could deplete the available mass from which it could form. Such a depletion of planetesimals left in Jupiter's wake would lower the number of collisions post-Grand Tack.

Pebble accretion has emerged as a favored theory for explaining many issues in planet formation such as rapid formation of giant planet cores, the formation of planetesimals via the streaming instability, and the small mass of Mars (Lambrechts and Johansen, 2012;

Levison et al., 2015). In this model the growth of planetesimals and planets in the terrestrial planet region would be limited once Jupiter is formed as the gas giant would interact with the nebular gas to impede the further inward drift of pebbles. Stopping the replenishment of pebbles from outside the Asteroid Belt, in which pebbles are still drifting inwards towards the Sun, greatly decreases the available mass in the region to form from. This would result in not only a low mass planet Mars, but a very low mass the Asteroid Belt. In this scenario there would be no spike in collisions as in the others, as the low number of bodies would imply infrequent collisions in comparison to all other models.

The dynamical evolution of planetesimals as a result of unique configurations of Jupiter and Saturn can be followed with N-body particle code and the intrinsic collision probability as a function of time can be calculated (O'Brien et al., 2006). The model parameters for simulating the Nice Model would begin with Jupiter and Saturn on circular orbits, with a dynamically cool collection of planetesimals. After a prescribed amount of time (likely 10 Myr), the orbits of Jupiter and Saturn would instantaneously update to their modern day orbits (EJS). Under the framework of the Grand Tack, modeling the dynamical evolution of the Asteroid Belt would begin immediately after Jupiter and Saturn have returned to their modern day orbits (EJS). The postmigration excitation of the Asteroid Belt could be prescribed by setting the eccentricities and inclinations of the inclinations of the planetesimals to high values, with values informed by the N-body simulations of the Grand Tack (Walsh et al., 2011). Pebble accretion does not describe a large dynamical event as the previous two models, and as such would not need a particular set of initial conditions to model. Pebble accretion predicts a small number of bodies and that low density would affect the final estimated number of collisions, not the intrinsic collision probability.

Meteorites pose a unique opportunity to probe the dynamics of the early Solar System but require continued work to bolster the connection between the impacts onto a few parent bodies and those throughout the entire Asteroid Belt. The effort described above would be a first step in evaluating how common the impacts needed to create measurable changes to a

meteorite's thermal history and Widmanstätten pattern would be under various dynamical conditions. That understanding would also be bidirectional, allowing for an assessment of various hypotheses regarding early Solar System dynamics. For example, we observed that impacts during the formation of the Widmanstätten pattern could leave behind a signature in the resulting Ni profiles. Assuming parent bodies $\geq$100 km, these impacts would need to not only be energetic enough to cause increases in cooling rates but would need to occur more than 100 Myr after initial formation. In the Grand Tack model, impacts would likely occur very early, but may rapidly decrease in frequency with time as the mass in the Asteroid Belt is depleted by dynamic effects. If signs of late impacts are observed in the meteoritic record, this may indicate that the Asteroid Belt remained populated for long periods of time or that later-stage dynamic effects, possibly related to the Nice Model instability, took place.

6.2.2 Survey and Database of Widmanstätten Patterns

Given the possible insights that can be gained into the early Solar System, continued documentation of meteorite properties and searches for signs of impacts are needed. As outlined in this dissertation, detailed comparisons between measured Ni profiles of Widmanstätten patterns and numerical models can be used to infer the thermal history of the bodies form which the sample originated. An impacted thermal history with variable cooling may be preserved in the Ni concentrations however, it is also possible these features will appear no different than would be expected for an unimpacted sample. The strength of such a tracer for impacts in the meteoritic record is in the large number of Widmanstätten patterns not only in individual samples but across entire meteorite groups. But there there has been no large scale survey of the variety of patterns across all meteorite groups. Measurements have been made in order to infer the cooling rates, however it is unclear from these studies how Widmanstätten patterns which did not matched up with constant cooling rates were used or interpreted in the data.

In order to search for the traces of impacts that would otherwise go unnoticed in the

meteoritic record, a large scale survey of the Widmanstätten pattern is needed. This survey can consist of both full Ni profile measurements that can be used for the curve matching tests outlined in Chapter 5 and the taenite half-width and central Ni concentration for use in the Wood diagram. Measurements made on Widmanstätten patterns should then be entered into a field wide data base which can be accessed by those wishing to explore them. A larger collection of measured taenite and kamacite bands can better inform not only the occurrence of impacts but can be coupled with hydrodynamic models described in Chapter 5 to constrain the impact parameters of said collisions.

In addition, the timing of the impacts are also vitally important for the recording of an impact in the Widmanstätten pattern as well as an evaluation of a particular dynamical scenario. Work that determines and collects the possible timing of impacts across various meteorite groups, as done in Schulz et al. (2012) for the IAB, winonaite, and IIE groups as well as in both Hunt et al. (2018) and Hunt and Schönbächler (2019) for the IAB, IIAB, IIAB, and IVA groups, will be critical to creating a timeline of events in the early Solar System. The synthesis of both of these aspects will help piece together the dynamical history of meteoritic parent bodies.

Following these steps will provide an important and useful framework for using meteorites toward developing a greater understanding of planet formation in the Solar System.

6.3 Conclusion

The Solar System was chaotic in its early history. The meteorites that have been central to this thesis experienced the full extent of that chaos, including large impacts. This thesis has illustrated the continued utility of meteorites toward gaining insights into this time period. Meteorites allow us to infer the sizes of planetesimals, extent of heating and differentiation, chemical evolution, and impact histories of planetary building blocks. The continued evaluation of these models is necessary to hone our understanding these processes. Impacts between planetesimals not only played a key role in the formation of meteorites but the

formation of the planets in the Solar System and ought to be the focus of meteoriticists and dynamicists alike. Through an interdisciplinary understanding of impacts, we can take further steps to answering, "How do planets form?"

REFERENCES

A. Amsden, H. Ruppel, and C. Hirt. Sale: A simplified ALE computer program for fluid flow at all speeds. *Los Alamos Natl. Lab., Los Alamos, NM*, 1980.

E. Asphaug. Similar-sized collisions and the diversity of planets. *Chemie der Erde-Geochemistry*, 70:199–219, 2010.

E. Asphaug, C. B. Agnor, and Q. Williams. Hit-and-run planetary collisions. *Nature*, 439: 155–160, 2006.

G. Benedix, T. McCoy, K. Keil, and S. Love. A petrologic study of the IAB iron meteorites: Constraints on the formation of the IAB-Winonaite parent body. *Meteoritics & Planetary Science*, 35:1127–1141, 2000.

G. K. Benedix, H. Haack, and T. McCoy. Iron and stony-iron meteorites. *In Meteorites and Cosmochemical Processes (Ed. A. M. Davis), Vol. 1 Treatise on Geochemistry, 2nd Ed. (Exec. Eds. H. D. Holland and K. K. Turekian), Elsevier, Oxford*, pages 267–285, 2014.

W. Benz, A. Cameron, and H. Melosh. The origin of the Moon and the single-impact hypothesis III. *Icarus*, 81:113–131, 1989.

T. Bowling, R. Lyons, F. Ciesla, T. Davison, and G. Collins. Mixing of iron and silicate during collisions on differentiated planetesimals. *Lunar and Planetary Science*, 48, #2323, 2017.

R. Brasser, A. Morbidelli, R. Gomes, K. Tsiganis, and H. F. Levison. Constructing the secular architecture of the solar system II: the terrestrial planets. *Astronomy & Astrophysics*, 507: 1053–1065, 2009.

A. Cassan, D. Kubas, J.-P. Beaulieu, M. Dominik, K. Horne, J. Greenhill, J. Wambsganss, J. Menzies, A. Williams, U. G. Jørgensen, et al. One or more bound planets per Milky Way star from microlensing observations. *Nature*, 481:167–169, 2012.

F. J. Ciesla, T. M. Davison, G. S. Collins, and D. P. O'Brien. Thermal consequences of impacts in the early Solar System. *Meteoritics & Planetary Science*, 48:2559–2576, 2013.

R. N. Clayton and T. K. Mayeda. Oxygen isotope studies of achondrites. *Geochimica et Cosmochimica Acta*, 60:1999–2017, 1996.

M. S. Clement, N. A. Kaib, S. N. Raymond, and K. J. Walsh. Mars' growth stunted by an early giant planet instability. *Icarus*, 311:340–356, 2018.

G. Collins, T. Davison, and F. Ciesla. The effects of planetesimal collisions. *Meteoritics & Planetary Science Supplement*, 74, #5024, 2011.

G. S. Collins, H. J. Melosh, and B. A. Ivanov. Modeling damage and deformation in impact simulations. *Meteoritics & Planetary Science*, 39:217–231, 2004.

J. Crank. *Free and moving boundary problems*. Oxford University Press, 1984.

N. Dauphas. Diffusion-driven kinetic isotope effect of Fe and Ni during formation of the Widmanstätten pattern. *Meteoritics & Planetary Science*, 42:1597–1613, 2007.

T. Davison, G. Collins, and F. Ciesla. Numerical modelling of heating in porous planetesimal collisions. *Icarus*, 208:468–481, 2010.

T. M. Davison, F. J. Ciesla, and G. S. Collins. Post-impact thermal evolution of porous planetesimals. *Geochimica et Cosmochimica Acta*, 95:252–269, 2012.

T. M. Davison, D. P. O'Brien, F. J. Ciesla, and G. S. Collins. The early impact histories of meteorite parent bodies. *Meteoritics & Planetary Science*, 48:1894–1918, 2013.

T. M. Davison, F. J. Ciesla, G. S. Collins, and D. Elbeshausen. The effect of impact obliquity on shock heating in planetesimal collisions. *Meteoritics & Planetary Science*, 49:2252–2265, 2014.

S. R. de Groot. Thermodynamics of irreversible processes. *The Journal of Physical Chemistry*, 55:1577–1578, 1951.

D. Elbeshausen and J. Melosh. A nonlinear and time-dependent visco-elasto-plastic rheology model for studying shock-physics phenomena. *The Journal of Chemical Physics (Submitted)*, 2018.

D. Elbeshausen and K. Wünnemann. iSALE-3D: A three-dimensional, multi-material, multi-rheology hydrocode and its applications to large-scale geodynamic processes. In *Proceedings of 11th Hypervelocity Impact Symposium (HVIS), Fraunhofer Verlag*, 2011.

A. Ghosh and H. Y. McSween. A thermal model for the differentiation of asteroid 4 Vesta, based on radiogenic heating. *Icarus*, 134:187–206, 1998.

A. Ghosh, S. Weidenschilling, H. McSween Jr, and A. Rubin. *Asteroidal heating and thermal stratification of the Asteroid Belt*. Meteorites and the early Solar System II. University of Arizona Press, Tuscon, Arizona, 2006.

E. Goldberg, A. Uchiyama, and H. Brown. The distribution of nickel, cobalt, gallium, palladium and gold in iron meteorites. *Geochimica et Cosmochimica Acta*, 2:1–25, 1951.

J. Goldstein, E. Scott, and N. Chabot. Iron meteorites: Crystallization, thermal history, parent bodies, and origin. *Geochemistry*, 69:293–325, 2009a.

J. Goldstein, J. Yang, P. Kotula, J. Michael, and E. Scott. Thermal histories of IVA iron meteorites from transmission electron microscopy of the cloudy zone microstructure. *Meteoritics & Planetary Science*, 44:343–358, 2009b.

J. I. Goldstein and R. E. Ogilvie. The growth of the Widmanstätten pattern in metallic meteorites. *Geochimica et Cosmochimica Acta*, 29:893–920, 1965.

J. I. Goldstein and J. M. Short. The iron meteorites, their thermal history and parent bodies. *Geochimica et Cosmochimica Acta*, 31:1733–1770, 1967.

R. Gomes, H. F. Levison, K. Tsiganis, and A. Morbidelli. Origin of the cataclysmic Late Heavy Bombardment period of the terrestrial planets. *Nature*, 435:466–469, 2005.

J. D. Gregory, R. G. Mayne, J. S. Boesenberg, M. Humayun, A. P. Silver, R. C. Greenwood, and I. A. Franchi. Choteau makes three: A characterization of the third member of the Vermillion subgroup. *Lunar and Planetary Science*, 47, #2393, 2016.

H. Haack, K. L. Rasmussen, and P. H. Warren. Effects of regolith/megaregolith insulation on the cooling histories of differentiated asteroids. *Journal of Geophysical Research: Solid Earth*, 95:5111–5124, 1990.

H. Haack, E. R. Scott, and K. L. Rasmussen. Thermal and shock history of mesosiderites and their large parent asteroid. *Geochimica et Cosmochimica Acta*, 60:2609–2619, 1996.

K. P. Harrison and R. E. Grimm. Thermal constraints on the early history of the H-chondrite parent body reconsidered. *Geochimica et Cosmochimica Acta*, 74:5410–5423, 2010.

P. J. Hevey and I. S. Sanders. A model for planetesimal meltdown by ^{26}Al and its implications for meteorite parent bodies. *Meteoritics & Planetary Science*, 41:95–106, 2006.

W. Hopfe and J. Goldstein. The metallographic cooling rate method revised: Application to iron meteorites and mesosiderites. *Meteoritics & Planetary Science*, 36:135–154, 2001.

K. Housen, L. Wilkening, C. Chapman, and R. Greenberg. *Regolith development and evolution on asteroids and the Moon*. University of Arizona Press, Tuscon, Arizona, 1979.

A. C. Hunt and M. Schönbächler. Timing of rapid core cooling events in the early solar system revealed by the pd-ag chronometer. *Goldschmidt Abstracts*, 1445, 2019.

A. C. Hunt, D. L. Cook, T. Lichtenberg, P. M. Reger, M. Ek, G. J. Golabek, and M. Schönbächler. Late metal–silicate separation on the IAB parent asteroid: constraints from combined W and Pt isotopes and thermal modelling. *Earth and Planetary Science Letters*, 482:490–500, 2018.

B. Ivanov and V. Kostuchenko. Block oscillation model for impact crater collapse. *Lunar and Planetary Science*, 28, #1655, 1997.

B. Ivanov, H. Melosh, and E. Pierazzo. Basin-forming impacts: Reconnaissance modeling. *Special Paper of the Geological Society of America*, 465:29–49, 2010.

B. C. Johnson, T. J. Bowling, A. J. Trowbridge, and A. M. Freed. Formation of the Sputnik Planum basin and the thickness of Pluto's subsurface ocean. *Geophysical Research Letters*, 43:10,068–10,077, 2016.

G. R. Johnson and W. H. Cook. A constitutive model and data for metals subjected to large strains, high strain rates and high temperatures. In *Proceedings of the 7th International Symposium on Ballistics*, volume 21, pages 541–547, 1983.

W. Jost. *Diffusion in solids, liquids, gases*. New York: Academic Press Inc., 1952.

M. Kameyama, D. A. Yuen, and S.-I. Karato. Thermal-mechanical effects of low-temperature plasticity (the Peierls mechanism) on the deformation of a viscoelastic shear zone. *Earth and Planetary Science Letters*, 168:159–172, 1999.

T. Kleine, M. Touboul, J. A. Van Orman, B. Bourdon, C. Maden, K. Mezger, and A. N. Halliday. Hf–W thermochronometry: Closure temperature and constraints on the accretion and cooling history of the H chondrite parent body. *Earth and Planetary Science Letters*, 270:106–118, 2008.

E. Kokubo and S. Ida. Oligarchic growth of protoplanets. *Icarus*, 131:171–178, 1998.

A. Krot, K. Keil, E. Scott, C. Goodrich, and M. Weisberg. Classification of meteorites and their genetic relationships. *Microphysics of Cosmic Plasmas*, 1:1–63, 2014.

M. Lambrechts and A. Johansen. Rapid growth of gas-giant cores by pebble accretion. *Astronomy & Astrophysics*, 544(A32), 2012.

Z. M. Leinhardt and S. T. Stewart. Full numerical simulations of catastrophic small body collisions. *Icarus*, 199:542–559, 2009.

Z. M. Leinhardt and S. T. Stewart. Collisions between gravity-dominated bodies. I. Outcome regimes and scaling laws. *The Astrophysical Journal*, 745:79, 2012.

Z. M. Leinhardt, D. C. Richardson, and T. Quinn. Direct N-body simulations of rubble pile collisions. *Icarus*, 146:133–151, 2000.

H. F. Levison, K. A. Kretke, and M. J. Duncan. Growing the gas-giant planets by the gradual accumulation of pebbles. *Nature*, 524:322–324, 2015.

J. J. Lissauer. Planet formation. *Annual review of astronomy and astrophysics*, 31:129–174, 1993.

R. Lyons, F. Ciesla, K. Walsh, T. Davison, and G. Collins. Thermal analysis of post-impact bodies in the early solar system. *Lunar and Planetary Science*, 47, #1603, 2016.

R. J. Lyons, T. J. Bowling, F. J. Ciesla, T. M. Davison, and G. S. Collins. The effects of impacts on the cooling rates of iron meteorites. *Meteoritics & Planetary Science*, 54: 1604–1618, 2019.

C. Maurel, J. F. Bryson, B. P. Weiss, R. Lyons, M. Ball, R. Chopdekar, and A. Scholl. Partial differentiation and magnetic history of the IIE iron meteorite parent body. *Lunar and Planetary Science*, 50, #2049, 2019.

C. Maurel, J. F. Bryson, R. J. Lyons, M. R. Ball, R. V. Chopdekar, A. Scholl, F. J. Ciesla, W. F. Bottke, and B. P. Weiss. Meteorite evidence for partial differentiation and protracted accretion of planetesimals. *Science Advances*, In Print, 2020.

H. Melosh, E. Ryan, and E. Asphaug. Dynamic fragmentation in impacts: Hydrocode simulation of laboratory impacts. *Journal of Geophysical Research: Planets*, 97:14735–14759, 1992.

A. Morbidelli and A. Crida. The dynamics of Jupiter and Saturn in the gaseous protoplanetary disk. *Icarus*, 191:158–171, 2007.

A. Morbidelli, H. Levison, K. Tsiganis, and R. Gomes. Chaotic capture of Jupiter's Trojan asteroids in the early Solar System. *Nature*, 435:462–465, 2005.

A. Morbidelli, W. F. Bottke, D. Nesvornỳ, and H. F. Levison. Asteroids were born big. *Icarus*, 204:558–573, 2009.

A. Moren and J. Goldstein. Cooling rate variations of group IVA iron meteorites. *Earth and Planetary Science Letters*, 40:151–161, 1978.

A. Moren and J. Goldstein. Cooling rates of group IVA iron meteorites determined from a ternary Fe-Ni-P model. *Earth and Planetary Science Letters*, 43:182–196, 1979.

D. P. O'Brien, A. Morbidelli, and H. F. Levison. Terrestrial planet formation with strong dynamical friction. *Icarus*, 184:39–58, 2006.

M. Ohnaka. A shear failure strength law of rock in the brittle-plastic transition regime. *Geophysical Research Letters*, 22:25–28, 1995.

O. Pravdivtseva, A. Meshik, C. Hohenberg, and G. Kurat. I-Xe ages of Campo del Cielo silicates as a record of the complex early history of the IAB parent body. *Meteoritics & Planetary Science*, 48:2480–2490, 2013.

K. L. Rasmussen. The cooling rates of iron meteorites—A new approach. *Icarus*, 45:564–576, 1981.

K. L. Rasmussen. Determination of the cooling rates and nucleation histories of eight group IVA iron meteorites using local bulk Ni and P variation. *Icarus*, 52:444–453, 1982.

K. L. Rasmussen. Cooling rates and parent bodies of iron meteorites from group IIICD, IAB, and IVB. *Physica Scripta*, 39:410, 1989.

K. L. Rasmussen, F. Ulff-Møller, and H. Haack. The thermal evolution of IVA iron meteorites: Evidence from metallographic cooling rates. *Geochimica et Cosmochimica Acta*, 59:3049–3059, 1995.

S. N. Raymond, D. P. O'Brien, A. Morbidelli, and N. A. Kaib. Building the terrestrial planets: Constrained accretion in the inner Solar System. *Icarus*, 203:644–662, 2009.

A. E. Rubin. Petrologic evidence for collisional heating of chondritic asteroids. *Icarus*, 113: 156–167, 1995.

A. E. Rubin. Chromite-plagioclase assemblages as a new shock indicator; implications for the shock and thermal histories of ordinary chondrites. *Geochimica et Cosmochimica Acta*, 67:2695–2709, 2003.

A. E. Rubin. Postshock annealing and postannealing shock in equilibrated ordinary chondrites: Implications for the thermal and shock histories of chondritic asteroids. *Geochimica et Cosmochimica Acta*, 68:673–689, 2004.

A. Ruzicka. Silicate-bearing iron meteorites and their implications for the evolution of asteroidal parent bodies. *Chemie der Erde-Geochemistry*, 74:3–48, 2014.

A. Ruzicka and M. Hutson. Comparative petrology of silicates in the Udei Station (IAB) and Miles (IIE) iron meteorites: Implications for the origin of silicate-bearing irons. *Geochimica et Cosmochimica Acta*, 74:394–433, 2010.

T. Schulz, C. Münker, H. Palme, and K. Mezger. Hf–W chronometry of the IAB iron meteorite parent body. *Earth and Planetary Science Letters*, 280:185–193, 2009.

T. Schulz, C. Münker, K. Mezger, and H. Palme. Hf–W chronometry of primitive achondrites. *Geochimica et Cosmochimica Acta*, 74:1706–1718, 2010.

T. Schulz, D. Upadhyay, C. Münker, and K. Mezger. Formation and exposure history of non-magmatic iron meteorites and winonaites: Clues from Sm and W isotopes. *Geochimica et Cosmochimica Acta*, 85:200–212, 2012.

E. R. Scott, H. Haack, and S. G. Love. Formation of mesosiderites by fragmentation and reaccretion of a large differentiated asteroid. *Meteoritics & Planetary Science*, 36:869–881, 2001.

E. R. Scott, T. V. Krot, J. I. Goldstein, and S. Wakita. Thermal and impact history of the H chondrite parent asteroid during metamorphism: Constraints from metallic Fe–Ni. *Geochimica et Cosmochimica Acta*, 136:13–37, 2014.

E. M. Shoemaker. Interpretation of luner caters. *Physics and astronomy of the Moon*, pages 283–359, 1962.

G. J. Taylor, P. Maggiore, E. R. Scott, A. E. Rubin, and K. Keil. Original structures, and fragmentation and reassembly histories of asteroids: Evidence from meteorites. *Icarus*, 69: 1–13, 1987.

K. Theis, M. Schönbächler, G. Benedix, M. Rehkämper, R. Andreasen, and C. Davies. Palladium–silver chronology of IAB iron meteorites. *Earth and Planetary Science Letters*, 361:402–411, 2013.

S. L. Thompson. Aneos analytic equations of state for shock physics codes input manual. *Albuquerque, New Mexico: Sandia National Laboratories*, 1990.

K. Tsiganis, R. Gomes, A. Morbidelli, and H. Levison. Origin of the orbital architecture of the giant planets of the Solar System. *Nature*, 435:459–461, 2005.

N. Vogel and P. R. Renne. ^{40}Ar–^{39}Ar dating of plagioclase grain size separates from silicate inclusions in IAB iron meteorites and implications for the thermochronological evolution of the IAB parent body. *Geochimica et Cosmochimica Acta*, 72:1231–1255, 2008.

K. J. Walsh, A. Morbidelli, S. N. Raymond, D. P. O'Brien, and A. M. Mandell. A low mass for Mars from Jupiter's early gas-driven migration. *Nature*, 475:206–209, 2011.

P. H. Warren. Ejecta–megaregolith accumulation on planetesimals and large asteroids. *Meteoritics & Planetary Science*, 46:53–78, 2011.

P. H. Warren and K. L. Rasmussen. Megaregolith insulation, internal temperatures, and bulk uranium content of the Moon. *Journal of Geophysical Research: Solid Earth*, 92: 3453–3465, 1987.

J. Wasson and G. Kallemeyn. The IAB iron-meteorite complex: A group, five subgroups, numerous grouplets, closely related, mainly formed by crystal segregation in rapidly cooling melts. *Geochimica et Cosmochimica Acta*, 66:2445–2473, 2002.

J. T. Wasson. *Meteorites: Classification and properties*, volume 10. Springer Science & Business Media, 2012.

J. T. Wasson. Formation of the Treysa quintet and the main-group pallasites by impact-generated processes in the IIIAB asteroid. *Meteoritics & Planetary Science*, 51:773–784, 2016.

J. T. Wasson and W. Jianmin. A nonmagmatic origin of group-IIE iron meteorites. *Geochimica et Cosmochimica Acta*, 50:725–732, 1986.

C. Williams, K. Keil, G. Taylor, and E. Scott. Cooling rates of equilibrated clasts in ordinary chondrite regolith breccias: Implications for parent body histories. *Chemie der Erde-Geochemistry*, 59:287–305, 2000.

J. Willis and J. T. Wasson. Cooling rates of group IVA iron meteorites. *Earth and Planetary Science Letters*, 40:141–150, 1978.

J. A. Wood. The cooling rates and parent planets of several iron meteorites. *Icarus*, 3: 429–459, 1964.

J. A. Wood. Chondrites: Their metallic minerals, thermal histories, and parent planets. *Icarus*, 6:1–49, 1967.

E. A. Worsham, K. R. Bermingham, and R. J. Walker. Siderophile element systematics of iab complex iron meteorites: new insights into the formation of an enigmatic group. *Geochimica et cosmochimica acta*, 188:261–283, 2016.

K. Wünnemann, G. Collins, and H. Melosh. A strain-based porosity model for use in hydrocode simulations of impacts and implications for transient crater growth in porous targets. *Icarus*, 180:514–527, 2006.

J. Yang and J. I. Goldstein. Metallographic cooling rates of the IIIAB iron meteorites. *Geochimica et Cosmochimica Acta*, 70:3197–3215, 2006.

J. Yang, J. I. Goldstein, and E. R. Scott. Iron meteorite evidence for early formation and catastrophic disruption of protoplanets. *Nature*, 446:888–891, 2007.

J. Yang, J. I. Goldstein, and E. R. Scott. Metallographic cooling rates and origin of IVA iron meteorites. *Geochimica et Cosmochimica Acta*, 72:3043–3061, 2008.

J. Yang, J. I. Goldstein, J. R. Michael, P. G. Kotula, and E. R. Scott. Thermal history and origin of the IVB iron meteorites and their parent body. *Geochimica et Cosmochimica Acta*, 74:4493–4506, 2010a.

J. Yang, J. I. Goldstein, and E. R. Scott. Main-group pallasites: Thermal history, relationship to IIIAB irons, and origin. *Geochimica et Cosmochimica Acta*, 74:4471–4492, 2010b.

J. Yang, J. Goldstein, E. Scott, J. Michael, P. Kotula, T. Pham, and T. McCoy. Thermal and impact histories of reheated group IVA, IVB, and ungrouped iron meteorites and their parent asteroids. *Meteoritics & Planetary Science*, 46:1227–1252, 2011.

K. Yomogida and T. Matsui. Multiple parent bodies of ordinary chondrites. *Earth and Planetary Science Letters*, 68:34–42, 1984.